

AD A337 050

ANALYSIS OF A HIGH-STRENGTH CONCRETE MODEL UNDER
BIAXIAL COMPRESSION(U) TEXAS UNIV AT AUSTIN DEPT OF
CIVIL ENGINEERING P M CASTRO ET AL. MAY 83

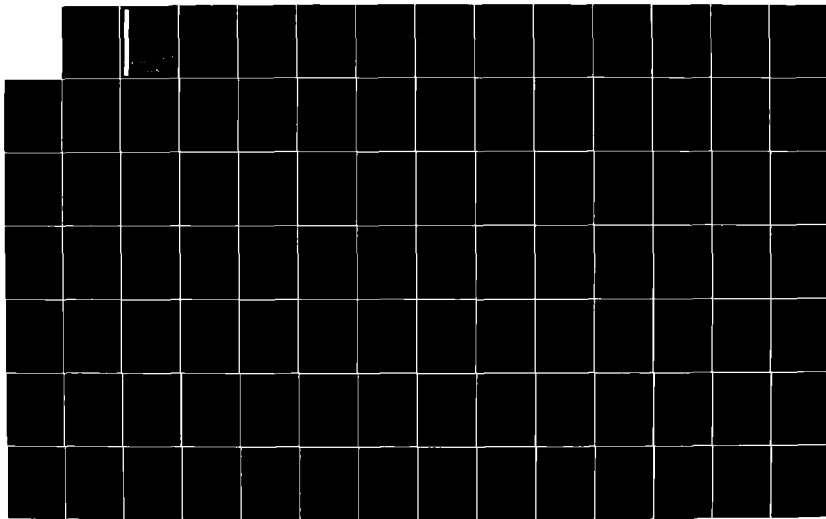
1/3

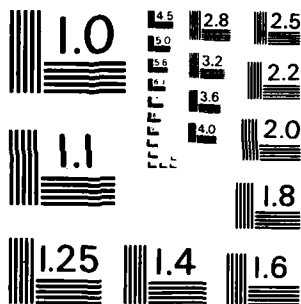
UNCLASSIFIED

AFOSR-TR 83 1341 AFOSR-81-0202

F/G 13/3

NI





MICROCOPY RESOLUTION TEST CHART
NATIONAL BUREAU OF STANDARDS - 1963 - A

AFOSR-TR- 83-1341

**ANALYSIS OF A HIGH-STRENGTH CONCRETE
MODEL UNDER BIAXIAL COMPRESSION**

BY

PAULO M. CASTRO

JOHN L. TASSOULAS

RAMON L. CARRASQUILLO

DAVID W. FOWLER

Annual

RESEARCH REPORT AF-2

FOR

UNITED STATES AIR FORCE
OFFICE OF SCIENTIFIC RESEARCH
BOLLING AIR FORCE BASE

CONTRACT NO. AFOSR-81-0202

DEPARTMENT OF CIVIL ENGINEERING
THE UNIVERSITY OF TEXAS AT AUSTIN

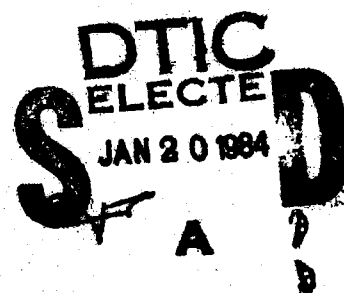
MAY 1983

83 01 18 106

APPROVED FOR PUBLIC RELEASE; DISTRIBUTION UNLIMITED

AD A 137050

DTIC FILE COPY



unclassified

SECURITY

CLASSIFICATION OF THIS PAGE (When Data Entered)

REPORT DOCUMENTATION PAGE		READ INSTRUCTIONS BEFORE COMPLETING FORM
1. REPORT NUMBER AFOSR-TR- 83- 1341	2. GOVT ACCESSION NO. ADA137050	3. RECIPIENT'S CATALOG NUMBER
4. TITLE (and Subtitle) Analysis of a High-Strength Concrete Model Under Biaxial Compression		5. TYPE OF REPORT & PERIOD COVERED ANNUAL 31 Dec 1982 - 1 June 1983
		6. PERFORMING ORG. REPORT NUMBER
7. AUTHOR(s) P. Castro, J.L. Tassoulas, R.L. Carrasquillo, and D.W. Fowler		8. CONTRACT OR GRANT NUMBER(s) AFOSR-81-0202
9. PERFORMING ORGANIZATION NAME AND ADDRESS The University of Texas at Austin Department of Civil Engineering; ECJ 5.2 Austin TX 78712		10. PROGRAM ELEMENT, PROJECT, TASK AREA & WORK UNIT NUMBERS 61102F 2307/C2
11. CONTROLLING OFFICE NAME AND ADDRESS Air Force Office of Scientific Research/NA Bolling AFB DC 20332		12. REPORT DATE MAY 1983
		13. NUMBER OF PAGES 144
14. MONITORING AGENCY NAME & ADDRESS (if different from Controlling Office)		15. SECURITY CLASS. (of this report) UNCLASSIFIED
		15a. DECLASSIFICATION/DOWNGRADING SCHEDULE
16. DISTRIBUTION STATEMENT (of this Report) APPROVED FOR PUBLIC RELEASE: DISTRIBUTION UNLIMITED.		
17. DISTRIBUTION STATEMENT (of the abstract entered in Block 20, if different from Report)		
18. SUPPLEMENTARY NOTES		
19. KEY WORDS (Continue on reverse side if necessary and identify by block number) high-strength, concrete, biaxial loading, finite element analysis; properties		
20. ABSTRACT (Continue on reverse side if necessary and identify by block number) The behavior of a model of high-strength concrete consisting of nine coarse aggregate circular inclusions in a square mortar matrix is studied under biaxial compressive loads. Constitutive equations are developed following the theory of plasticity in order to describe the behavior of mortar in biaxial compression. The bond between mortar and aggregates is simulated by an inter- face element. A comparison of analytical and experimental results shows good agreement.		

DD FORM 1 JAN 73 1473

EDITION OF 1 NOV 65 IS OBSOLETE

SECURITY CLASSIFICATION OF THIS PAGE (When Data Entered)

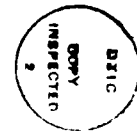
**Qualified requestors may obtain additional copies from
the Defense Technical Information Service.**

Conditions of Reproduction

**Reproduction, translation, publication, use and disposal
in whole or in part by or for the United States
Government is permitted.**

ABSTRACT

↙
The behavior of a model of high-strength concrete consisting of nine coarse aggregate circular inclusions in a square mortar matrix is studied under biaxial compressive loads. Constitutive equations are developed following the theory of plasticity in order to describe the behavior of mortar in biaxial compression. The bond between mortar and aggregates is simulated by an interface element. A comparison of analytical and experimental results shows good agreement.
↑



A1

A

AIR FORCE OFFICE OF SCIENTIFIC RESEARCH
NOTICE OF RESEARCH RESULTS
THIS REPORT IS THE PROPERTY OF THE AIR FORCE
OFFICE OF SCIENTIFIC RESEARCH
AND IS LOANED TO YOUR ORGANIZATION
IT IS TO BE RETURNED TO THE AIR FORCE
OFFICE OF SCIENTIFIC RESEARCH
Chief, Technical Information Division

ACKNOWLEDGEMENTS

The authors wish to acknowledge the support of the United States Air Force Office of Scientific Research for sponsoring this work. The advice and encouragement of Lt. Col. J.J. Allen and Lt. Col Dale Hokanson are appreciated.

The assistance of John Herrin and Robert Chen is gratefully acknowledged. Nancy Zett was very helpful in compiling the final report.

Paulo Castro
John Tassoulas
Ramon Carrasquillo
David W. Fowler

TABLE OF CONTENTS

LIST OF TABLES	vii
----------------------	-----

LIST OF FIGURES	viii
-----------------------	------

Chapter		Page
1	INTRODUCTION	1
2	HIGH STRENGTH CONCRETE	3
	2.1 Introduction	3
	2.2 Applications of High-Strength Concrete	3
	2.3 Properties of High-Strength Concrete	5
	2.3.1 Uniaxial Compressive Strength	5
	2.3.2 Stress-Strain Relations	5
	2.3.3 Microcracking	5
	2.3.4 Failure Mode	6
	2.4 Component Materials Used in the Concrete Model	7
3	DESCRIPTION OF A CONSTITUTIVE MODEL	9
	3.1 Introduction	9
	3.2 Description of the Model	9
	3.3 Constitutive Equations	16
	3.4 Parameter Estimation	19
4	THE FINITE ELEMENT ANALYSIS OF THE CONCRETE MODEL	27
	4.1 Introduction	27
	4.2 Linear Analysis	27
	4.2.1 Derivation of the Element Stiffness Matrix ..	30
	4.2.2 Modification of the Element Stiffness Matrix for Support Conditions,	38
	4.2.3 Assembly and Solution of the Structure System of Equations	41
	4.2.4 Calculation of Stresses and Strains in the Body	42
	4.2.5 Accuracy Test of the Linear Finite Element Analysis	42
	4.3 Nonlinear Analysis	45
	4.3.1 Implementation of the Constitutive Model in the Nonlinear Analysis	48
	4.3.2 Calculation of Residual Forces from Residual Stresses	54

TABLE OF CONTENTS (continued)

Chapter		Page
4	THE FINITE ELEMENT ANALYSIS OF THE CONCRETE MODEL (continued)	
	4.3.3 Convergence Criterion	55
	4.3.4 Failure Criteria	55
5	MORTAR-AGGREGATE INTERFACE MODELING	57
	5.1 Introduction	57
	5.2 Derivation of the Stiffness Matrix of the Interface Element	58
	5.3 Bond Strength between the Mortar and the Coarse Aggregate	65
	5.4 Implementation of the Bond Properties in the Analysis	67
6	ANALYTICAL RESULTS AND COMPARISON	69
	6.1 Introduction	69
	6.2 Estimation of the Bond Properties of the Interface	69
	6.3 Analysis Prediction of the Concrete Model Behavior .	70
	6.3.1 Elastic Distribution of Stresses	73
	6.3.2 Evolution of Damage in the Concrete Model during Loading	82
	6.3.3 Comparison between Analytical and Experimental Results	95
	6.4 Analysis of Constrained Specimens	104
	6.5 Analysis Shortcomings	112
7	SUMMARY AND CONCLUSIONS	130
	7.1 Summary	130
	7.2 Conclusions	131
	REFERENCES	132

LIST OF TABLES

Table	Page
2.1 Elastic Properties of the Mortar and the Coarse Aggregate	7
3.1 Relationship between k and H in Uniaxial Compression	22
3.2 Expressions for H as a Function of k in Uniaxial Compression	22
3.3 Expressions for H under Multiaxial States of Stress	24
3.4 Relationship between k and β in Uniaxial Compression	25
4.1 Comparison between Results of the Finite Element Analysis and the Exact Solution	45

LIST OF FIGURES

Figure	Page
2.1 The concrete model	4
2.2 Stress-strain curves for concrete	6
2.3 Typical stress-strain curves for the coarse aggregate and the mortar	8
3.1 Typical yield surface in $\sigma - \tau$ space	16
3.2 Yield surfaces in $\sigma_1 - \sigma_2$ space	21
3.3 Yield surfaces in $\sigma - \tau$ space	21
3.4 Stress-strain curves for mortar in uniaxial compression. Comparison between test results and the model	26
4.1 Discretization of the concrete model by finite elements .	28
4.2 Local system of coordinates for the eight node element ..	32
4.3 Integration points for the eight-node element in local coordinates	37
4.4 A test in the elastic analysis	43
4.5 Finite element meshes used in the test analyses	44
4.6 P vs. u diagram for a one-degree-of-freedom structure ...	46
5.1 Interface element in global and local systems of coordinates	58
5.2 Bond failure envelope in the $\sigma - \tau$ space	66
6.1 Comparison between analytical and experimental results using different bond properties for the interface ($\sigma_2/\sigma_1 = 0.0$)	71
6.2 Map of bond damage for the case of normal-strength concrete bond properties ($\sigma_2/\sigma_1 = 0.0$, $\sigma_1 = 0.40 \sigma_u$)	72

LIST OF FIGURES (continued)

Figure		Page
6.3	Graphical representation of the smaller principal stress at the integration points ($\sigma_2/\sigma_1 = 0.0$)	74
6.4	Graphical representation of the larger principal stress at the integration points ($\sigma_2/\sigma_1 = 0.0$)	75
6.5	Graphical representation of the smaller principal stress at the integration points ($\sigma_2/\sigma_1 = 0.20$)	76
6.6	Graphical representation of the larger principal stress at the integration points ($\sigma_2/\sigma_1 = 0.20$)	77
6.7	Graphical representation of the smaller principal stress at the integration points ($\sigma_2/\sigma_1 = 0.50$)	78
6.8	Graphical representation of the larger principal stress at the integration points ($\sigma_2/\sigma_1 = 0.50$)	79
6.9	Graphical representation of the smaller principal stress at the integration points ($\sigma_2/\sigma_1 = 1.0$)	80
6.10	Graphical representation of the larger principal stress at the integration points ($\sigma_2/\sigma_1 = 1.0$)	81
6.11	Degree of damage in the specimen at 65 percent of the analytical ultimate strength ($\sigma_2/\sigma_1 = 0.0$)	83
6.12	Degree of damage in the specimen at 80 percent of the analytical ultimate strength ($\sigma_2/\sigma_1 = 0.0$)	84
6.13	Degree of damage in the specimen at the analytical ultimate strength ($\sigma_2/\sigma_1 = 0.0$)	85
6.14	Degree of damage in the specimen at 57 percent of the analytical ultimate strength ($\sigma_2/\sigma_1 = 0.20$)	86
6.15	Degree of damage in the specimen at 78 percent of the analytical ultimate strength ($\sigma_2/\sigma_1 = 0.20$)	87
6.16	Degree of damage in the specimen at the analytical ultimate strength ($\sigma_2/\sigma_1 = 0.20$)	88

LIST OF FIGURES (continued)

Figure		Page
6.17	Degree of damage in the specimen at 48 percent of the analytical ultimate strength ($\sigma_2/\sigma_1 = 0.50$)	89
6.18	Degree of damage in the specimen at 74 percent of the analytical ultimate strength ($\sigma_2/\sigma_1 = 0.50$)	90
6.19	Degree of damage in the specimen at the analytical ultimate strength ($\sigma_2/\sigma_1 = 0.50$)	91
6.20	Degree of damage in the specimen at 52 percent of the analytical ultimate strength ($\sigma_2/\sigma_1 = 1.0$)	92
6.21	Degree of damage in the specimen at 84 percent of the analytical ultimate strength ($\sigma_2/\sigma_1 = 1.0$)	93
6.22	Degree of damage in the specimen at the analytical ultimate strength ($\sigma_2/\sigma_1 = 1.0$)	94
6.23	Comparison between analytical and experimental results ($\sigma_2/\sigma_1 = 0.0$, $H = f(\sigma, k)$)	96
6.24	Comparison between analytical and experimental results ($\sigma_2/\sigma_1 = 0.20$, $H = f(\sigma, k)$)	97
6.25	Comparison between analytical and experimental results ($\sigma_2/\sigma_1 = 0.50$, $H = f(\sigma, k)$)	98
6.26	Comparison between analytical and experimental results ($\sigma_2/\sigma_1 = 1.0$, $H = f(\sigma, k)$)	99
6.27	Comparison between analytical and experimental results ($\sigma_2/\sigma_1 = 0.0$, $H = f(k)$)	100
6.28	Comparison between analytical and experimental results ($\sigma_2/\sigma_1 = 0.20$, $H = f(k)$)	101
6.29	Comparison between analytical and experimental results ($\sigma_2/\sigma_1 = 0.50$, $H = f(k)$)	102
6.30	Comparison between analytical and experimental results ($\sigma_2/\sigma_1 = 1.0$, $H = f(k)$)	103

LIST OF FIGURES (continued)

Figure		Page
6.31	Finite element mesh with the steel elements attached	106
6.32	Comparison between analytical results with and without edge restraints and the experimental results ($\sigma_2/\sigma_1 = 0.0$)	107
6.33	Comparison between analytical results with and without edge restraints and the experimental results ($\sigma_2/\sigma_1 = 0.20$)	108
6.34	Comparison between analytical results with and without edge restraints and the experimental results ($\sigma_2/\sigma_1 = 0.50$)	109
6.35	Comparison between analytical results with and without edge restraints and the experimental results ($\sigma_2/\sigma_1 = 1.0$)	110
6.36	Three-node bar element used in the constrained analysis of the specimen	111
6.37	Comparison between analytical results with edge stiffening elements attached and the experimental results ($\sigma_2/\sigma_1 = 0.0$)	113
6.38	Comparison between analytical results with edge stiffening elements attached and the experimental results ($\sigma_2/\sigma_1 = 0.20$)	114
6.39	Comparison between analytical results with edge stiffening elements attached and the experimental results ($\sigma_2/\sigma_1 = 0.50$)	115
6.40	Comparison between analytical results with edge stiffening elements attached and the experimental results ($\sigma_2/\sigma_1 = 1.0$)	116
6.41	Degree of damage in the specimen at 65 percent of the analytical ultimate strength with the edge stiffening elements attached ($\sigma_2/\sigma_1 = 0.0$)	117

LIST OF FIGURES (continued)

Figure		Page
6.42	Degree of damage in the specimen at 80 percent of the analytical ultimate strength with the edge stiffening elements attached ($\sigma_2/\sigma_1 = 0.00$)	118
6.43	Degree of damage in the specimen at the analytical ultimate strength with the edge stiffening elements attached ($\sigma_2/\sigma_1 = 0.0$)	119
6.44	Degree of damage in the specimen at 58 percent of the analytical ultimate strength with the edge stiffening elements attached ($\sigma_2/\sigma_1 = 0.20$)	120
6.45	Degree of damage in the specimen at 79 percent of the analytical ultimate strength with the edge stiffening elements attached ($\sigma_2/\sigma_1 = 0.20$)	121
6.46	Degree of damage in the specimen at the analytical ultimate strength with the edge stiffening elements attached ($\sigma_2/\sigma_1 = 0.20$)	122
6.47	Degree of damage in the specimen at 53 percent of the analytical ultimate strength with the edge stiffening elements attached ($\sigma_2/\sigma_1 = 0.50$)	123
6.48	Degree of damage in the specimen at 79 percent of the analytical ultimate strength with the edge stiffening elements attached ($\sigma_2/\sigma_1 = 0.50$)	124
6.49	Degree of damage in the specimen at the analytical ultimate strength with the edge stiffening elements attached ($\sigma_2/\sigma_1 = 0.50$)	125
6.50	Degree of damage in the specimen at 58 percent of the analytical ultimate strength with the edge stiffening elements attached ($\sigma_2/\sigma_1 = 1.0$)	126
6.51	Degree of damage in the specimen at 74 percent of the analytical ultimate strength with the edge stiffening elements attached ($\sigma_2/\sigma_1 = 1.0$)	127
6.52	Degree of damage in the specimen at the analytical ultimate strength with the edge stiffening elements attached ($\sigma_2/\sigma_1 = 1.0$)	128

CHAPTER 1

INTRODUCTION

This present work is part of a study of the behavior of high-strength concrete under monotonic biaxial compressive loading. A model of concrete, consisting of a square mortar plate with nine coarse aggregate circular inclusions (see Fig. 2.1), is analyzed using the Finite Element Method. The analytical results are then compared with results of experimental tests of the same model.

The analysis takes into account the nonlinear behavior of the mortar using the constitutive equations proposed in Ref. 1. These constitutive equations have proved adequate for the prediction of the behavior of concrete under biaxial states of stress.

The significance of the bond between the coarse aggregate and the mortar is also studied using an interface element developed in this work. Relative displacement of the two materials occurs if the strength of the bond is exceeded.

Chapter 2 gives a brief account of the behavior of high-strength concrete and presents a comparison with normal-strength concrete. The properties of the materials used in the analysis are also presented. The constitutive equations used for the mortar are described in detail in Chapter 3 and the linear and nonlinear finite element analysis of the concrete model are developed in Chapter 4. Chapter 5 shows the modeling of the interface between the mortar and

the coarse aggregate and the bond properties between the two materials. Chapter 6 gives the analytical results and compares them with experimental ones. Finally, some conclusions about the important factors affecting the stiffness and strength of the concrete model are listed in Chapter 7.

CHAPTER 2

HIGH-STRENGTH CONCRETE

2.1 Introduction

The concrete model shown in Fig. 2.1 was first proposed in Ref. 2 for the study of the behavior of normal-strength concrete subjected to biaxial loading. In the present work, the same model is used to study the behavior of high-strength concrete under biaxial loads. Thus, this chapter gives a brief presentation of applications and properties of high-strength concrete and summarizes the most important differences in behavior between high-strength concrete and normal-strength concrete. The properties of the component materials in the concrete model are also presented.

2.2 Applications of High-Strength Concrete

In recent years, efforts have been made to improve the compressive strength of concrete. Nowadays, high-strength concrete is becoming increasingly common. Among other applications, it has been used in high-rise buildings where oversized columns can be avoided in the lower floors, or in prestressed flexural members permitting larger values of span-to-depth ratio. It also has great potential of use in structures in which the concrete is subjected to a biaxial state of stress such as large shells, containment vessels and tunnels.

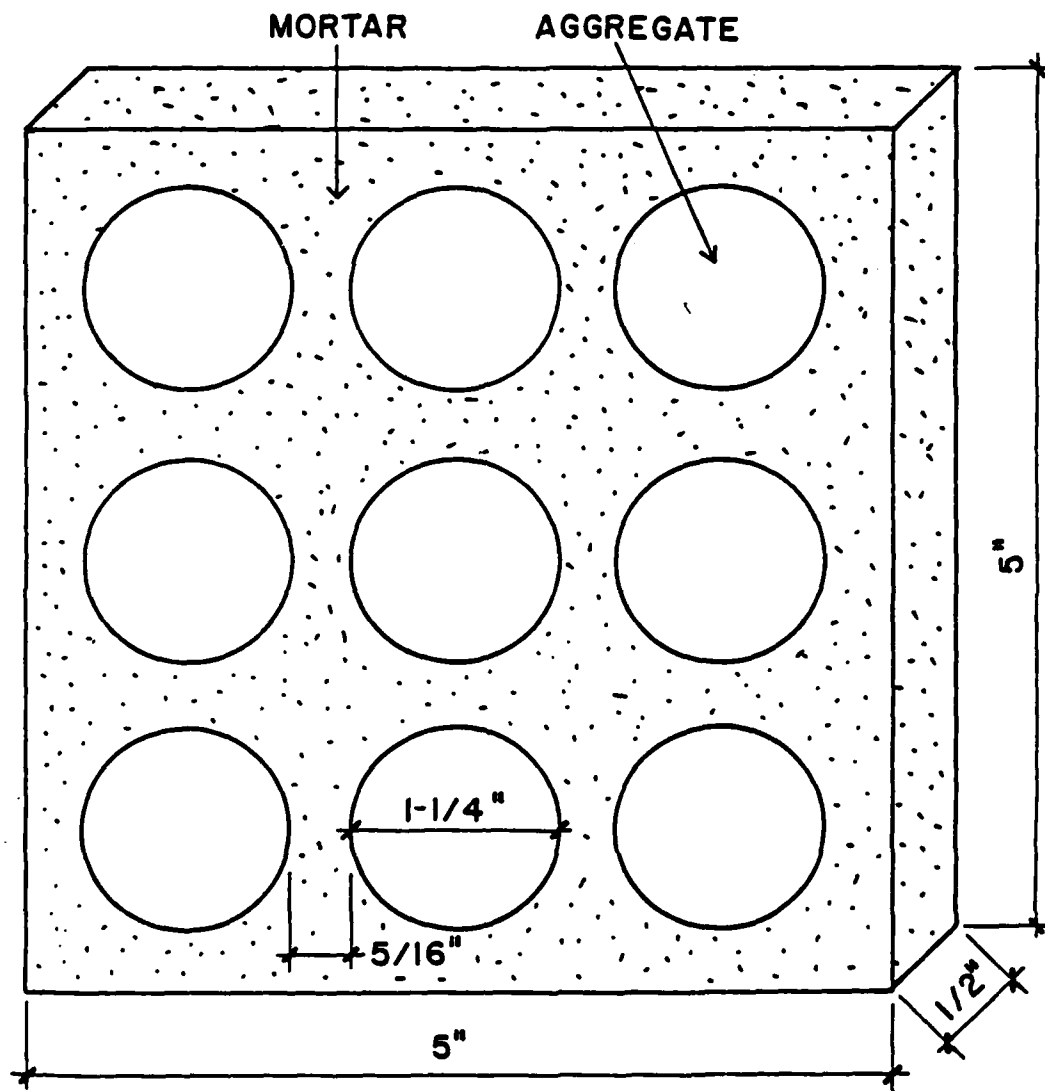


Fig. 2.1 The concrete model

2.3 Properties of High-Strength Concrete

2.3.1 Uniaxial Compressive Strength. Although there is no well defined boundary between normal-strength and high-strength concrete, some authors (see Ref. 3) classify arbitrarily concrete with a specified cylinder compressive strength of at least 6,000 psi as being high-strength concrete. Concretes with specified cylinder compressive strength in the range of 8,000 to 10,000 psi have been used successfully with conventional technology and materials but with careful selection, proportioning and quality control. In this study, the uniaxial compressive strength of the concrete model ranged between 6,000 and 8,000 psi.

2.3.2 Stress-Strain Relations. Plain concrete has some amount of ductility. This ductility, however, decreases with increasing concrete strength. The stress-strain relation up to ultimate strength becomes almost a straight line as the concrete strength increases (see Fig. 2.2 and Ref. 3). Note that there is a descending branch in each curve after the maximum stress has been reached. Also, the maximum strain at failure in compression is lower at higher concrete strengths. The maximum ultimate strain may be below 0.003 for higher-strength concretes. As it may be seen in Fig. 2.2, the modulus of elasticity is greater for higher strength concrete.

2.3.3 Microcracking. The differences in behavior between high-strength and normal-strength concrete as shown in Fig. 2.2 may be explained by differences in microcracking. For higher-strength concretes there is less cracking at the interface between the aggregate

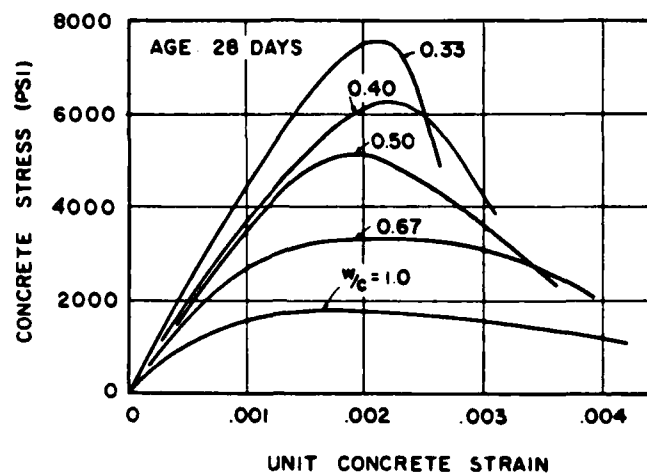


Fig. 2.2 Stress-strain curves for concrete (Ref. 3)

and the mortar than for lower-strength concretes and the stress-strength ratio at which microcracks begin to form continuous crack patterns is higher. Therefore, the stress-strain curve is steeper and closely linear up to a higher stress-strength ratio (see Ref. 4), and the number of continuous crack paths is smaller for higher-strength concrete resulting in a decrease in the redundancy present in the material. This is an explanation for its lack of ductility.

2.3.4 Failure Mode. High-strength concrete behaves more like a homogenous material than normal-strength concrete and therefore their failure modes in uniaxial compression are different. The fracture surface of normal-strength concrete generally follows the contour of the coarse aggregate surface in inclined planes forming a cone of rupture. In high-strength concrete, failure occurs in a plane parallel to the applied load and passing through the aggregate and the mortar (see Ref. 4).

2.4 Component Materials Used in the Concrete Model

Typical stress-strain curves for the mortar and the coarse aggregate used in the concrete model are shown in Fig. 2.3. As it may be seen, the coarse aggregate behaves almost linearly up to ultimate strength and the mortar shows some nonlinearities for loads higher than approximately 40 percent of ultimate strength. Thus, in this study, the coarse aggregate will be assumed to be elastic and the nonlinear behavior of mortar will be taken into account.

The coarse aggregate and the mortar used in this study were obtained, respectively, from limestone rock and from a mix of natural sand and type I cement ($w/c = 0.35$, $s/c = 2.0$). The elastic properties of the two materials obtained from the average of three tests on cylinder specimens are presented in Table 2.1.

TABLE 2.1 Elastic Properties of the Mortar and the Coarse Aggregate

Material Property	Coarse Aggregate	Mortar
Compressive Strength (psi)	12,850	10,970
Tensile Strength (psi)	---	1,029
Modulus of Elasticity (psi)	4.49×10^6	6.74×10^6
Poisson's Ratio	0.058	0.25

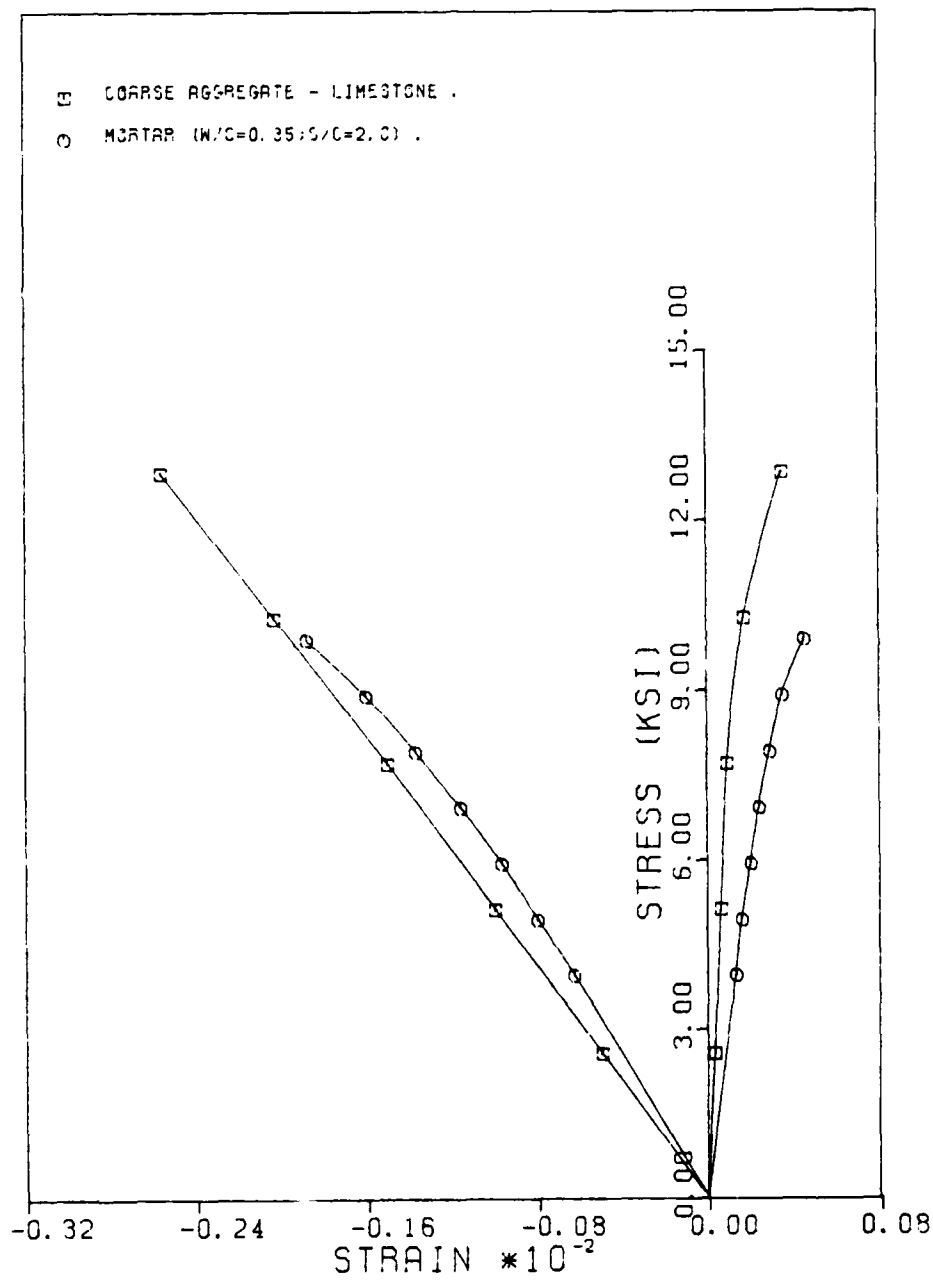


Fig. 2.3 Typical stress-strain curves for the coarse aggregate and the mortar.

CHAPTER 3

DESCRIPTION OF A CONSTITUTIVE MODEL

3.1 Introduction

The behavior of the coarse aggregate and the mortar under short-term monothonic compression was discussed in detail in Chapter 2. In uniaxial compression the stress-strain curve for the mortar may be assumed linear for levels of load up to 40-50 percent of ultimate strength. Beyond this point, inelastic behavior is clearly obtained and must be considered in the analysis.

In this chapter a model is presented applicable to the description of the behavior of the mortar under multiaxial states of stress. The model parameters are estimated from experimental results. As outlined below, the development of the model follows the formalism of the classical theory of plasticity. The model was first proposed in Ref. 1 in which details may be found.

3.2 Description of the Model

Following the theory of plasticity, the increment of strain $d\epsilon_{ij}$ is taken to be the sum of an increment of strain resulting from elastic behavior $d\epsilon_{ij}^e$ and an increment of strain resulting from inelastic (plastic) behavior $d\epsilon_{ij}^p$.

$$d\epsilon_{ij} = d\epsilon_{ij}^e + d\epsilon_{ij}^p \quad (3.1)$$

Assuming that the elasticity of the material is isotropic, the elastic increment of strain $d \epsilon_{ij}^e$ is given by:

$$d \epsilon_{ij}^e = C_{ijkl}^e d \sigma_{kl} \quad (3.2)$$

where C_{ijkl}^e is the isotropic elastic compliance tensor and is given by:

$$C_{ijkl}^e = \left[\frac{1}{2G} \delta_{ik} \delta_{jl} + \left(\frac{1}{9K} - \frac{1}{6G} \right) \delta_{ij} \delta_{kl} \right] \quad (3.3)$$

(Indicial notation is conveniently used. Indices assume the values 1, 2, 3. The Kronecker delta δ_{ij} is defined as $\delta_{ij} = 0$, if $i \neq j$ and $\delta_{ij} = 1$, if $i = j$). K and G are the elastic bulk and shear moduli defined as:

$$K = \frac{E}{3(1-2\nu)} \quad (3.4)$$

$$G = \frac{E}{2(1+\nu)} \quad (3.5)$$

E and ν are the Young's modulus and the Poisson's ratio respectively.

An alternative form of Eq. (3.2) is:

$$d \epsilon_{ij}^e = \frac{d S_{ij}}{2G} \quad (3.6a)$$

$$d \epsilon^e = \frac{d \sigma}{K} \quad (3.6b)$$

$$d \epsilon_{ij}^e = d \epsilon_{ij}^e + \frac{1}{3} d \epsilon \delta_{ij} \quad (3.7)$$

$$d \sigma_{ij} = d S_{ij} + d \sigma \delta_{ij} \quad (3.8)$$

$d \epsilon_{ij}^e$ is the elastic increment of deviatoric strain. $d \epsilon^e = d \epsilon_{ii}^e$ is the elastic increment of volumetric strain. $d \sigma = \frac{1}{3} d \sigma_{ii}$ is the increment of hydrostatic stress and $d S_{ij}$ is the increment of deviatoric stress.

An important assumption in the calculation of the plastic increment of strain $d \epsilon_{ij}^p$, following the theory of plasticity, is the existence of a yield function. In the present model, the arguments of the yield function, F , are the state of stress, σ_{ij} , and a parameter, k , that reflects the history of plastic deformation:

$$F(\sigma_{ij}, k) = 0. \quad (3.9)$$

In the space of stresses σ_{ij} , the yield function may be represented by a surface. For plastic deformation to occur the material must be subjected to a state of stress that lies on this surface, $F = 0$ (yield surface). If the state of stress is in the interior of the convex region bounded by the surface, $F < 0$, only elastic deformation occurs. The value of the parameter k changes so that the state of stress satisfies $F = 0$ during plastic deformation. Thus, the region

defined by $F > 0$ is the set of states of stress which cannot be obtained without further plastic deformation. In this way, an increment of stress $d\sigma_{ij}$ can be considered as loading, if it is directed towards the exterior of the convex region bounded by the yield surface, as unloading if it is directed towards the interior of the convex region and as neutral loading, if it is tangent to the yield surface:

1) Loading:

$$F(\sigma_{ij}, k) = 0 \text{ and } \frac{\partial F}{\partial \sigma_{ij}} d\sigma_{ij} > 0 \quad (3.10a)$$

2) Unloading:

$$F(\sigma_{ij}, k) = 0 \text{ and } \frac{\partial F}{\partial \sigma_{ij}} d\sigma_{ij} < 0 \quad (3.10b)$$

3) Neutral Loading:

$$F(\sigma_{ij}, k) = 0 \text{ and } \frac{\partial F}{\partial \sigma_{ij}} d\sigma_{ij} = 0 \quad (3.10c)$$

(It is assumed that F is continuously differentiable.) Plastic deformation occurs only during loading. The yield function F is assumed isotropic, involving invariants of the stress tensor σ_{ij} , namely, the hydrostatic stress (mean normal stress)

$$\sigma = \frac{1}{3} \sigma_{ii}$$

and the shearing stress intensity

$$\tau = \left[\frac{1}{2} S_{ij} S_{ij} \right]^{1/2} =$$

$$\sqrt{1/6} [(\sigma_1 - \sigma_2)^2 + (\sigma_2 - \sigma_3)^2 + (\sigma_3 - \sigma_1)^2]^{1/2}$$

($S_{ij} = \sigma_{ij} - \sigma \delta_{ij}$, $\sigma_1, \sigma_2, \sigma_3$ are the principal values of the stress tensor.) It is taken of the general form

$$F(\sigma, T, k) \equiv f(\sigma, T) - k \quad (3.11)$$

Upon loading, $F(\sigma_{ij}, k) = 0$ and $F(\sigma_{ij} + d\sigma_{ij}, k + dk) = 0$.

Thus,

$$dF = \frac{\partial F}{\partial \sigma_{ij}} d\sigma_{ij} + \frac{\partial F}{\partial k} dk = \frac{\partial f}{\partial \sigma_{ij}} d\sigma_{ij} - dk = 0$$

therefore

$$dk = \frac{\partial f}{\partial \sigma_{ij}} d\sigma_{ij} \quad (3.12)$$

The plastic increment of strain $d\epsilon_{ij}^p$ is written as

$$d\epsilon_{ij}^p = de_{ij}^p + \frac{1}{3} d\epsilon^p \delta_{ij} \quad (3.13)$$

with de_{ij}^p (the plastic increment of deviatoric strain) and $d\epsilon^p$ (the plastic increment of volumetric strain) given by:

$$de_{ij}^p = \frac{1}{H} dk \frac{S_{ij}}{2T} \quad (3.14a)$$

$$d \epsilon^D = \frac{1}{H} d k \beta \quad (3.14b)$$

with H and β , in general, functions of σ and T .

In order to describe the physical meaning of H and β , it is convenient to define the intensity of the increment of inelastic shear distortion $d e^D$ as:

$$d e^D = [2 d e_{k\ell}^D d e_{k\ell}^D]^{1/2} \quad (3.15)$$

Using Eq. (3.14a), it may be seen that, during loading, H must be positive, since $d k > 0$, $T > 0$ and $d e_{ij}^D$ is taken in the same direction as S_{ij} . It is easily obtained that

$$d e_{k\ell}^D d e_{k\ell}^D = \left[\frac{d k}{H} \right]^2 \frac{S_{k\ell} S_{k\ell}}{4 T^2}.$$

Since $T^2 = \frac{1}{2} S_{k\ell} S_{k\ell}$, it follows that

$$2 d e_{k\ell}^D d e_{k\ell}^D = \left[\frac{d k}{H} \right]^2$$

and

$$[2 d e_{k\ell}^D d e_{k\ell}^D]^{1/2} = \frac{d k}{H}.$$

Finally,

$$d e^P = \frac{d k}{H} . \quad (3.16)$$

Since $d k$ may be understood as an increment of loading and $d e^P$ is the intensity of the increment of plastic shear distortion, H may be interpreted as a plastic shear modulus.

Combining equations (3.14b) and (3.16), it follows that

$$d \epsilon^P = \beta d e^P . \quad (3.17)$$

Thus β may be understood as the ratio of inelastic volumetric deformation to inelastic shear deformation. It is referred to as the inelastic dilatancy factor. Since $d e^P > 0$, $\beta < 0$ means inelastic contraction and $\beta > 0$ means inelastic dilatancy.

The yield function F must exhibit what is sometimes referred to as pressure sensitivity of inelastic behavior. Thus, it is assumed that as magnitude of the hydrostatic stress $|\sigma|$ increases, the shearing stress intensity for which inelastic behavior may occur, also increases. A typical yield surface in σ - T space is shown in Fig. 3.1. The parameter k is also known as the hardening parameter and, if the state of stress is on the yield surface, it is related to σ and T through the equation $F = 0$ (Eq. (3.11)).

Thus, H and β may be taken as functions of (σ, T) , (σ, k) or (T, k) equivalently. However, since ultimate strength of the material is obtained when k reaches a limit value, it is more convenient to take

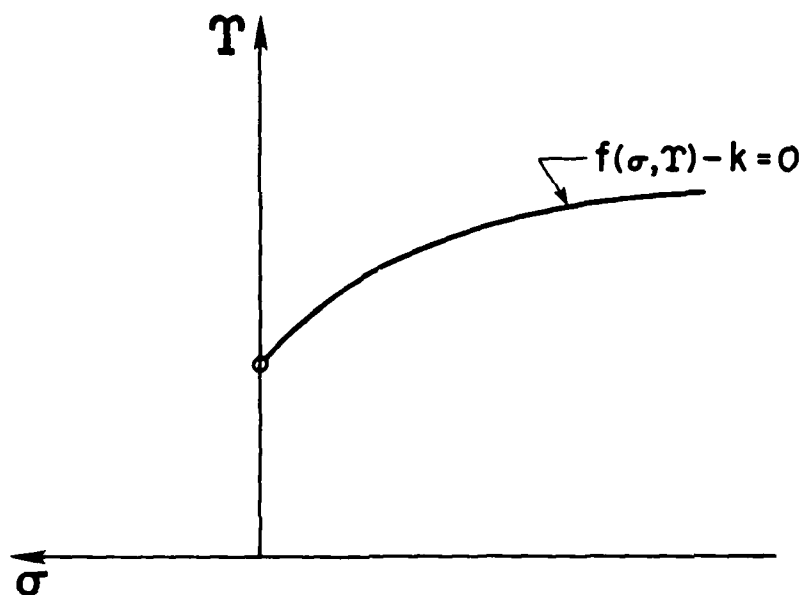


Fig. 3.1. Typical yield surface in $\sigma - T$ space

H and β as functions of (T, k) or (σ, k) rather than (σ, T) since k provides a measure of the proximity of the state of the material to the ultimate strength.

3.3 Constitutive Equations

Eqs. (3.14) may be rewritten as:

$$d \epsilon_{ij}^p = C_{ijkl}^p d \sigma_{kl} \quad (3.18)$$

The plastic compliance tensor C_{ijkl}^p is obtained using Eq. (3.12):

$$\begin{aligned} d\epsilon_{kl} &= \left[\frac{\partial f}{\partial \sigma_{kl}} d\sigma_{kl} \right] \\ &= \left[\frac{\partial f}{\partial S_{kl}} dS_{kl} + \frac{\partial f}{\partial \sigma} d\sigma \right] \\ &= \left[\frac{\partial f}{\partial T} \frac{S_{kl}}{2T} dS_{kl} + \frac{\partial f}{\partial \sigma} d\sigma \right] \end{aligned}$$

Since

$$S_{kl} = \sigma_{kl} - \sigma \delta_{kl}$$

and

$$dS_{kl} = d\sigma_{kl} - d\sigma \delta_{kl}$$

it is seen that

$$d\epsilon_{kl} = \left[\frac{\partial f}{\partial T} \frac{S_{kl}}{2T} d\sigma_{kl} - \frac{\partial f}{\partial T} \frac{S_{kl}}{2T} d\sigma \delta_{kl} + \frac{\partial f}{\partial \sigma} d\sigma \right]$$

However,

$$\frac{\partial f}{\partial T} \frac{S_{kl}}{2T} d\sigma \delta_{kl} = 0$$

and

$$d\sigma = \frac{1}{3} d\sigma_{kl} \delta_{kl}.$$

therefore,

$$d\epsilon_{ij} = \left[\frac{\partial f}{\partial T} \frac{S_{ij}}{2T} + \frac{1}{3} \frac{\partial f}{\partial \sigma} \delta_{ij} \right] d\sigma_{kl}.$$

It follows from Eqs. (3.13) and (3.14) that:

$$C_{ijkl}^p = \frac{1}{H} \left[\frac{S_{ij}}{2T} + \frac{1}{3} \beta \delta_{ij} \right] \left[\frac{\partial f}{\partial T} \frac{S_{kl}}{2T} + \frac{1}{3} \frac{\partial f}{\partial \sigma} \delta_{kl} \right] \quad (3.19)$$

In general, $C_{ijkl}^p \neq C_{klij}^p$.

Finally, the incremental constitutive equations corresponding to loading may be written as

$$d\epsilon_{ij} = C_{ijkl} d\sigma_{kl} \quad (3.20)$$

with

$$C_{ijkl} = C_{ijkl}^e + C_{ijkl}^p.$$

Again, in general, $C_{ijkl} \neq C_{klij}$.

In the cases of unloading and neutral loading, the compliance tensor C_{ijkl} is equal to the elastic compliance tensor C_{ijkl}^e and the increment of strain $d\epsilon_{ij}$ is given by:

$$d \varepsilon_{ij} = C_{ijkl}^e d\sigma_{kl} \quad (3.21)$$

3.4 Parameter Estimation

The yield function F has been taken of the general form:

$$F(\sigma, T, k) \equiv f(\sigma, T) - k \quad (3.11)$$

A simple special case of Eq. (3.11) is:

$$F(\sigma, T, k) \equiv A_1\sigma + A_2T + A_3 - k = 0$$

Using the following conditions,

- 1) $\sigma_1 = -|f'_c|$; $\sigma_2 = \sigma_3 \approx 0$ and $k = 1$
- 2) $\sigma_1 = \sigma_2 = -1.16 |f'_c|$; $\sigma_3 = 0$ and $k = 1$
- 3) $\sigma_1 = -0.40 |f'_c|$; $\sigma_2 = \sigma_3 = 0$ and $k = 0$,

the values of A_1 , A_2 and A_3 may be found. Thus

$$F(\sigma, T, k) \equiv 0.69 \frac{\sigma}{|f'_c|} + 3.285 \frac{T}{|f'_c|} - 0.0667 - k \quad (3.22)$$

(f'_c is the strength of the material in uniaxial compression.)

Conditions 1, 2 and 3 represent, respectively,

- 1) ultimate strength in uniaxial compression.
- 2) ultimate strength in equal biaxial compression. (The factor 1.16 allows for the increase in strength under combined compressive stresses.)
- 3) Initial yielding in uniaxial compression.

The parameter k can assume values between 0 (initial yielding) and 1 (ultimate strength). Thus, it can be used as an indicator of the proximity of the yield surface to the material ultimate strength. A graphical representation of the yield function (3.22) in $\sigma_1 - \sigma_2$ space and in $\sigma - T$ space is shown in Figs. 3.2 and 3.3 respectively.

The plastic shear modulus H will be taken to be a function of the magnitude of the hydrostatic stress $|\sigma|$ and the hardening parameter k . As shown in Figs. 3.1 and 3.3, the yield function used in this study is such that the shearing stress intensity T increases as the magnitude of the hydrostatic stress $|\sigma|$ increases. Since more inelastic shear deformation is obtained under higher shear loading (higher T), it follows that H must be a decreasing function of T and hence of $|\sigma|$.

Using Eq. (3.16) and calculating the values of $d k$ and de^P from stress-strain curves measured in uniaxial compression tests, the values of H shown in Table 3.1 were obtained. Within each interval, H is assumed to vary as follows:

$$H = \frac{1}{a + b k}$$

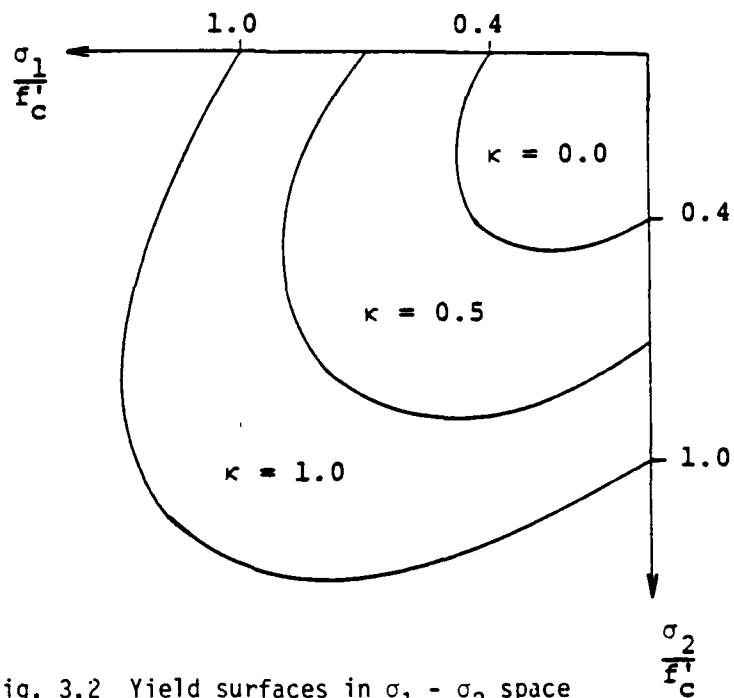


Fig. 3.2 Yield surfaces in $\sigma_1 - \sigma_2$ space

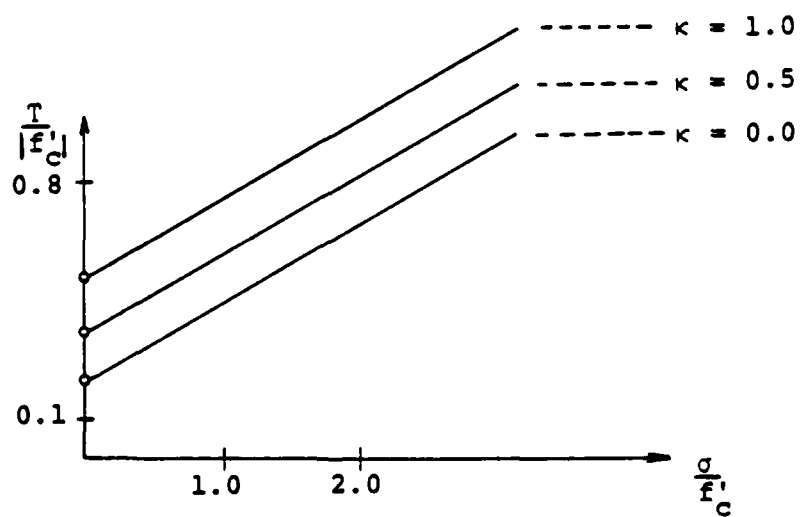


Fig. 3.3 Yield surfaces in $\sigma - T$ space

Table 3.1 Relationship between k and H in uniaxial compression

<u>k</u>	<u>H (psi)</u>
0	16,000
0.35	4,870
0.50	2,800
0.70	1,600
1.00	575

The values of a and b may be calculated for each interval yielding the expressions in Table 3.2.

Table 3.2 Expressions for H as a function of k in uniaxial compression.

<u>k</u>	<u>H (psi)</u>
$0 \leq k \leq 0.35$	$H = 1/(4.081 \times 10^{-4}k + 6.250 \times 10^{-5})$
$0.35 \leq k \leq 0.50$	$H = 1/(1.012 \times 10^{-3}k - 1.489 \times 10^{-4})$
$0.50 \leq k \leq 0.70$	$H = 1/(1.339 \times 10^{-3}k - 3.125 \times 10^{-4})$
$0.70 \leq k \leq 1.00$	$H = 1/(3.714 \times 10^{-3}k - 1.975 \times 10^{-3})$

In uniaxial compression ($\sigma_1 < 0, \sigma_2 = \sigma_3 = 0$):

$$\sigma = -\frac{1}{3} |\sigma_1|$$

and

$$T = \frac{1}{\sqrt{3}} |\sigma_1| .$$

Using the yield function given by Eq. (3.22), it is seen that, beyond the initial yielding,

$$|\sigma_1| = \frac{2 + 3 k}{5} |f'_c|$$

and therefore

$$\left| \frac{\sigma}{f'_c} \right| = \frac{2 + 3 k}{15}$$

or

$$\frac{2 + 3 k}{\left| \frac{\sigma}{f'_c} \right|} = 15.$$

In order to generalize the results given in Table 3.2 and obtain expressions for H valid for any state of stress, the values of H in uniaxial compression were divided by 15 and multiplied by

$$\frac{2 + 3 k}{\left| \frac{\sigma}{f'_c} \right|}$$

Thus, the expressions for H shown in Table 3.3 were determined.

Table 3.3 Expressions for H under multiaxial states of stress ($C = (2 + 3k)/|\sigma/f'_c|$).

k	H (psi)
$0 \leq k \leq 0.35$	$H = C/(6.122 \times 10^{-3}k + 9.375 \times 10^{-4})$
$0.35 \leq k \leq 0.50$	$H = C/(1.518 \times 10^{-2}k - 2.234 \times 10^{-3})$
$0.50 \leq k \leq 0.70$	$H = C/(2.009 \times 10^{-2}k - 4.688 \times 10^{-3})$
$0.70 \leq k \leq 1.0$	$H = C/(5.571 \times 10^{-2}k - 2.963 \times 10^{-2})$

The inelastic dilatancy factor β will be taken to be a function of the parameter k only. A more elaborate analysis could include the effect of the hydrostatic stress σ in the expressions for β .

Using Eq. (3.17) and calculating the value of $d\epsilon^D$ and $d\epsilon^P$ from stress-strain curves measured in uniaxial compression tests, the value of β shown in Table 3.4 were obtained.

In order to check the accuracy of the expressions for H and β shown in Tables 3.2 and 3.4 respectively, the stress-strain curve in uniaxial compression used to obtain the two parameters was reproduced and the comparison is shown in Fig. 3.4.

Table 3.4 Relationship between k and β in uniaxial compression.

k	β
$0 \leq k \leq 0.135$	$\beta = -49.60k + 2.92$
$0.135 \leq k \leq 0.219$	$\beta = 66.31k - 12.73$
$0.219 \leq k \leq 0.354$	$\beta = -14.44k + 4.95$
$0.354 \leq k \leq 0.521$	$\beta = -3.05k + 0.92$
$0.521 \leq k \leq 0.615$	$\beta = 8.09k - 4.88$
$0.615 \leq k \leq 0.708$	$\beta = -9.89k + 6.17$
$0.708 \leq k \leq 0.792$	$\beta = 15.12k - 11.53$
$0.792 \leq k \leq 0.875$	$\beta = -11.81k + 9.79$
$0.875 \leq k \leq 1.0$	$\beta = 8.32k - 7.82$

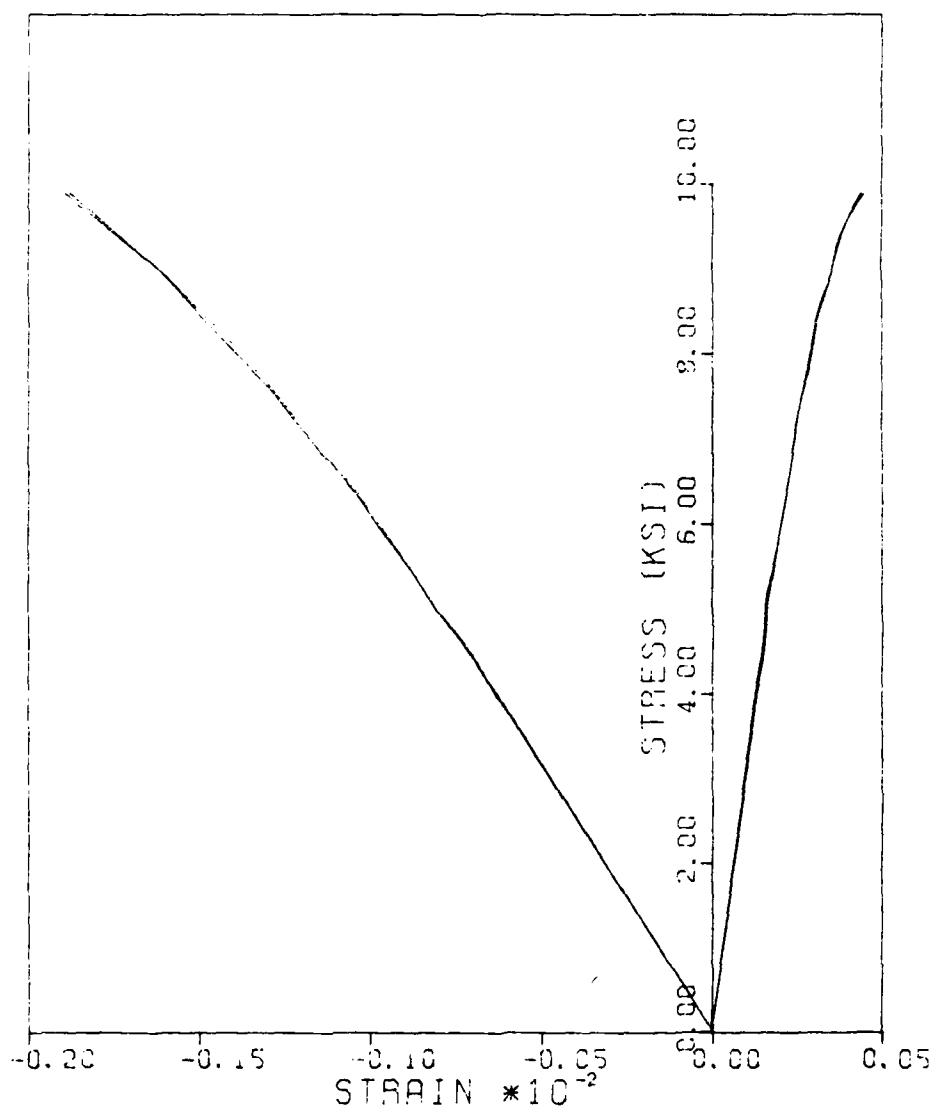


Fig. 3.4 Stress-strain curves for mortar in uniaxial compression-- comparison between test results and the model.

CHAPTER 4

THE FINITE ELEMENT ANALYSIS OF THE CONCRETE MODEL

4.1 Introduction

The concrete model to be analyzed in this study is shown in Figure 2.1. The coarse aggregate will be assumed to be elastic up to ultimate strength since test results in uniaxial compression showed that this is true to a very good approximation. Inelastic deformation in the mortar will be taken into account using the constitutive model described in Chapter 3.

As the model and the loading are symmetric about the two orthogonal axes, it is necessary to analyze one quadrant only. A discretization of this quadrant by finite elements is shown in Fig. 4.1. As it may be seen, a six-node element is used to represent the coarse aggregate and an eight-node element is used to represent the mortar.

The objective of this chapter is to describe the linear and nonlinear finite element analysis of the concrete model.

4.2 Linear Analysis

This section describes the analysis of the concrete model assuming both materials (aggregate and mortar) to be isotropic and elastic. Section 4.3 will describe the nonlinear analysis, i.e., the analysis accounting for the nonlinear behavior of the mortar.

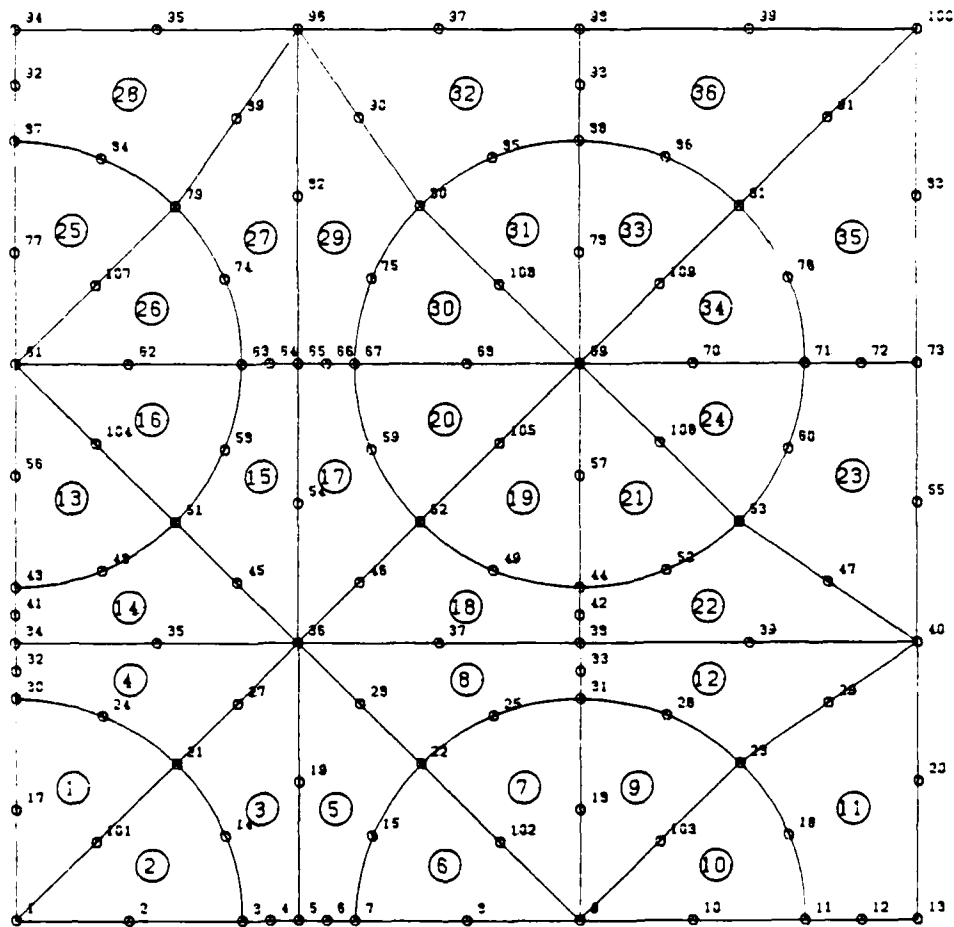


Fig. 4.1 Discretization of the concrete model by finite elements.

The linear analysis may be described briefly as follows:

Step 1. Given the elastic properties of the materials, a relationship between nodal forces and nodal displacements for each element is found:

$$\underline{\underline{F}}^i = \underline{\underline{K}}^i \underline{\underline{U}}^i$$

where

$$\underline{\underline{F}}^i = [x_1^i, y_1^i, x_2^i, y_2^i, \dots, x_m^i, y_m^i]^T$$

$$\underline{\underline{U}}^i = [u_1, v_1, u_2, v_2, \dots, u_m, v_m]^T$$

The superscript T indicates that the transpose of the superscripted matrix must be taken. x_j^i and y_j^i are the forces, in the x and y directions, respectively, applied at node j of element i. u_j and v_j are the displacements, in the x and y directions, respectively, of node j. m is the number of nodes of the element. $\underline{\underline{K}}^i$ is the stiffness matrix of element i.

Step 2. The element stiffness matrix $\underline{\underline{K}}^i$ and the load vector $\underline{\underline{F}}^i$ are modified for the support conditions.

Step 3. A relationship between nodal forces and nodal displacements for the structure is found, i.e., the structure stiffness matrix is assembled from the element stiffness matrices:

$$\underline{\underline{F}} = \underline{\underline{K}} \underline{\underline{U}}$$

$$\underline{\underline{F}} = [X_1, Y_1, X_2, Y_2, \dots, X_p, Y_p]^T$$

$$\underline{\underline{U}} = [u_1, v_1, u_2, v_2, \dots, u_p, v_p]^T$$

X_j and Y_j are the forces, in x and y directions respectively, applied at node j. p is the number of nodes in the structure. $\underline{\underline{K}}$ is the stiffness matrix of the structure.

Step 4. The system of equations for the displacements is solved using Gauss elimination. Formally:

$$\underline{\underline{U}} = [\underline{\underline{K}}]^{-1} \underline{\underline{F}}$$

Step 5. After the displacements are determined, it is possible to find strains and, therefore, stresses at any point in the structure. In each element, some points also used in the calculation of the element stiffness matrix (integration points) are chosen.

4.2.1 Derivation of the Element Stiffness Matrix. The finite elements used in this study are called isoparametric. The same interpolation functions used to relate the coordinates of any point, within the element, to the coordinates of the element nodes are also used to relate the displacements of any point, within the element, to the displacements of the element nodes. Thus:

$$x = \sum_{j=1}^m N_j x_j \quad (4.1a)$$

$$y = \sum_{j=1}^m N_j y_j \quad (4.1b)$$

$$u = \sum_{j=1}^m N_j u_j \quad (4.2a)$$

$$v = \sum_{j=1}^m N_j v_j \quad (4.2b)$$

x, y are the coordinates of any point within the element. x_j, y_j are the coordinates of node j . u, v , are the displacements of any point within the element. u_j, v_j are the displacements of node j . N_j is the interpolation function corresponding to node j .

An interpolation function assumes a value equal to one when evaluated at its corresponding node and a value equal to zero when evaluated at any other node. For example, the interpolation functions used for the eight-node element (see Fig. 4.2) are given by

$$N_1 = -1/4(r + s + 1) (1 - s) (1 - r)$$

$$N_2 = 1/4(r - s - 1) (1 - s) (1 + r)$$

$$N_3 = 1/4(r + s - 1) (1 + s) (1 + r)$$

$$N_4 = -1/4(r - s + 1) (1 + s) (1 - r)$$

$$N_5 = 1/2(1 - s) (1 + r) (1 - r)$$

$$N_6 = 1/2(1 - s) (1 + s) (1 + r)$$

$$N_7 = 1/2(1 + s) (1 + r) (1 - r)$$

$$N_8 = 1/2(1 + s) (1 - s) (1 - r)$$

r, s being local coordinates as indicated in Fig. 4.2.

There is a one-to-one correspondence between points in the square in Fig. 4.2 and the eight-node element shown in Fig. 4.1. It is the interpolation used in Eqs. (4.1) and (4.2) that allows the use of curved elements such as the ones shown in Fig. 4.1.

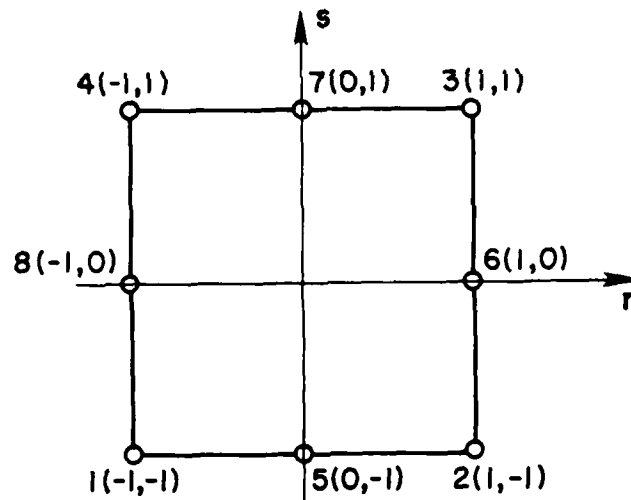


Fig. 4.2 Local system of coordinates for the eight-node element.

If small displacements are assumed, the strains at any point in the body are given by

$$\epsilon_x = \frac{\partial u}{\partial x}, \quad \epsilon_y = \frac{\partial v}{\partial y}$$

and

$$\gamma_{xy} = \frac{\partial u}{\partial y} + \frac{\partial v}{\partial x} \quad (4.3)$$

and, using Eq. (4.2),

$$\epsilon_x = \sum_{j=1}^m \frac{\partial N_j}{\partial x} u_j, \quad \epsilon_y = \sum_{j=1}^m \frac{\partial N_j}{\partial y} v_j$$

and

$$\gamma_{xy} = \sum_{j=1}^m \left[\frac{\partial N_j}{\partial y} u_j + \frac{\partial N_j}{\partial x} v_j \right] \quad (4.4)$$

The partial derivatives of the interpolation functions with respect to x and y may be calculated from

$$\begin{aligned} \frac{\partial N_j}{\partial r} &= \frac{\partial N_j}{\partial x} \frac{\partial x}{\partial r} + \frac{\partial N_j}{\partial y} \frac{\partial y}{\partial r} \\ \frac{\partial N_j}{\partial s} &= \frac{\partial N_j}{\partial x} \frac{\partial x}{\partial s} + \frac{\partial N_j}{\partial y} \frac{\partial y}{\partial s} \end{aligned}$$

In matrix form

$$\begin{bmatrix} \frac{\partial N_j}{\partial r} \\ \frac{\partial N_j}{\partial s} \end{bmatrix} = \begin{bmatrix} \frac{\partial x}{\partial r} & \frac{\partial y}{\partial r} \\ \frac{\partial x}{\partial s} & \frac{\partial y}{\partial s} \end{bmatrix} \begin{bmatrix} \frac{\partial N_j}{\partial x} \\ \frac{\partial N_j}{\partial y} \end{bmatrix} = \tilde{J} \begin{bmatrix} \frac{\partial N_j}{\partial x} \\ \frac{\partial N_j}{\partial y} \end{bmatrix}$$

\tilde{J} is known as the Jacobian Matrix and can be derived as a function of r and s using Eq. (4.1).

$$\tilde{J} = \begin{bmatrix} \sum_{j=1}^m \frac{\partial N_j}{\partial r} x_j & \sum_{j=1}^m \frac{\partial N_j}{\partial r} y_j \\ \sum_{j=1}^m \frac{\partial N_j}{\partial s} x_j & \sum_{j=1}^m \frac{\partial N_j}{\partial s} y_j \end{bmatrix} \quad (4.5)$$

Thus, given the coordinates r and s of a point in local coordinates, $\frac{\partial N_j}{\partial x}$ and $\frac{\partial N_j}{\partial y}$ can be found, for the corresponding point in the body:

$$\begin{bmatrix} \frac{\partial N_j}{\partial x} \\ \frac{\partial N_j}{\partial y} \end{bmatrix} = [\tilde{J}]^{-1} \begin{bmatrix} \frac{\partial N_j}{\partial r} \\ \frac{\partial N_j}{\partial s} \end{bmatrix} \quad (4.6)$$

The relationship between the strains at any point in the body and the nodal displacements may be written, in matrix form, as:

$$\underline{\underline{\varepsilon}} = \underline{\underline{B}} \underline{\underline{U}}^i \quad (4.7)$$

where

$$\underline{\underline{\varepsilon}} = [\varepsilon_x, \varepsilon_y, \gamma_{xy}]^T$$

$$\underline{\underline{U}}^i = [u_1, v_1, u_2, v_2, \dots, u_m, v_m]^T$$

$$\underline{\underline{B}} = \begin{bmatrix} \frac{\partial N_1}{\partial x} & 0 & \frac{\partial N_2}{\partial x} & 0 & \dots & \frac{\partial N_m}{\partial x} & 0 \\ 0 & \frac{\partial N_1}{\partial y} & 0 & \frac{\partial N_2}{\partial y} & \dots & 0 & \frac{\partial N_m}{\partial y} \\ \frac{\partial N_1}{\partial y} & \frac{\partial N_1}{\partial x} & \frac{\partial N_2}{\partial y} & \frac{\partial N_2}{\partial x} & \dots & \frac{\partial N_m}{\partial y} & \frac{\partial N_m}{\partial x} \end{bmatrix}$$

After the strains, the stresses can be calculated (assuming a plane state of stress with $\sigma_z = \tau_{xz} = \tau_{yz} = 0$) as

$$\underline{\underline{\sigma}} = \underline{\underline{D}} \underline{\underline{\varepsilon}} \quad (4.8)$$

where

$$\underline{\underline{\sigma}} = [\sigma_x, \sigma_y, \tau_{xy}]^T$$

$$\underline{\underline{D}} = \frac{E}{1-\nu^2} \begin{bmatrix} 1 & \nu & 0 \\ \nu & 1 & 0 \\ 0 & 0 & \frac{1-\nu}{2} \end{bmatrix}$$

The principle of minimum potential energy yields the stiffness matrix of an element (for example, see Ref. 6):

$$\underline{\underline{K}}^i = \int_{\text{element volume}} \underline{\underline{B}}^T \underline{\underline{D}} \underline{\underline{B}} \, dv \quad (4.9)$$

The integration in Eq. (4.9) is conveniently carried out numerically. In this analysis, Gaussian integration is employed. Nine integration points have been used for the eight-node elements and seven integration points for the six-node elements. The integration points in the eight-node element in local coordinates are shown in Fig. 4.3.

The matrix multiplication in Eq. (4.9) may be organized as follows:

Calling,

$$\underline{\underline{B}}_j = \begin{bmatrix} \frac{\partial N_j}{\partial x} & 0 \\ 0 & \frac{\partial N_j}{\partial y} \\ \frac{\partial N_j}{\partial y} & \frac{\partial N_j}{\partial x} \end{bmatrix}$$

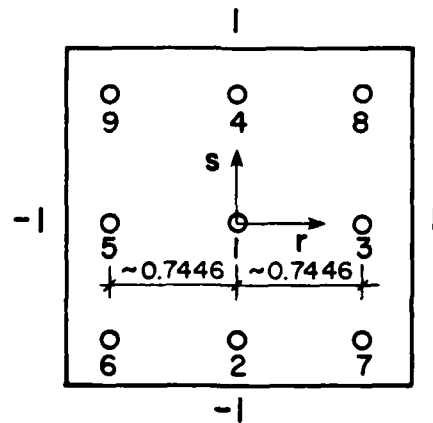


Fig. 4.3 Integration points for the eight-node element in local coordinates.

so that,

$$\underline{\underline{B}} = [\underline{\underline{B}}_1, \underline{\underline{B}}_2, \dots, \underline{\underline{B}}_m]$$

$$\underline{\underline{B}}^T = [\underline{\underline{B}}_1^T, \underline{\underline{B}}_2^T, \dots, \underline{\underline{B}}_m^T]^T$$

and using Eq. (4.9):

$$\tilde{K}^i = \sum_{\ell=1}^q w_{\ell} \begin{bmatrix} \tilde{B}_1^T \tilde{D} \tilde{B}_1 & \tilde{B}_1^T \tilde{D} \tilde{B}_2 & \cdots & \tilde{B}_1^T \tilde{D} \tilde{B}_m \\ \tilde{B}_2^T \tilde{D} \tilde{B}_1 & \tilde{B}_2^T \tilde{D} \tilde{B}_2 & \cdots & \tilde{B}_2^T \tilde{D} \tilde{B}_m \\ \vdots & \vdots & \ddots & \vdots \\ \tilde{B}_m^T \tilde{D} \tilde{B}_1 & \tilde{B}_m^T \tilde{D} \tilde{B}_2 & \cdots & \tilde{B}_m^T \tilde{D} \tilde{B}_m \end{bmatrix} \quad (4.10)$$

q being the number of integration points. The weight of integration point ℓ is denoted by w_{ℓ} .

The matrix in Eq. (4.10) is symmetric, if \tilde{D} is symmetric as in Eq. (4.8).

4.2.2 Modification of the Element Stiffness Matrix for

Support Conditions. The stiffness matrix derived above relates the forces at the nodes of an element to the corresponding displacements. These displacements are the degrees of freedom. If a displacement is prescribed, it is not considered a degree of freedom and the corresponding column and row in the stiffness matrix \tilde{K}^i are deleted after the column multiplied by the prescribed value is subtracted from the load vector. Thus, for example, if the displacement in the y -direction of node 1, v_1 , is prescribed equal to \bar{v}_1 , the element stiffness matrix will be modified as follows:

$$\begin{bmatrix} X_1^i \\ Y_1^i \\ X_2^i \\ Y_2^i \\ \cdot \\ \cdot \\ \cdot \\ \cdot \\ X_m^i \end{bmatrix} = \begin{bmatrix} k_{1,1} & k_{1,2} & k_{1,3} & k_{1,4} & \cdot & \cdot & \cdot & k_{1,2m} \\ k_{2,1} & k_{2,2} & k_{2,3} & k_{2,4} & \cdot & \cdot & \cdot & k_{2,2m} \\ k_{3,1} & k_{3,2} & k_{3,3} & k_{3,4} & \cdot & \cdot & \cdot & k_{3,2m} \\ k_{4,1} & k_{4,2} & k_{4,3} & k_{4,4} & \cdot & \cdot & \cdot & k_{4,2m} \\ \cdot & \cdot & \cdot & \cdot & & & & \cdot \\ \cdot & \cdot & \cdot & \cdot & & & & \cdot \\ \cdot & \cdot & \cdot & \cdot & & & & \cdot \\ \cdot & \cdot & \cdot & \cdot & & & & \cdot \\ k_{2m,1} & k_{2m,2} & k_{2m,3} & k_{2m,4} & \cdot & \cdot & \cdot & k_{2m,2m} \end{bmatrix} \begin{bmatrix} u_1 \\ \bar{v}_1 \\ u_2 \\ v_2 \\ \cdot \\ \cdot \\ \cdot \\ \cdot \\ v_m \end{bmatrix}$$

$$\begin{bmatrix} X_1^i - k_{1,2} \bar{v}_1 \\ X_2^i - k_{3,2} \bar{v}_1 \\ Y_2^i - k_{4,2} \bar{v}_1 \\ \cdot \\ \cdot \\ \cdot \\ \cdot \\ Y_m^i - k_{2m,2} \bar{v}_1 \end{bmatrix} = \begin{bmatrix} k_{1,1} & k_{1,3} & k_{1,4} & \cdot & \cdot & \cdot & k_{1,2m} \\ k_{3,1} & k_{3,3} & k_{3,4} & \cdot & \cdot & \cdot & k_{3,2m} \\ k_{4,1} & k_{4,3} & k_{4,4} & \cdot & \cdot & \cdot & k_{4,2m} \\ \cdot & \cdot & \cdot & & & & \cdot \\ \cdot & \cdot & \cdot & & & & \cdot \\ \cdot & \cdot & \cdot & & & & \cdot \\ \cdot & \cdot & \cdot & & & & \cdot \\ k_{2m,1} & k_{2m,3} & k_{2m,4} & & & & k_{2m,2m} \end{bmatrix} \begin{bmatrix} u_1 \\ u_2 \\ v_2 \\ \cdot \\ \cdot \\ \cdot \\ \cdot \\ v_m \end{bmatrix}$$

In this way, a support is introduced at node 1 in the y-direction and the force Y_1^i becomes the reaction at this support.

Another modification in the load vector and element stiffness matrix must be introduced in this analysis to take into account the fact that some degrees of freedom may be the same. For example, if the load is applied to the specimen shown in Fig. 2.1 using rigid platens, it is reasonable to assume equal displacements for all nodes located along the contact edge of the specimen in the direction of the applied load. Thus, all degrees of freedom can be condensed in a single one since they are all the same. The process of condensation may be described by the following example. Suppose that the degrees of freedom v_1 and v_2 are the same and it is desired to condense them in a single degree of freedom, say, v_1 . To accomplish this it is necessary to make the following modifications in the element stiffness matrix and load vector. The column and row corresponding to the degree of freedom v_2 must be added to the column and row corresponding to the degree of freedom v_1 . The column and row corresponding to the degree of freedom v_2 is then deleted. Thus,

$$\begin{bmatrix} x_1^i \\ y_1^i + y_2^i \\ x_2^i \\ x_3^i \\ y_3^i \\ \vdots \\ y_m^i \end{bmatrix} = \begin{bmatrix} k_{1,1} & (k_{1,2} + k_{1,4}) & k_{1,3} & \dots & k_{1,2m} \\ (k_{2,1} + k_{4,1}) & (k_{2,2} + 2k_{2,4}) & (k_{2,3} + k_{4,3}) & \dots & (k_{2,2m} + k_{4,2m}) \\ k_{3,1} & (k_{3,2} + k_{3,4}) & k_{3,3} & \dots & k_{3,2m} \\ k_{5,1} & (k_{5,2} + k_{5,4}) & k_{5,3} & \dots & k_{5,2m} \\ k_{6,1} & (k_{6,2} + k_{6,4}) & k_{6,3} & \dots & k_{6,2m} \\ \vdots & \vdots & \vdots & \ddots & \vdots \\ k_{2m,1} & (k_{2m,2} + k_{2m,4}) & k_{2m,3} & \dots & k_{2m,2m} \end{bmatrix} \begin{bmatrix} u_1 \\ v_1 \\ u_2 \\ u_3 \\ v_3 \\ \vdots \\ v_m \end{bmatrix}$$

Note that the remaining stiffness matrix is still symmetric, if the original matrix is symmetric.

Since, sometimes, there are some degrees of freedom which are the same but, in addition belong to different elements, a trick is used to overcome the difficulty. A one-degree-of-freedom node number is created in the program for each set of degrees of freedom to be condensed. An element node number corresponds to a structure node number. For example, the node number 1 of element 28, see Fig. 4.1, corresponds to node number 87 in the structure. Thus, in the program, the sets of degrees of freedom to be condensed are forced to correspond to the created node number and, therefore, during the process of assembly and solution of the system of equations, only one degree of freedom will be processed.

4.2.3 Assembly and Solution of the Structure System of Equations. The assembly and solution of the structure system of equations is a straightforward process. A detailed description of this process is not of interest in this study and therefore only a brief presentation will be given here. (See Ref. 7 for more information).

The Frontal Solution Method is used. In this method the assembly and Gauss elimination are performed at the same time, whereas in the usual solution method the stiffness matrix for the structure is first assembled and then Gauss elimination is carried out.

If, as elements are processed one after the other, a node appears for the last time, the degrees of freedom associated with the node may be eliminated and the corresponding equations are removed

and saved. After the last element has been processed, back-substitution yields the nodal displacements. Note that in the Frontal Solution Method it is element numbering that is crucial and not node numbering. The method is known to be more efficient than the more common band solvers, if elements with midside nodes are used as in the present analysis (see Ref. 7).

4.2.4 Calculation of Stresses and Strains in the Body. As explained in section 4.2.1, if the nodal displacements of an element are known, the strains and stresses at any point within the element can be calculated using Eqs. (4.7) and (4.8) respectively. In this study, the calculations are carried out at the integration points.

If the stresses at all integration points in the body do not exceed the material elastic limits, the linear analysis is sufficient to obtain the behavior of the concrete model. On the other hand, if, at any integration point, the stresses exceed the material elastic limits, a nonlinear analysis must be performed. This will be discussed in Section 4.3.

4.2.5 Accuracy Test of the Linear Finite Element Analysis.

The problem depicted in Fig. 4.4 was considered in order to check the accuracy of the linear finite element analysis. It involves a circular inclusion in a matrix subjected to uniform tension in one direction. An exact solution of this problem in the case in which tension is applied at an infinite distance away from the inclusion ($\alpha = \infty$) is available in the literature (see Refs. 8, 9). Details of the derivation of the exact solution may be found in these references. The

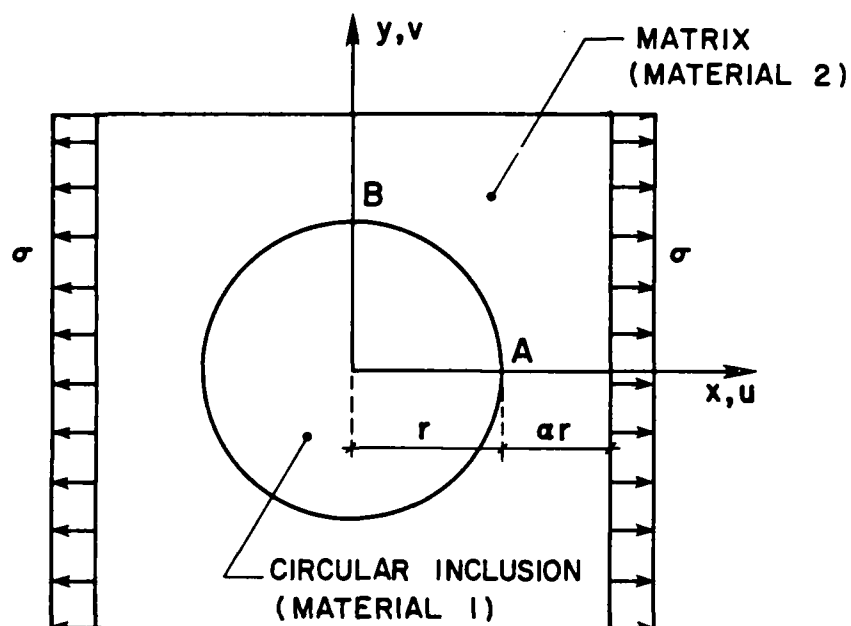


Fig. 4.4 A test in the elastic analysis.

displacements of points A and B were obtained from the exact solution and then using the linear finite element analysis. As it is impossible to apply the tension at an infinite distance away from the inclusion, several finite element analyses were performed for increasing values of α (see Fig. 4.5). The results for two different values of Poisson's ratio for the inclusion are shown in Table 4.1. Good agreement between the results of the finite element analysis and the exact solution may be observed as the value of α is increased. Thus,

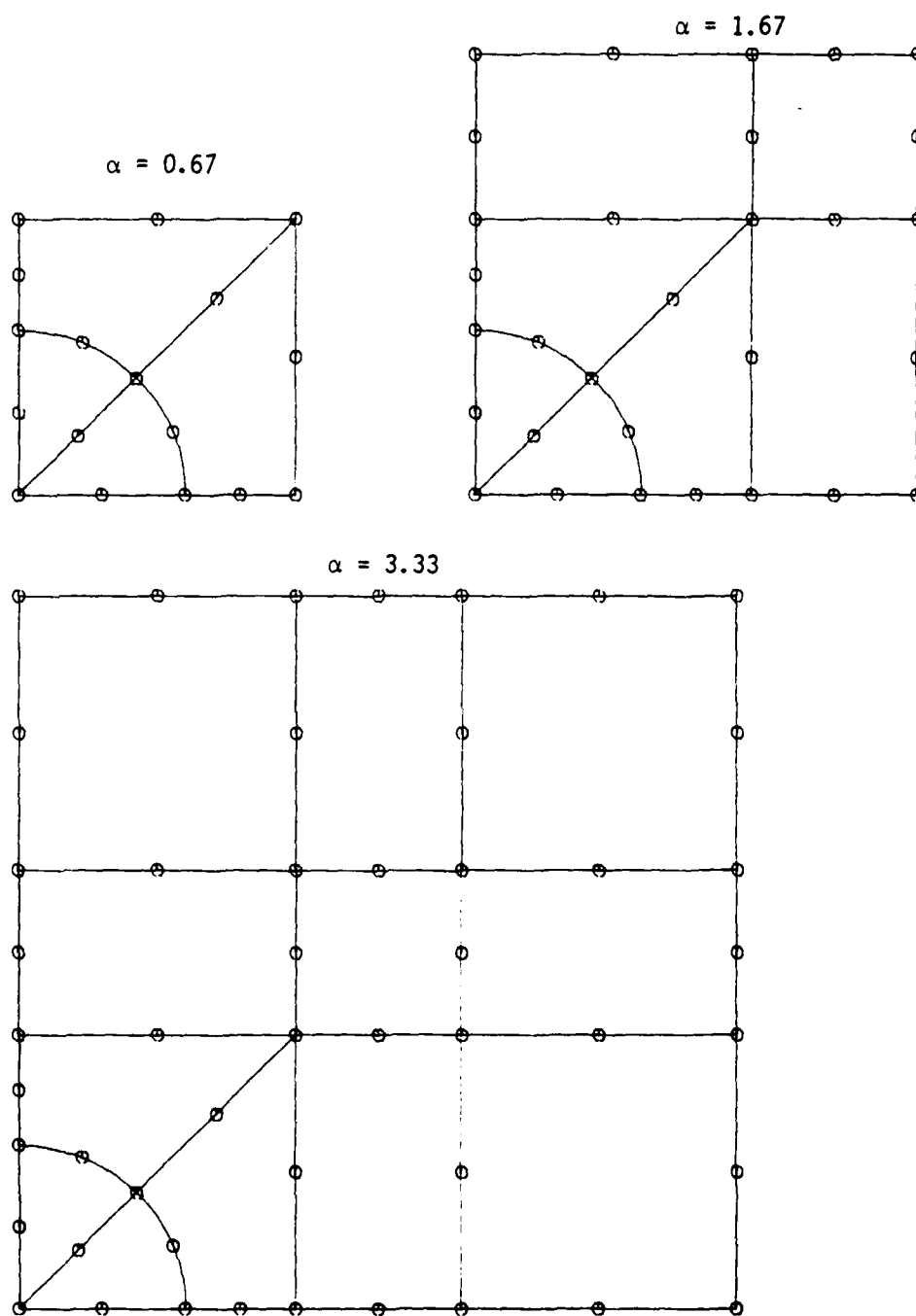


Fig. 4.5 Finite element meshes used in the test analyses.

Table 4.1 Comparison between results of the finite element analysis and the exact solution

$E_1 = 8.4 \times 10^6 \text{ psi} \quad E_2 = 4.7 \times 10^6 \text{ psi} \quad \nu_2 = 0.20$				
$\nu_1 = 0.06$				EXACT SOL.
α	0.67	1.67	3.33	∞
$u_A(\text{in})$	2.23×10^{-3}	2.38×10^{-3}	2.46×10^{-3}	2.51×10^{-3}
$v_B(\text{in})$	-0.18×10^{-4}	-0.94×10^{-4}	-1.41×10^{-4}	-1.75×10^{-4}
$\nu_1 = 0.15$				EXACT SOL.
α	0.67	1.67	3.33	∞
$u_A(\text{in})$	---	2.40×10^{-3}	2.47×10^{-3}	2.52×10^{-3}
$v_B(\text{in})$	---	-2.73×10^{-4}	-3.16×10^{-4}	-3.45×10^{-4}

the finite element meshes shown in Fig. 4.5 yield reasonably accurate results.

4.3 Nonlinear Analysis

The nonlinear analysis is better understood by considering a one-degree-of-freedom structure. Let P be the load applied to the structure. Also let u be the degree of freedom associated with P . The inelastic behavior of this structure is shown in Fig. 4.6. Suppose that for some value of the load P the corresponding displacement u is known. It is desired to find the increment of displacement Δu

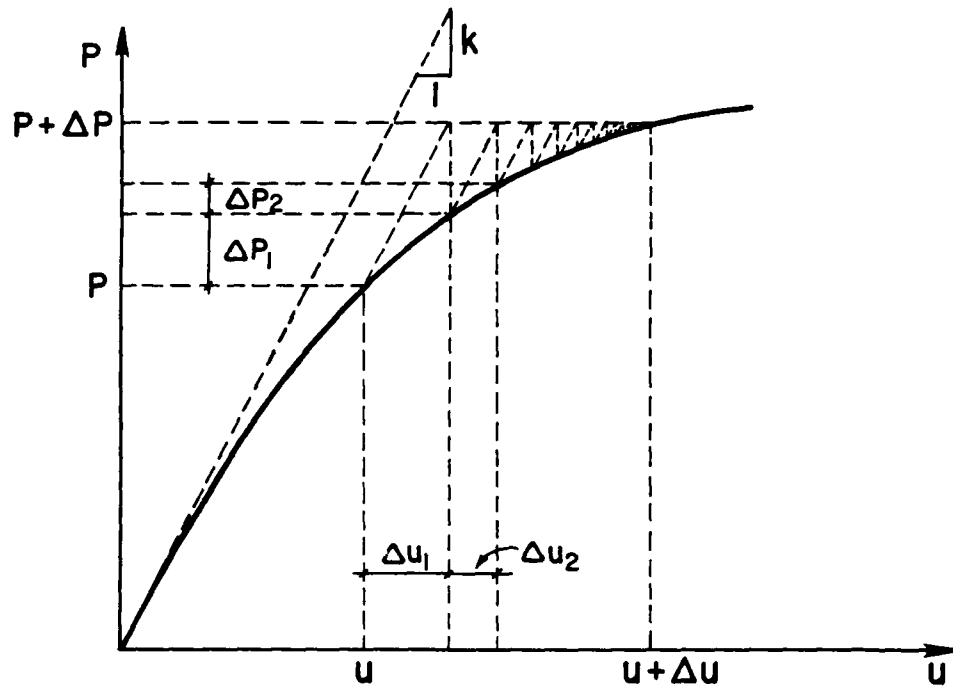


Fig. 4.6 P vs. u diagram for a one-degree-of-freedom structure

associated with the increment of load ΔP . If, for any given displacement, it is possible to find the corresponding load for structural equilibrium and if the initial elastic stiffness K is known, the problem may be solved iteratively as follows:

Step 1. Assuming that the structure is elastic, the increment of displacement Δu_1 associated with ΔP is found:

$$\Delta u_1 = \frac{\Delta P}{K}$$

Step 2. For the increment of displacement Δu_1 , the corresponding increment of load ΔP_1 for equilibrium is found:

Step 3. The residual increment of load $(\Delta P - \Delta P_1)$ is applied, assuming again elastic behavior, and the increment of displacement Δu_2 is calculated:

$$\Delta u_2 = \frac{(\Delta P - \Delta P_1)}{K}$$

Now repeat steps 2 and 3 until convergence is obtained and the value of $\Delta u = \sum_{i=1}^m \Delta u_i$ is determined, n being the number of iterations.

The procedure described above is usually referred to as the "Constant Stiffness Method". It is used in a similar way in the non-linear analysis of the concrete model shown in Fig. 2.1. Suppose that for some load \underline{P} on the model the nodal displacements \underline{U} as well as the stresses and strains $\underline{\sigma}$ and $\underline{\epsilon}$ at all integration points are known. It is desired to find the increments of nodal displacements $\underline{\Delta U}$ and the increments of stresses and strains $\underline{\Delta \sigma}$ and $\underline{\Delta \epsilon}$ corresponding to some increment of load $\underline{\Delta P}$. The problem is solved as follows:

Step 1. Assuming that the structure is elastic, a linear analysis (as described in Section 4.2) is performed and the increments of nodal displacements $\underline{\Delta U}_1$ associated with the load increment $\underline{\Delta P}$ are found:

$$\underline{\Delta U}_1 = [\underline{K}]^{-1} \underline{\Delta P}$$

Step 2. For each element and at each integration point:

Using $\underline{\Delta U}_1$ and Eq. (4.7) $\underline{\Delta \epsilon}_1$ is found. The increments of stresses using the elastic material properties ($\underline{\Delta \sigma}_1^e = \underline{D} \underline{\Delta \epsilon}_1$, see Eq. (4.8)) are calculated. Using the constitutive equations developed in Chapter 3, the increments of stresses $\underline{\Delta \sigma}_1$ corresponding to $\underline{\Delta \epsilon}_1$ are evaluated. The residual increments of stresses ($\underline{\Delta \sigma}_1^e - \underline{\Delta \sigma}_1$) are determined and then for each element, the corresponding nodal residual forces are calculated. Applying the residual forces, another linear analysis is performed and the increments of nodal displacements $\underline{\Delta U}_2$ are found.

Repeat steps 1 and 2 until a convergence criterion is satisfied.

The increments of nodal displacements, the increments of strains and the increments of stresses are given by:

$$\underline{\Delta U} = \sum_{i=1}^n \underline{\Delta U}_i$$

$$\underline{\Delta \epsilon} = \sum_{i=1}^n \underline{\Delta \epsilon}_i$$

$$\underline{\Delta \sigma} = \sum_{i=1}^n \underline{\Delta \sigma}_i$$

n being the number of iterations.

4.3.1 Implementation of the Constitutive Model in the Non-linear Analysis. As it may be concluded from the above description of the nonlinear analysis, a very important part is the calculation of the increments of the stresses on the material from the increments

of the strains. The constitutive model described in Chapter 3 will be used here to accomplish this task.

It is evident from the description of the constitutive model that the behavior of the material depends on the loading path. The state of the material is defined by the stresses $\underline{\sigma}$ (a plane state of stress is considered so that $\sigma_{33} = \tau_{23} = \tau_{31} = 0$):

$$\underline{\sigma} = [\sigma_{11}, \sigma_{22}, \tau_{12}]^T \quad (4.11)$$

and the hardening parameter k . σ_{11} , σ_{22} are the normal stresses and τ_{12} is the shear stress. The hydrostatic stress is

$$\sigma = \frac{1}{3} (\sigma_{11} + \sigma_{22}) \quad (4.12)$$

and the shearing stress intensity is given by

$$\tau = \sqrt{\frac{1}{6}} \left[(\sigma_{11} - \sigma_{22})^2 + \sigma_{11}^2 + \sigma_{22}^2 + 6 \tau_{12}^2 \right]^{1/2} \quad (4.13)$$

The assumed yield function F is

$$F(\underline{\sigma}, k) \equiv f(\sigma, \tau) - k. \quad (4.14)$$

For the state of stress $\underline{\sigma}$, $F(\underline{\sigma}, k) \leq 0$. The implementation of the constitutive model in the program can be described as follows:

First, elastic increments of stress are calculated from the increments of strain $\underline{\Delta \epsilon}$ using Eq. (4.8):

$$\underline{\Delta \sigma}^e = \begin{bmatrix} \Delta \sigma_{11}^e, \Delta \sigma_{22}^e, \Delta \tau_{12}^e \end{bmatrix}^T.$$

Second, the yield function F is calculated at the state of stress $\underline{\sigma}$. If $F(\underline{\sigma}, k) < 0$, the behavior is elastic if the increments of stress $\underline{\Delta \sigma}^e$ is not large enough for $\underline{\sigma} + \underline{\Delta \sigma}^e$ to be beyond the yield surface, i.e., if $F(\underline{\sigma} + \underline{\Delta \sigma}^e, k) \leq 0$. Thus

$$\underline{\Delta \epsilon} = \underline{\zeta}^e \underline{\Delta \sigma}^e \quad (4.15)$$

$\underline{\zeta}^e$ being the elastic compliance matrix (symmetric, 3×3) and

$$\underline{\epsilon} = \begin{bmatrix} \epsilon_{11}, \epsilon_{22}, \gamma_{12} \end{bmatrix}^T$$

$$\underline{\Delta \epsilon}^e = \begin{bmatrix} \Delta \epsilon_{11}, \Delta \epsilon_{22}, \Delta \gamma_{12} \end{bmatrix}^T$$

($\epsilon_{11}, \epsilon_{22}$ are the normal strains and γ_{12} is the shear strain.) The matrix $\underline{\zeta}^e$ is given by

$$\underline{\zeta}^e = \frac{1}{E} \begin{bmatrix} 1 & -\nu & 0 \\ -\nu & 1 & 0 \\ 0 & 0 & 2(1+\nu) \end{bmatrix}$$

(E and ν are Young's modulus and Poisson's ratio respectively.)

The normal strain and the increment of normal strain in the out-of-plane direction are given by

$$\epsilon_{33} = \frac{-\nu}{1-\nu} (\epsilon_{11} + \epsilon_{22}) \quad (4.16a)$$

$$\Delta\epsilon_{33} = \frac{-\nu}{1-\nu} (\Delta\epsilon_{11} + \Delta\epsilon_{22}) \quad (4.16b)$$

Eq. (4.15) may be rewritten as

$$\underline{\underline{\Delta\sigma}}^e = \underline{\underline{D}}^e \underline{\underline{\Delta\epsilon}} \quad (4.17)$$

where $\underline{\underline{D}}^e = [\underline{\underline{C}}^e]^{-1}$ is the elastic rigidity matrix (symmetric, 3×3).

In the case that $F(\underline{\underline{\sigma}} + \underline{\underline{\Delta\sigma}}^e, k) > 0$, the increments of stress must be divided into two parts: one to bring the state of stress to the yield surface (elastic behavior as described before) and the remainder resulting in elastoplastic behavior as described below.

If $F(\underline{\underline{\sigma}}, k) = 0$ (the state of stress is on the yield surface), the following cases are distinguished:

1) Loading:

$$\left[\frac{\partial F}{\partial \underline{\underline{\sigma}}} \right]^T \underline{\underline{\Delta\sigma}}^e > 0$$

with

$$\frac{\partial F}{\partial \underline{\sigma}} = \left[\frac{\partial F}{\partial \sigma_{11}}, \frac{\partial F}{\partial \sigma_{22}}, \frac{\partial F}{\partial \tau_{12}} \right]^T.$$

The constitutive equations are

$$\underline{\Delta \varepsilon} = (\underline{C}^e + \underline{C}^p) \underline{\Delta \sigma} \quad (4.18)$$

$$\text{where } \underline{\Delta \sigma} = [\Delta \sigma_{11}, \Delta \sigma_{22}, \Delta \tau_{12}]^T$$

are the increments of stress that correspond to $\underline{\Delta \varepsilon}$. \underline{C}^p is the two-dimensional plastic compliance matrix (3x3) and \underline{C}^e is, again, the elastic compliance matrix. In order to calculate the plastic increment of normal strain in the out-of-plane direction, $\Delta \varepsilon_{33}^p$, the necessary entries in the three-dimensional plastic compliance matrix will also be computed. Thus, with the notation

$$A_i = \frac{1}{H} \left[\frac{S_i}{2T} + \frac{1}{3} \beta \right], \quad i = 1, 2, 3 \quad (4.19a)$$

$$A_i = \frac{2}{H} \left[\frac{S_i}{2T} \right], \quad i = 4$$

$$B_i = \left[\frac{\partial f}{\partial T} \frac{S_i}{2T} + \frac{1}{3} \frac{\partial f}{\partial T} \right], \quad i = 1, 2, 3 \quad (4.19b)$$

$$B_i = 2 \left[\frac{\partial f}{\partial T} \frac{S_i}{2T} \right], \quad i = 4$$

($S_1 = \sigma_{11} - \sigma$, $S_2 = \sigma_{22} - \sigma$, $S_3 = \sigma_{33} - \sigma$, $S_4 = \tau_{12}$; H and β are the plastic shear modulus and the inelastic dilatancy factor respectively as defined in Chapter 3.) The entries of the three-dimensional matrix \underline{C}^p may be written as (see Eq. (3.19)):

$$C_{ij}^p = A_i B_j, \quad i, j = 1, 2, 3, 4. \quad (4.20)$$

This is a 4×4 matrix. Since $\Delta\sigma_{33}$ is zero, the third column may be deleted. Keeping rows 1, 2, 4 yields the two-dimensional plastic compliance matrix in Eq. (4.18). Row 3 is used in order to calculate the plastic increment of strain in the out-of-plane direction $\Delta\epsilon_{33}^p$.

Eq. (4.18) may be rewritten as

$$\underline{\Delta\sigma} = \underline{D}^{ep} \underline{\Delta\epsilon}. \quad (4.21)$$

where $\underline{D}^{ep} = [\underline{C}^e + \underline{C}^p]^{-1}$, is the elastoplastic rigidity matrix. In this study, the matrix \underline{C}^p is not necessarily symmetric and, therefore, the rigidity matrix \underline{D}^{ep} is also, in general not symmetric.

The increment of the hardening parameter k is obtained as

$$\Delta k = \left[\frac{\partial F}{\partial \underline{\sigma}} \right]^T \underline{\Delta\sigma}. \quad (4.22)$$

2) Unloading:

$$\left[\frac{\partial F}{\partial \underline{\sigma}} \right]^T \underline{\Delta\sigma}^e < 0.$$

The behavior is elastic (Eq. (4.17)).

3) Neutral loading:

$$\left[\frac{\partial F}{\partial \underline{u}} \right]^T \underline{\Delta \sigma}^e = 0.$$

Again, elastic behavior is obtained (Eq. (4.17)).

4.3.2 Calculation of Residual Forces from Residual Stresses.

After the residual stresses are calculated at each integration point, the corresponding nodal residual forces for each element may be found using the equation:

$$\underline{\Delta F}^i = \underline{K}^i \underline{\Delta U}^i.$$

Since

$$\underline{K}^i = \int_{vol} \underline{B}^T \underline{D} \underline{B} \, dv, \quad \underline{\Delta \epsilon} = \underline{B} \underline{\Delta U}^i \quad \text{and}$$

$$\underline{\Delta \sigma} = \underline{D} \underline{\Delta \epsilon},$$

$$\underline{\Delta F}^i = \int_{vol} \underline{B}^T \underline{D} \underline{B} \, dv \underline{\Delta U}^i = \int_{vol} \underline{B}^T \underline{D} \underline{B} \underline{\Delta U}^i \, dv$$

$$\underline{\Delta F}^i = \int_{vol} \underline{B}^T \underline{\Delta \sigma} \, dv \quad (4.23)$$

where $\underline{\Delta F}^i$ is the vector of nodal residual forces for element i and $\underline{\Delta \sigma}$ represents the residual stresses in the element. The integration

is carried out numerically:

$$\underline{\Delta F}^i = \sum_{\ell=1}^q w_{\ell} \underline{B}^T \underline{\Delta \sigma}_{\ell} \quad (4.24)$$

$\underline{\Delta \sigma}_{\ell}$ is the vector of residual stresses at integration point ℓ .

4.3.3 Convergence Criterion. In this study the convergence test is based on a relative error estimate calculated from the nodal displacements and increments of nodal displacements of the structure. The ratio of the square root of the sum of the squares of the increments of the nodal displacements to the square root of the sum of the squares of the nodal displacements in an iteration is obtained. If it is less than a specified tolerance then iterations are terminated. The value of the tolerance is chosen so that displacements are determined accurately and residual nodal forces are also relatively small at termination of the iterations. The tolerance value used in this analysis is 10^{-8} . After termination of the iterations, the remaining vector of residual nodal forces is added to the next load increment.

4.3.4 Failure Criteria. As discussed in Chapter 3, the hardening parameter k assumes values between 0 and 1. $k = 0$ indicates the initiation of material inelasticity and $k = 1$ means that the ultimate strength of the material is reached. In this analysis failure may occur locally and globally. If, at an integration point, ultimate strength is reached the material is assumed to fail locally at that point and the stresses are considered as residual ones. This does not necessarily mean a global failure of the specimen. It may still

carry load. However, if equilibrium cannot be satisfied after redistribution of stresses, as evidenced by failure to achieve convergence, the specimen is assumed to collapse.

CHAPTER 5

MORTAR-AGGREGATE INTERFACE MODELING

5.1 Introduction

The interface between the coarse aggregate and the mortar is, in general, the weakest link in concrete. This is most clearly seen in uniaxial compression. Under this state of stress, failure of the concrete specimen generally starts with the development of bond cracks at the interface which propagate through the mortar. Uniaxial compression tests have shown less bond cracks in high strength concrete than in normal strength concrete (see Chapter 2). However, tests of the concrete model specimens in uniaxial compression exhibit configuration of cracks parallel to the direction of the applied load and following a path along the interface.

Thus it may be seen that it is very important to include in the analysis a model to reproduce the behavior of the interface between the coarse aggregate and the mortar. In this study this is done by means of the special interface element shown in Fig. 5.1. The internal nodes 1, 3 and 5 are attached to an element that represents the aggregate while the external nodes 2, 4 and 6 are attached to an element that represents the mortar (see Fig. 4.1). The global coordinates x , y are the same for each pair of adjacent nodes and the element thickness t is set equal to a very small number.

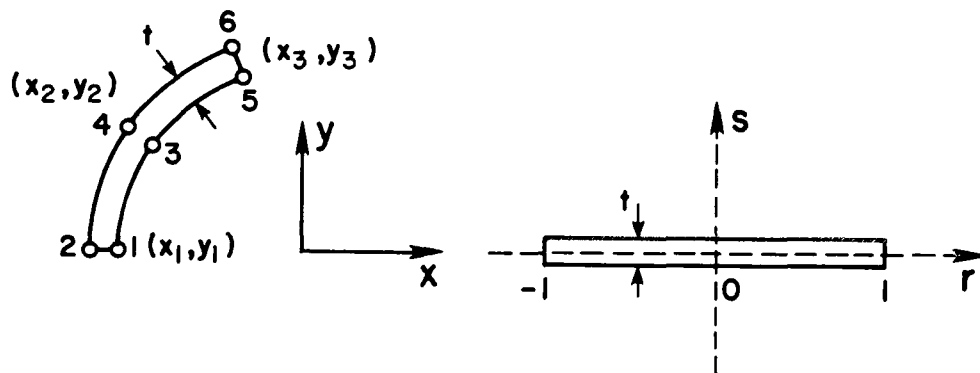


Fig. 5.1 Interface element in global and local systems of coordinates.

5.2 Derivation of the Stiffness Matrix of the Interface Element

The interface element is also an isoparametric element and the derivation of its stiffness matrix follows a procedure similar to that used in the derivation of the stiffness matrices of the other elements. The derivation can be summarized as follows:

Step 1. The displacements at any point along the edges of the element are expressed in terms of the nodal displacements:

$$u_{in}^G = N_1 u_1 + N_2 u_3 + N_3 u_5 \quad (5.1a)$$

$$v_{in}^G = N_1 v_1 + N_2 v_3 + N_3 v_5 \quad (5.1b)$$

$$u_{out}^G = N_1 u_2 + N_2 u_4 + N_3 u_6 \quad (5.1c)$$

$$v_{out}^G = N_1 v_2 + N_2 v_4 + N_3 v_6 \quad (5.1d)$$

where the subscripts *in* and *out* indicate displacements of the inside and of the outside edge of the interface element respectively and the superscript *G* identifies displacement components in the global system of coordinates *x*, *y*. The interpolation functions are

$$N_1 = \frac{1}{2} r (r - 1)$$

$$N_2 = (1 - r) (1 + r)$$

$$N_3 = \frac{1}{2} r (1 + r)$$

Eqs. (5.1) may be organized in matrix form as follows:

$$\underset{\sim}{u}^G = \underset{\sim}{N} \underset{\sim}{u}_n \quad (5.2)$$

where,

$$\underset{\sim}{u}^G = [u_{in}^G, v_{in}^G, u_{out}^G, v_{out}^G]^T$$

$$\underline{u}_n = [u_1, v_1, u_2, v_2, \dots, u_6, v_6]^T$$

$$\underline{N} = [\underline{N}^1, \underline{N}^2, \underline{N}^3]$$

with

$$\underline{N}^i = \begin{bmatrix} N_i & 0 & 0 & 0 \\ 0 & N_i & 0 & 0 \\ 0 & 0 & N_i & 0 \\ 0 & 0 & 0 & N_i \end{bmatrix}$$

Step 2. The calculated displacements are transformed to a local system of coordinates that is tangent and normal to the interface at the particular point under consideration. This is done using an appropriated rotation matrix:

$$\begin{bmatrix} u_{in}^L \\ v_{in}^L \\ u_{out}^L \\ v_{out}^L \end{bmatrix} = \begin{bmatrix} \cos \theta & \sin \theta & 0 & 0 \\ -\sin \theta & \cos \theta & 0 & 0 \\ 0 & 0 & \cos \theta & \sin \theta \\ 0 & 0 & -\sin \theta & \cos \theta \end{bmatrix} \begin{bmatrix} u_{in}^G \\ v_{in}^G \\ u_{out}^G \\ v_{out}^G \end{bmatrix}$$

or,

$$\underline{U}^L = \underline{R} \underline{U}^G \quad (5.3)$$

θ is the angle between the x axis and the tangent to the interface at the point in study. $\sin \theta$ and $\cos \theta$ can be calculated at any point on the interface as follows:

$$\cos \theta = \frac{(\partial x / \partial r)}{\Delta}$$

$$\sin \theta = \frac{(\partial y / \partial r)}{\Delta}$$

with

$$\Delta = [(\partial x / \partial r)^2 + (\partial y / \partial r)^2]^{1/2}$$

since

$$x = \sum_{i=1}^3 N_i x_i$$

$$y = \sum_{i=1}^3 N_i y_i,$$

it is seen that

$$\frac{\partial x}{\partial r} = \sum_{i=1}^3 \frac{\partial N_i}{\partial r} x_i$$

$$\frac{\partial y}{\partial r} = \sum_{i=1}^3 \frac{\partial N_i}{\partial r} y_i$$

x_i and y_i being the global coordinates of the pair of nodes i (e.g., pair 1 is the pair of nodes, 1, 2, etc.).

Step 3. With the displacements in local coordinates, the strains and stresses are found in the tangent and normal directions.

The strains are equal to the difference between corresponding displacements divided by the element thickness.

$$\begin{bmatrix} \epsilon \\ \gamma \end{bmatrix} = \begin{bmatrix} 0 & \frac{-1}{t} & 0 & \frac{1}{t} \\ \frac{-1}{t} & 0 & \frac{1}{t} & 0 \end{bmatrix} \begin{bmatrix} u_{in}^L \\ v_{in}^L \\ u_{out}^L \\ v_{out}^L \end{bmatrix}$$

or,

$$\underline{\underline{\epsilon}} = \underline{\underline{I}} \underline{\underline{U}}^L \quad (5.4)$$

ϵ and γ are the strains in the normal and in the tangent directions respectively. Having calculated the strains, the stresses can be obtained as

$$\begin{bmatrix} \sigma \\ \tau \end{bmatrix} = \begin{bmatrix} E & 0 \\ 0 & G \end{bmatrix} \begin{bmatrix} \epsilon \\ \gamma \end{bmatrix}$$

or,

$$\underline{\underline{\sigma}} = \underline{\underline{D}} \underline{\underline{\epsilon}}. \quad (5.5)$$

σ and τ are the stresses in the normal and tangent directions respectively and E and G are the extensional and the shear moduli of elasticity respectively at the point under consideration. In the present analysis large values for E and G are used in order to keep the corresponding displacements of nodes in each pair practically the same. Values of E and G cannot be arbitrarily large, if ill-conditioned calculations are to be avoided. An appropriate set of values of E , G , and t may be obtained by trial and error. In this study E and G are initially set equal to 1.0×10^6 psi at all interface points and the element thickness t is set equal to 1.0×10^{-10} in.

Step 5. The element stiffness matrix is calculated.

With eqs. (5.2), (5.3) and (5.4) a relationship between strains and nodal displacements may be derived as follows:

$$\underline{\underline{\epsilon}} = \underline{\underline{T}} \underline{\underline{R}} \underline{\underline{U}}^G = \underline{\underline{T}} \underline{\underline{R}} \underline{\underline{N}} \underline{\underline{U}}_n$$

or

$$\underline{\underline{\varepsilon}} = \underline{\underline{B}} \underline{\underline{U}}_n \quad (5.6)$$

with

$$\underline{\underline{B}} = \underline{\underline{T}} \underline{\underline{R}} \underline{\underline{N}}$$

and the element stiffness matrix is given by

$$\underline{\underline{K}} = \int_{\text{element volume}} \underline{\underline{B}}^T \underline{\underline{D}} \underline{\underline{B}} \, dv$$

Again the integration is carried out numerically using three Gaussian integration points. Thus, partitioning

$$\underline{\underline{B}} = [\underline{\underline{B}}^1, \underline{\underline{B}}^2, \underline{\underline{B}}^3]$$

$$\underline{\underline{B}}^T = [(\underline{\underline{B}}^1)^T, (\underline{\underline{B}}^2)^T, (\underline{\underline{B}}^3)^T]^T$$

with

$$\underline{\underline{B}}^i = \underline{\underline{T}} \underline{\underline{R}} \underline{\underline{N}}^i$$

yields

$$\underline{K} = \sum_{i=1}^3 w_i t \begin{bmatrix} (\underline{B}^1)^T \underline{D} \underline{B}^1 & (\underline{B}^1)^T \underline{D} \underline{B}^2 & (\underline{B}^1)^T \underline{D} \underline{B}^3 \\ (\underline{B}^2)^T \underline{D} \underline{B}^1 & (\underline{B}^2)^T \underline{D} \underline{B}^2 & (\underline{B}^2)^T \underline{D} \underline{B}^3 \\ (\underline{B}^3)^T \underline{D} \underline{B}^1 & (\underline{B}^3)^T \underline{D} \underline{B}^2 & (\underline{B}^3)^T \underline{D} \underline{B}^3 \end{bmatrix} \quad (5.7)$$

where the summation is over the number of integration points and w_i is the weight of integration point i .

5.3 Bond Strength Between the Mortar and the Coarse Aggregate

The interface may be submitted to a combination of shear and tensile normal stresses or to a combination of shear and compressive stresses. Figure 5.2 shows the bond failure envelope in the two regions. The envelope is defined by the three parameters σ_t , c and ϕ , which are respectively the bond tensile strength, the cohesion and the angle of internal friction. These parameters have been measured in bond tests between coarse aggregate and normal-strength mortar. The following range of results have been reported for this type of material (see Refs. 10, 11 and 12):

σ_t = between 200 psi and 400 psi

c = between 300 psi and 600 psi

ϕ = between 32 degrees and 39 degrees

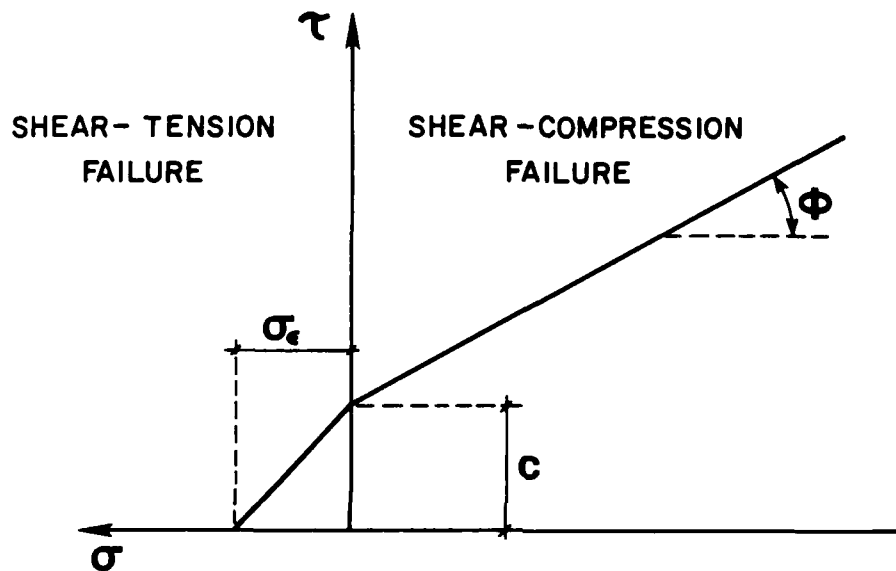


Fig. 5.2 Bond failure envelope in the $\sigma - \tau$ space.

No information is available in the literature for the bond strength between coarse aggregate and high-strength mortar; thus, in this study, different sets of parameters will be used to examine the importance of the bond strength in the performance of the concrete model.

5.4 Implementation of the Bond Properties in the Analysis

As described in Sec. 5.2, the stiffness matrix of the interface element is derived using initially large values for the extensional modulus E and the shear modulus G at all interface points. Thus, each pair of nodes has the corresponding nodal displacements practically equal and, therefore, complete attachment (stick condition) between the coarse aggregate and the mortar is achieved.

After the calculation of the nodal displacements, the strains and stresses in the tangent and normal directions at any point within the interface element can be computed. If the combination of normal and shear stresses at any point on the interface exceeds the maximum allowed by the failure envelope in Fig. 5.2, it is assumed that the bond is damaged at that point and its properties are no longer the same. The three integration points used in the derivation of the element stiffness matrix are also used here as the locations to check if the bond has failed. The procedure can be summarized as follows:

Step 1. After calculating the nodal displacements, the strains and stresses at each integration point of each interface element are found in the tangent and normal directions using Eqs. (5.6) and (5.5).

Step 2. The calculated stresses are checked to see if they exceed the maximum allowed by the failure envelope in Fig. 5.2. Here two different modes of bond failure may occur: shear-tension or shear-compression failure. If a shear-tension failure is reached at an

integration point, the values of E and G at that point are set equal to zero and the normal and the tangent stresses become residual stresses. If a shear-compression failure is achieved, only the value of the shear modulus G is set equal to zero at that integration point and only the tangent stress becomes residual stress.

Step 3. Nodal residual forces from the residual stresses (see Section 4.3.2) and the stiffness matrices of the interface elements in which the bond was damaged are obtained, now using the new values of G and E for each integration point.

Step 4. A new analysis is performed applying the residual forces and using the new stiffness matrices for the damaged interface elements. If no more integration points on the surface reach the failure envelope the analysis is complete. Otherwise, iterations are continued until no further bond damage occurs.

CHAPTER 6

ANALYTICAL RESULTS AND COMPARISON

6.1 Introduction

The presentation of the analytical results in this chapter is divided into two parts. The results shown in the first part were obtained using all the assumptions and parameters given in the preceding chapters (with the exception of the bond properties between the mortar and the aggregate which are discussed in the next section). The second part of this chapter shows some modifications introduced in the analysis in order to obtain better agreement with the experimental results.

6.2 Estimation of the Bond Properties of the Interface

As shown in Section 5.3, the bond properties of the interface can be defined by three parameters, σ_t , c and ϕ , which are, respectively, the bond tensile strength, the cohesion and the angle of internal friction. Since there appears to be no quantitative information on the properties of the bond between high-strength mortar and aggregates, the values used in this analysis were estimated by calibration with experimental results.

Figure 6.1 shows a comparison between analytical and experimental results using several different sets of bond parameters in the case of uniaxial compression. Note the slope discontinuity in

the analytical stress-strain curves corresponding to $\sigma_t = 300$ psi, $c = 500$ psi, and $\sigma_t = 1000$ psi, $c = 1000$ psi, due to failure in the interface elements. The value of the tensile bond strength, σ_t , was assumed to be equal to the tensile strength of the mortar (about 1000 psi) and the cohesion value was then adjusted in order to get the same level of strength of the experimental results. A value of 2000 psi was then assigned to the cohesion and the angle of internal friction was kept equal to 35 degrees. These values were used in all other load cases.

A map of bond damage is shown in Fig. 6.2 for the case of uniaxial compression with normal-strength concrete bond properties. A dashed line means that a shear-compression failure has occurred at the nearby integration point of the interface element and a continuous line means that a shear-tension failure has occurred in that region. This stage of loading corresponds to the points of slope discontinuity shown in the stress-strain curves in Fig. 6.1.

6.3 Analysis Prediction of the Concrete Model Behavior

The concrete model behavior, as predicted by the finite element analysis, is presented in this section. The elastic and plastic material properties used in the analysis were obtained from uniaxial compressive tests on cylindrical specimens as described in the previous chapters.

Four different load cases are studied using the same type of mortar and coarse aggregate: uniaxial compression ($\sigma_2/\sigma_1 = 0.0$),

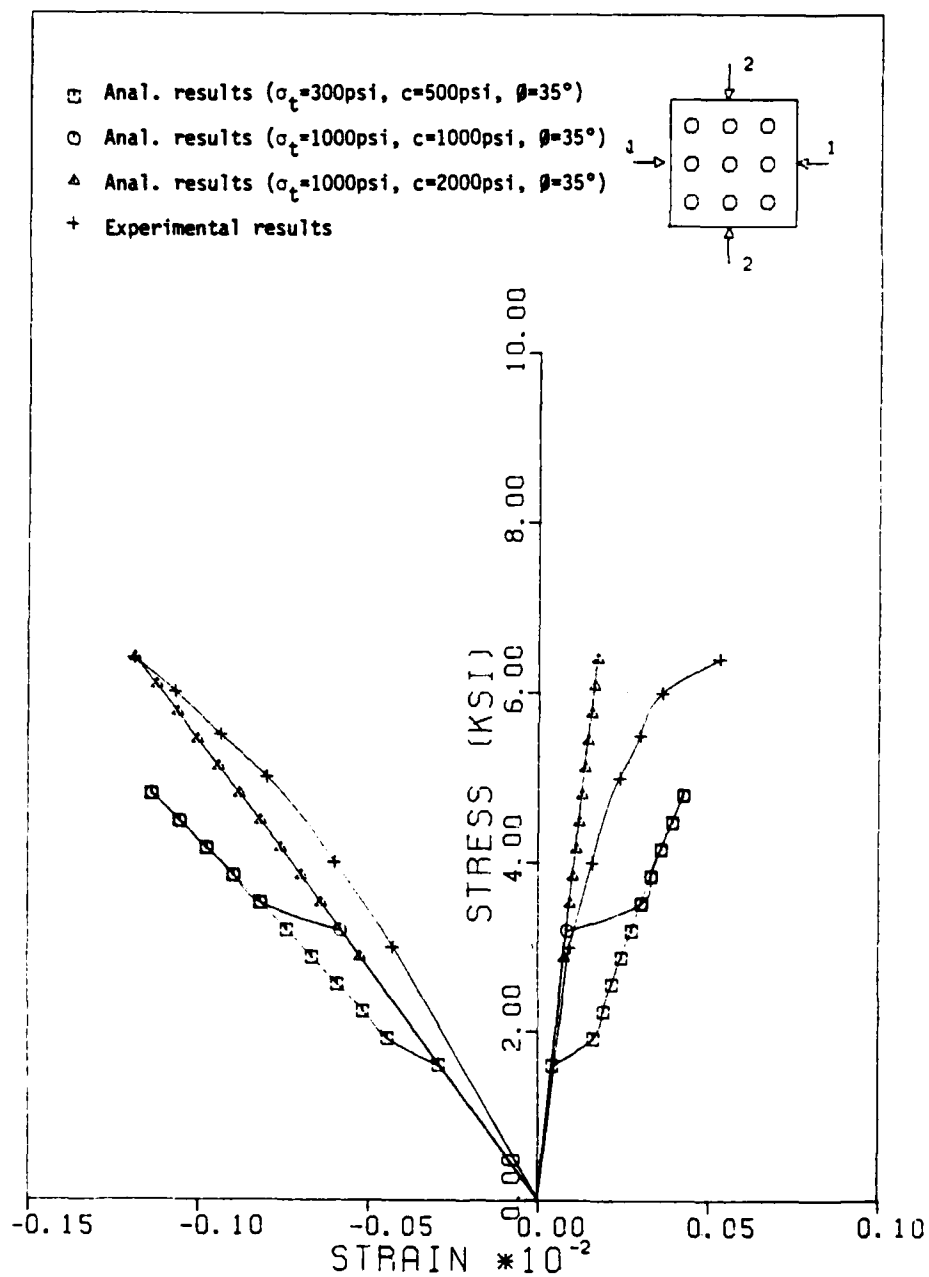


Fig. 6.1 Comparison between analytical and experimental results using different bond properties for the interface ($\sigma_2/\sigma_1 = 0.0$)

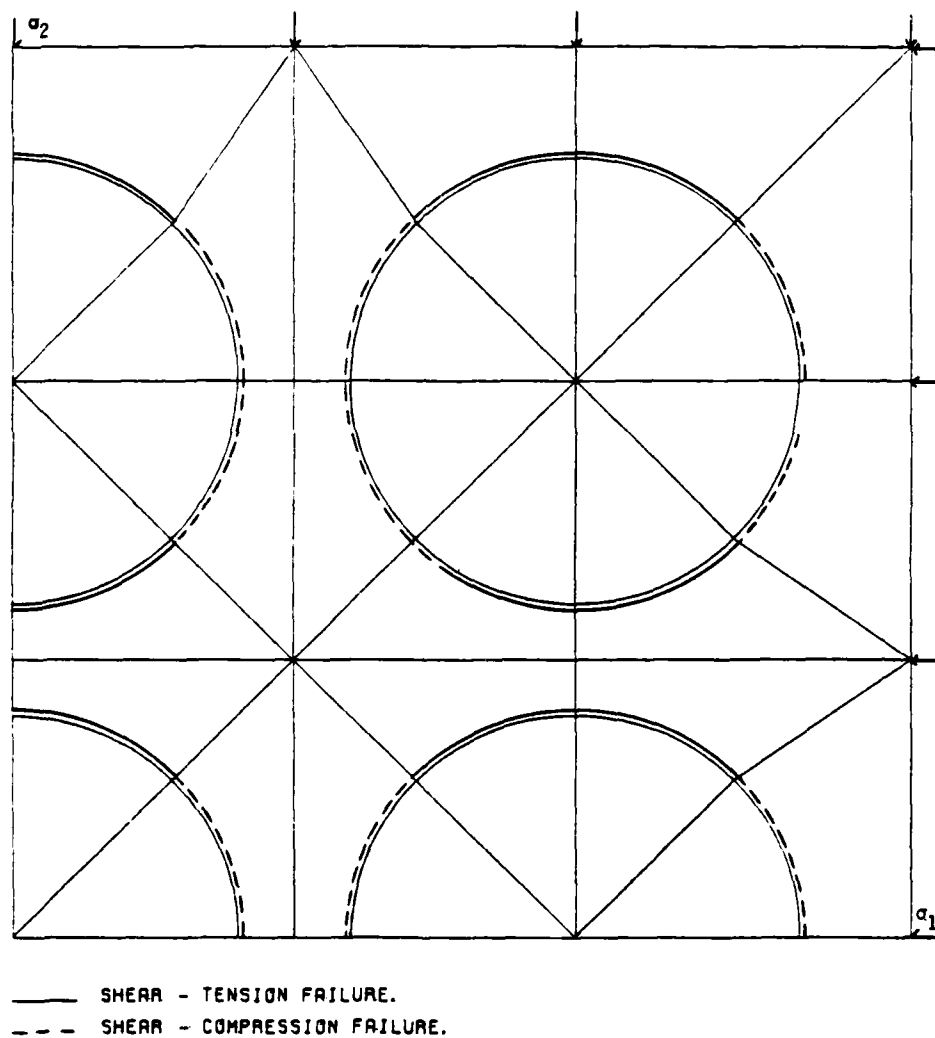


Fig. 6.2 Map of bond damage for the case of normal-strength concrete bond properties ($\sigma_2/\sigma_1 = 0.0$, $\sigma_1 = 0.40\sigma_u$)

equal biaxial compression ($\sigma_2/\sigma_1 = 1.0$), and two other biaxial compression cases ($\sigma_2/\sigma_1 = 0.50$ and $\sigma_2/\sigma_1 = 0.20$). The load is applied on the specimen in such a way that all the edge nodes have the same displacement in the direction of the applied load and it is assumed that there is no edge restraint in the direction perpendicular to the direction of the applied load.

6.3.1 Elastic Distribution of Stresses. A graphical representation of the principal stresses at the integration points for the four load cases is shown in Figs. 6.3 through 6.10. Each stress is represented by an arrow. The direction of the arrow coincides with the direction of the principal stress and the arrow length is proportional to the magnitude of the principal stress. A compressive principal stress is represented by an arrow pointing towards the corresponding integration point whereas a tensile principal stress is represented by an arrow pointing in the opposite direction. Two figures (with different scales) are used to represent the two principal stresses for each load case. The first figure contains the smaller (in absolute value) principal stress and the second figure contains the larger one. The externally applied stress, σ_1 , is equal to 1,000 psi. The absolute value of the stresses at the integration points without arrows in Fig. 6.3 is less than 38 psi.

Note that tensile stresses have occurred only in the case of uniaxial compression. With the exception of the case of equal biaxial compression ($\sigma_2/\sigma_1 = 1.0$), a slight concentration of stresses may be observed in the regions between two circles of aggregate and the

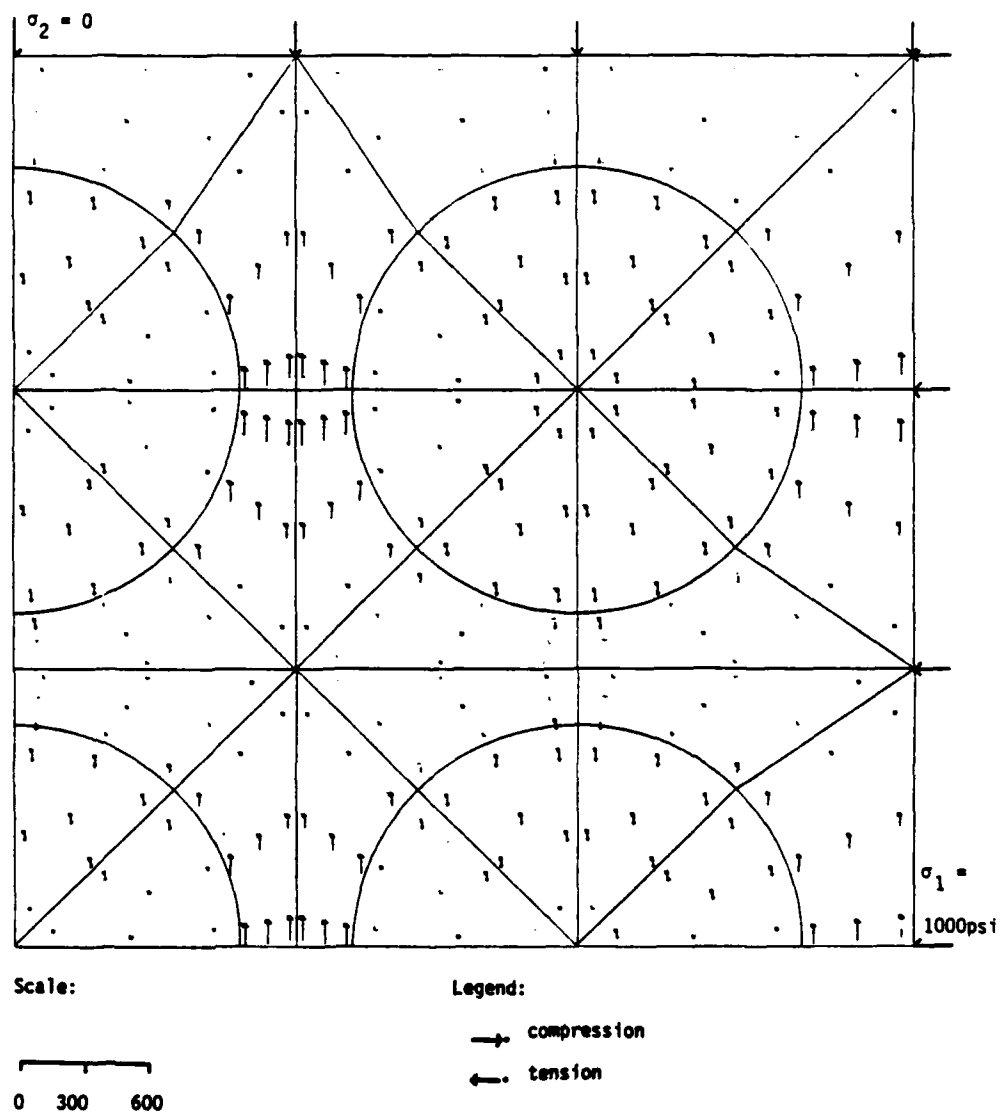


Fig. 6.3 Graphical representation of the smaller principal stress at the integration points ($\sigma_2/\sigma_1 = 0.0$).

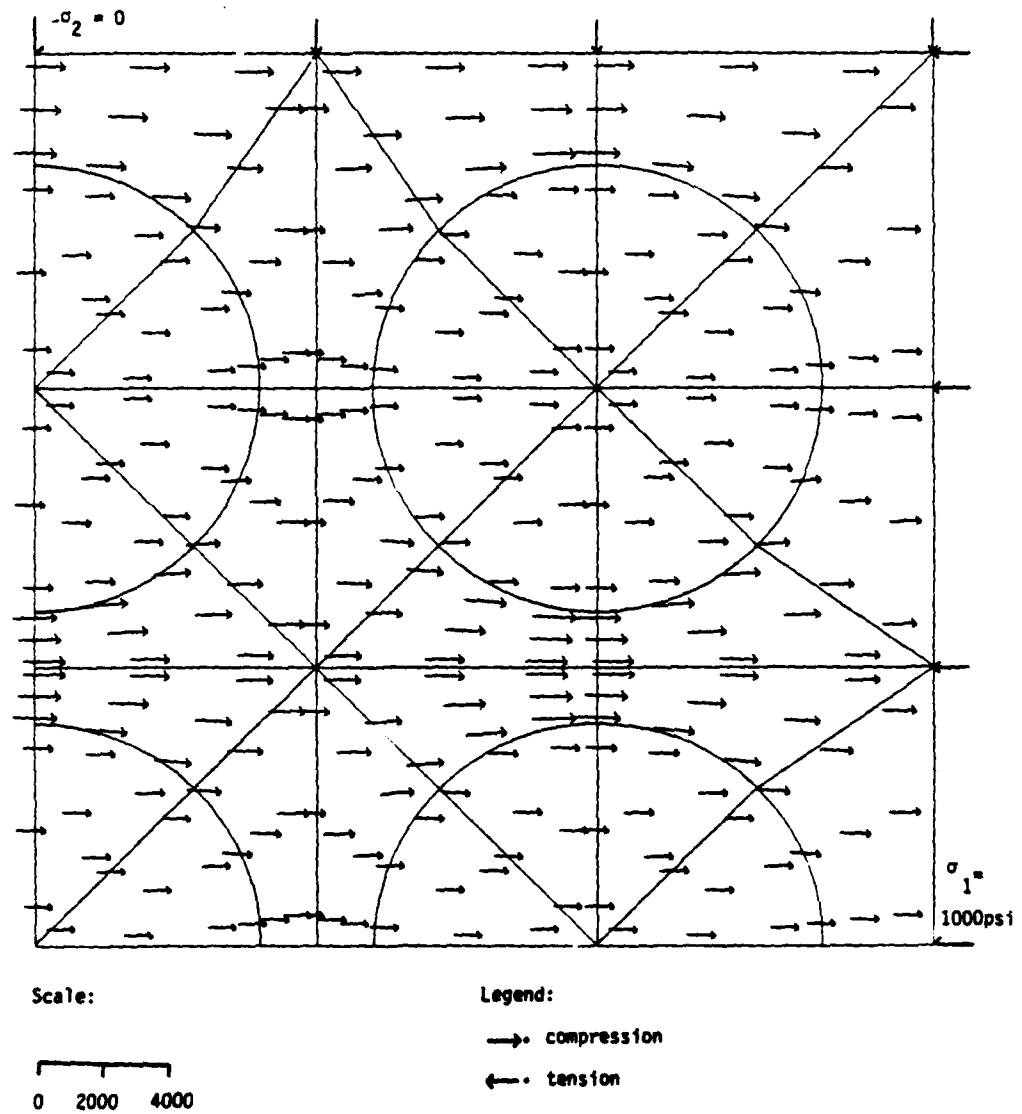


Fig. 6.4 Graphical representation of the larger principal stress at the integration points ($\sigma_2/\sigma_1 = 0.0$).

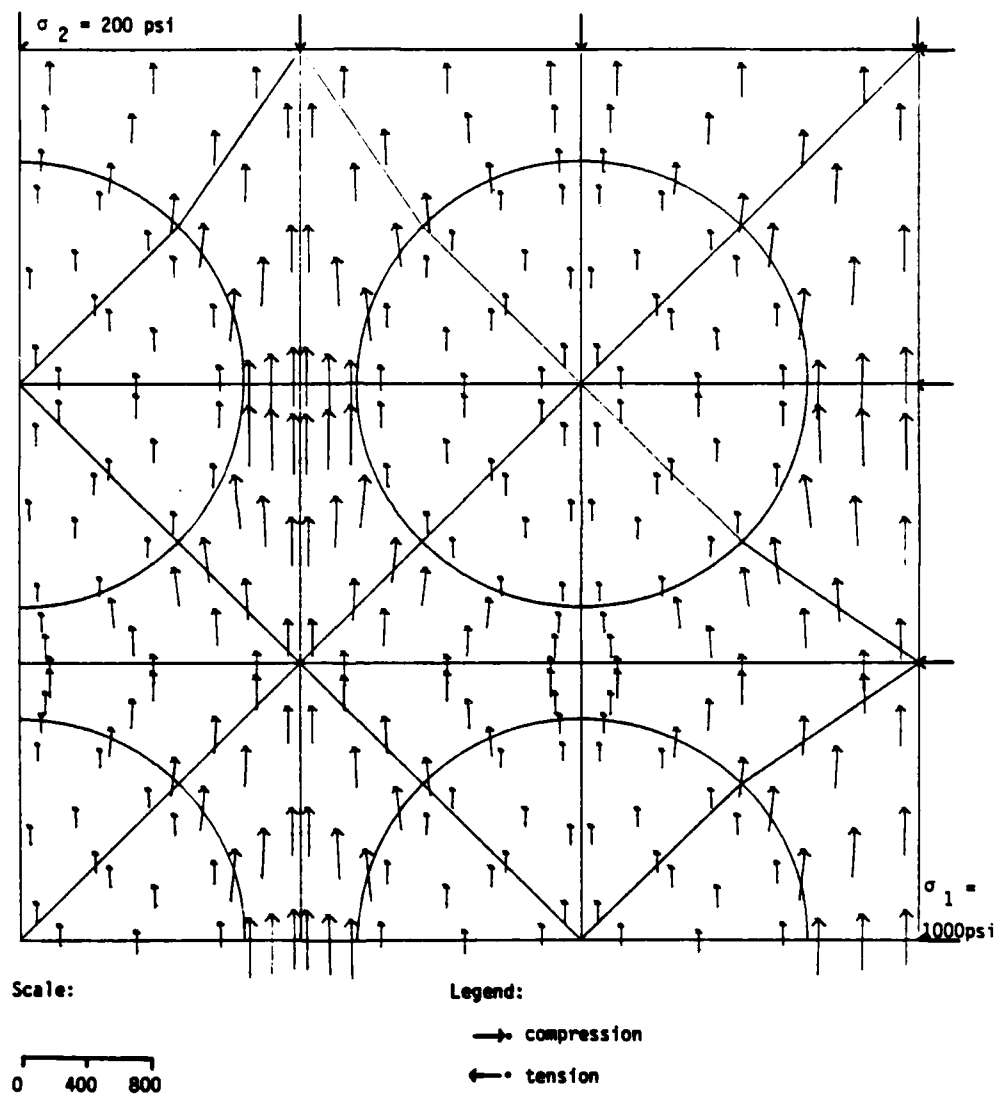
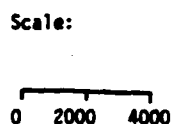


Fig. 6.5 Graphical representation of the smaller principal stress at the integration points ($\sigma_2/\sigma_1 = 0.20$).



Legend:

- compression
- ← tension

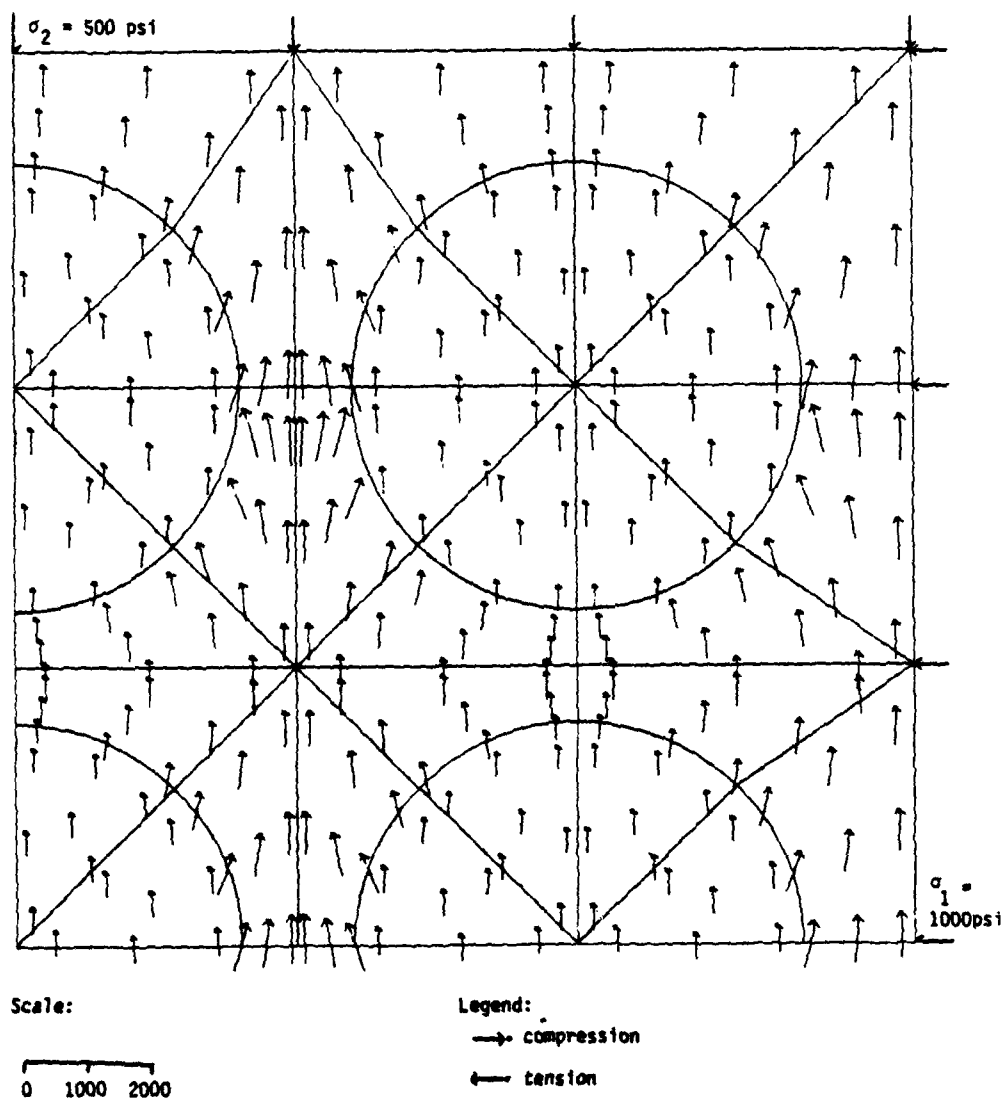


Fig. 6.7 Graphical representation of the smaller principal stress at the integration points ($\sigma_2/\sigma_1 = 0.50$).

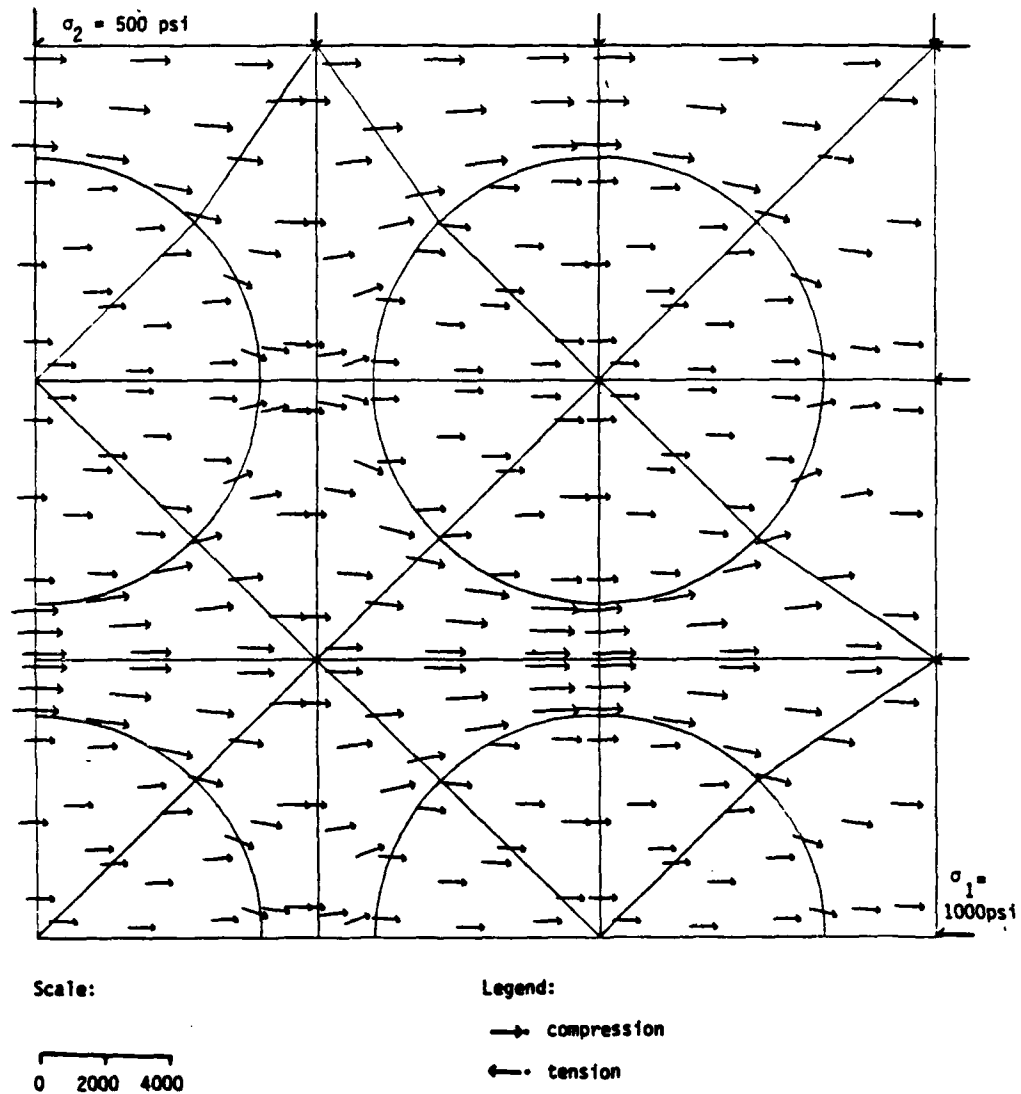


Fig. 6.8 Graphical representation of the larger principal stress at the integration points ($\sigma_2/\sigma_1 = 0.50$).

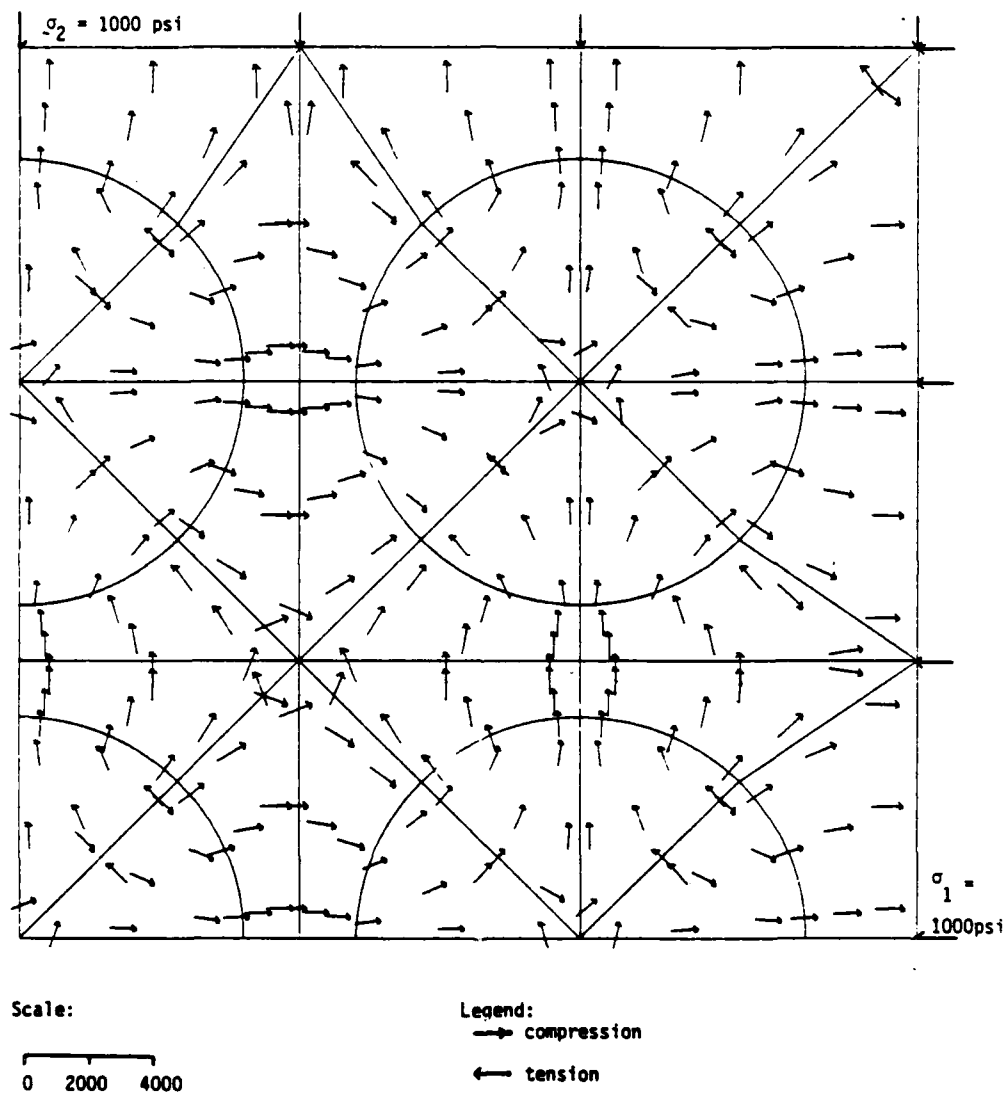


Fig. 6.9 Graphical representation of the smaller principal stress at the integration points ($\sigma_2/\sigma_1 = 1.0$).

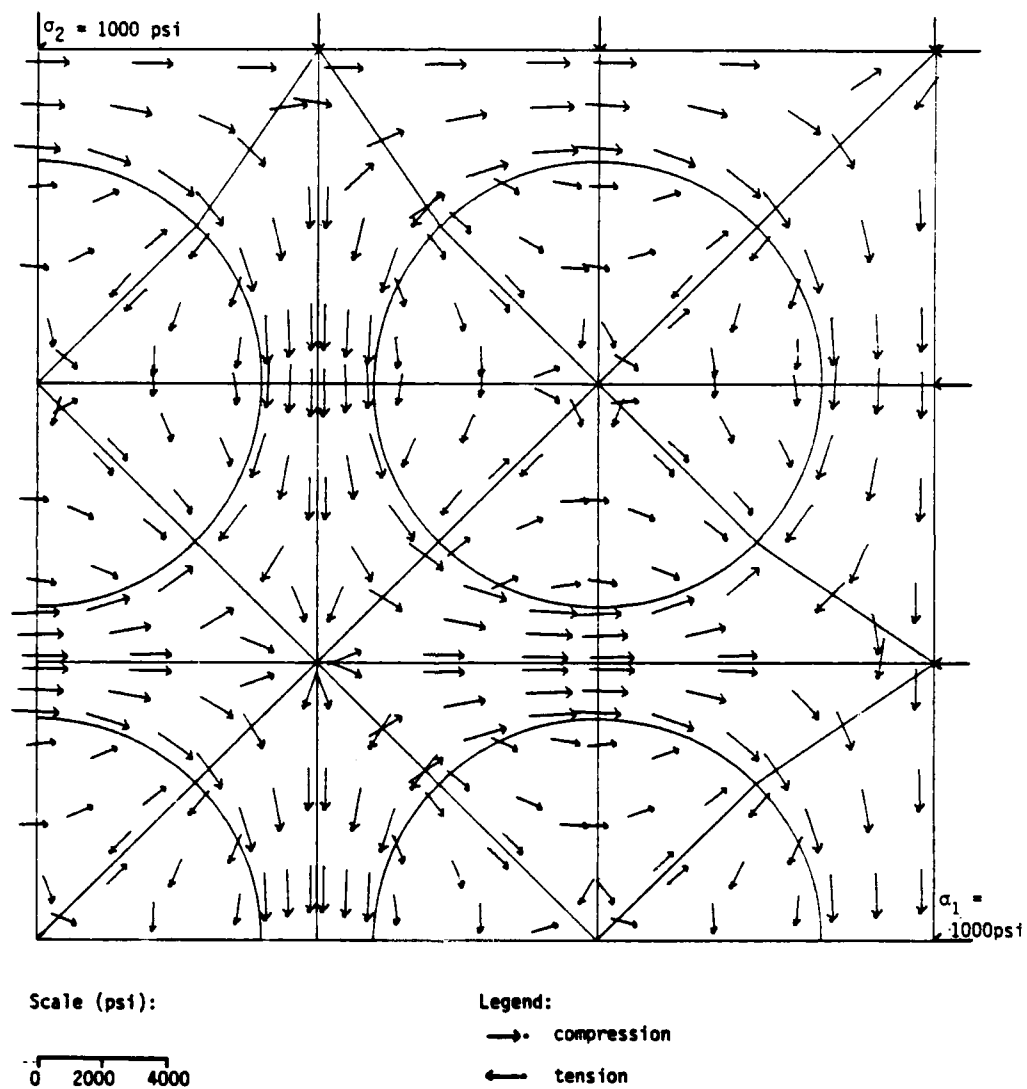
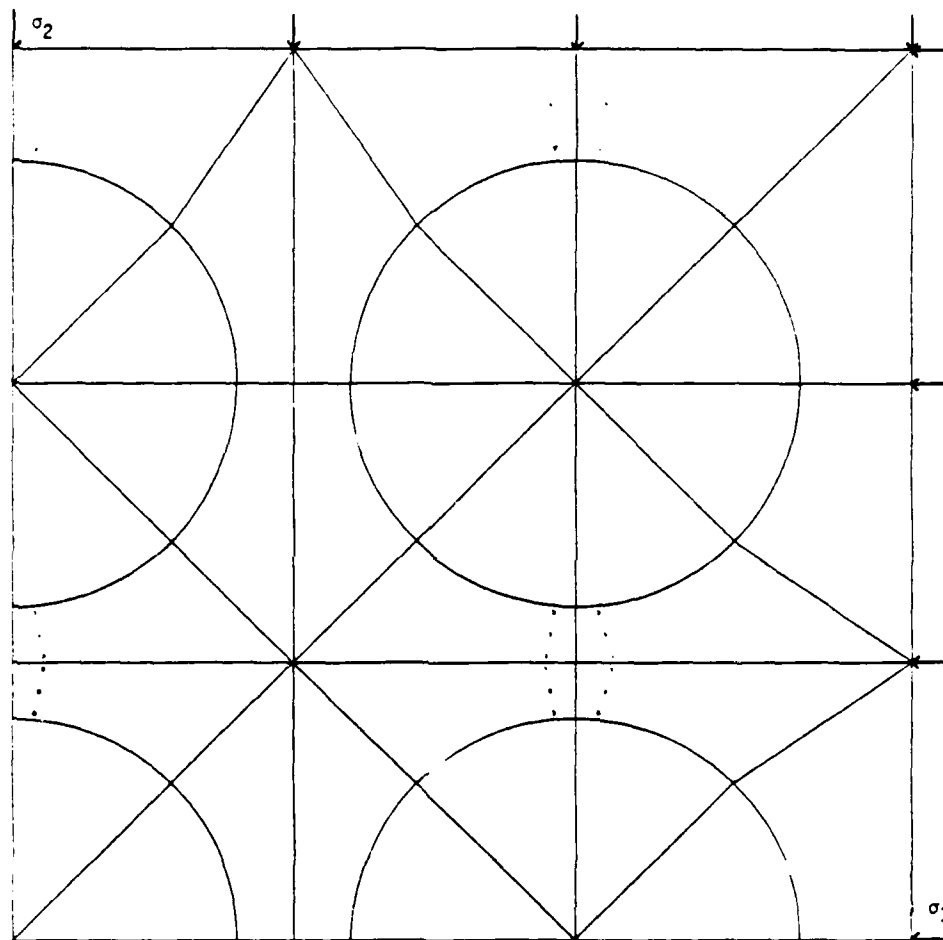


Fig. 6.10 Graphical representation of the larger principal stress at the integration points ($\sigma_2/\sigma_1 = 1.0$).

directions of the principal stresses are almost coincident with the directions of the applied loads. The equal biaxial loading case shows a more uniform distribution of stress in magnitude. In this case the directions of the principal stresses are approximately normal and tangential to the interface which means that, practically, the interface is subjected to no shear stresses.

6.3.2 Evolution of the Damage in the Concrete Model During Loading. As described in Chapter 3, the hardening parameter k was chosen to vary between 0 and 1. These values correspond, respectively, to the initiation of inelasticity and ultimate strength of the material. Thus, the magnitude of k may be used as an indicator of the proximity to failure or the degree of damage at a point in the specimen. Figures 6.11 through 6.22 show a representation of the magnitude of k at the mortar elements integration points for the four load cases and at different load stages. A circle of radius proportional to the value of k is used in the representation. For the values of k less than 0.125 the circles are not shown.

With the exception of the equal biaxial load case ($\sigma_2/\sigma_1 = 1.0$), it may be observed that the inelasticity of the material starts and develops with more intensity in the regions between two circles of aggregate in the direction perpendicular to σ_1 . Note that in the case of uniaxial compression no integration point reaches failure at ultimate strength of the specimen. This agrees with the fact that the bond strength is the most important factor influencing the ultimate strength of the specimen in this load case. The case of



- O $k = 1.0$
 • $k = 0.125$

Fig. 6.11 Degree of damage in the specimen at 65 percent of the analytical ultimate strength ($\sigma_2/\sigma_1 = 0.0$).

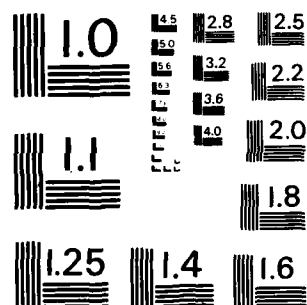
UNCLASSIFIED

AFOSR-IR 83-1341 AFOSR-81-0202

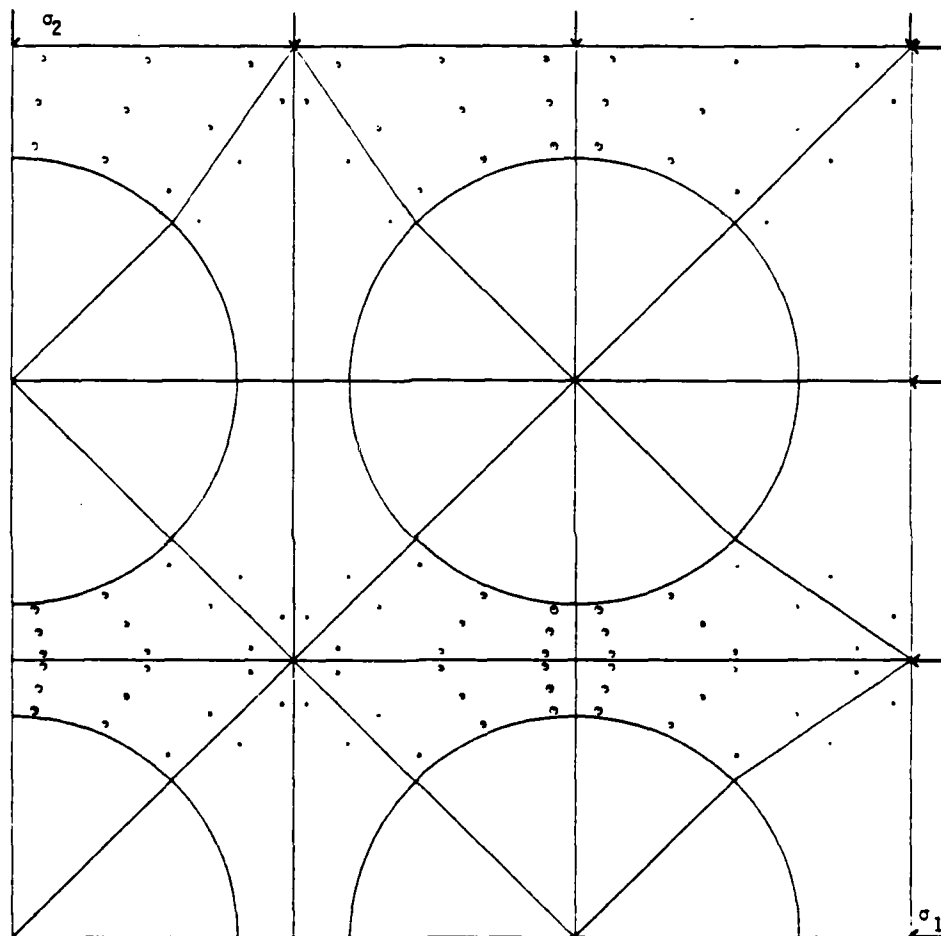
F/G 13/3

NE

END
DATE
FILMED
2 84
DTU



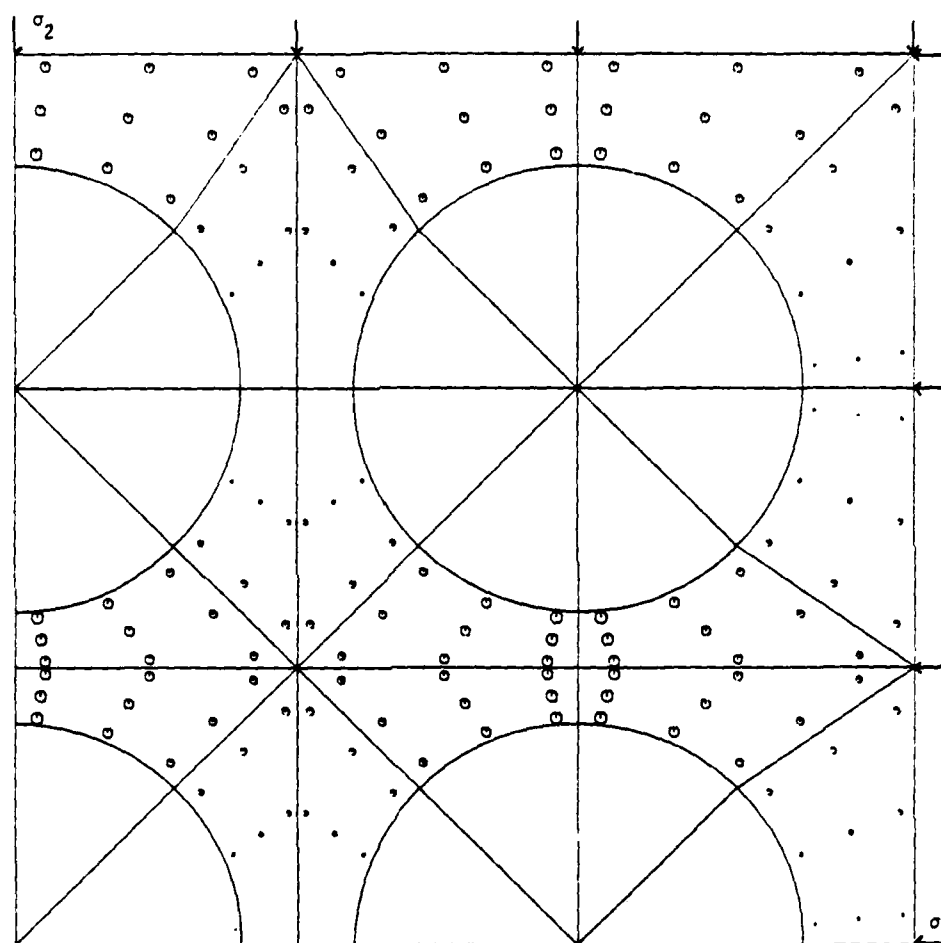
MICROCOPY RESOLUTION TEST CHART
NATIONAL BUREAU OF STANDARDS-1963-A



□ $k = 1.0$

• $k = 0.125$

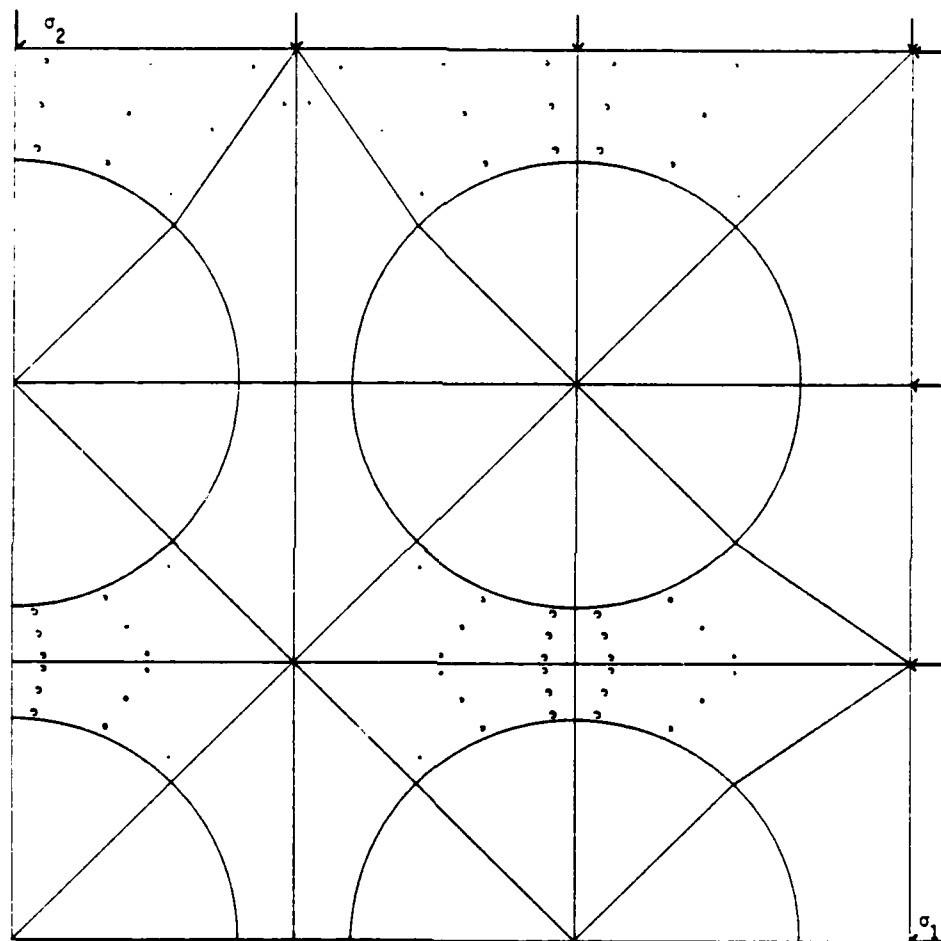
Fig. 6.12 Degree of damage in the specimen at 80 percent of the analytical ultimate strength ($\sigma_2/\sigma_1 = 0.0$).



○ $k = 1.0$

· $k = 0.125$

Fig. 6.13 Degree of damage in the specimen at the analytical ultimate strength ($\sigma_2/\sigma_1 = 0.0$).



○ $k = 1.0$

• $k = 0.125$

Fig. 6.14 Degree of damage in the specimen at 57 percent of the analytical ultimate strength ($\sigma_2/\sigma_1 = 0.20$).

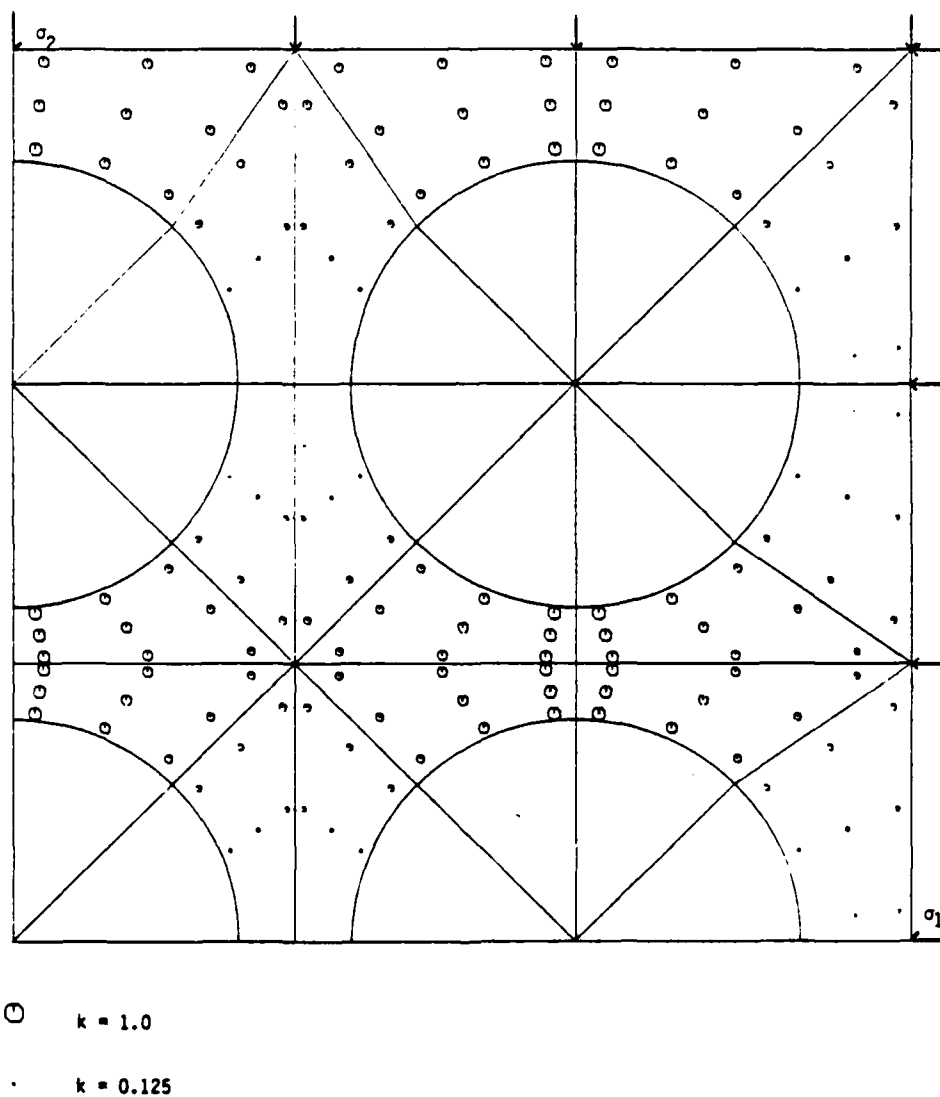


Fig. 6.15 Degree of damage in the specimen at 78 percent of the analytical ultimate strength ($\sigma_2/\sigma_1 = 0.20$).

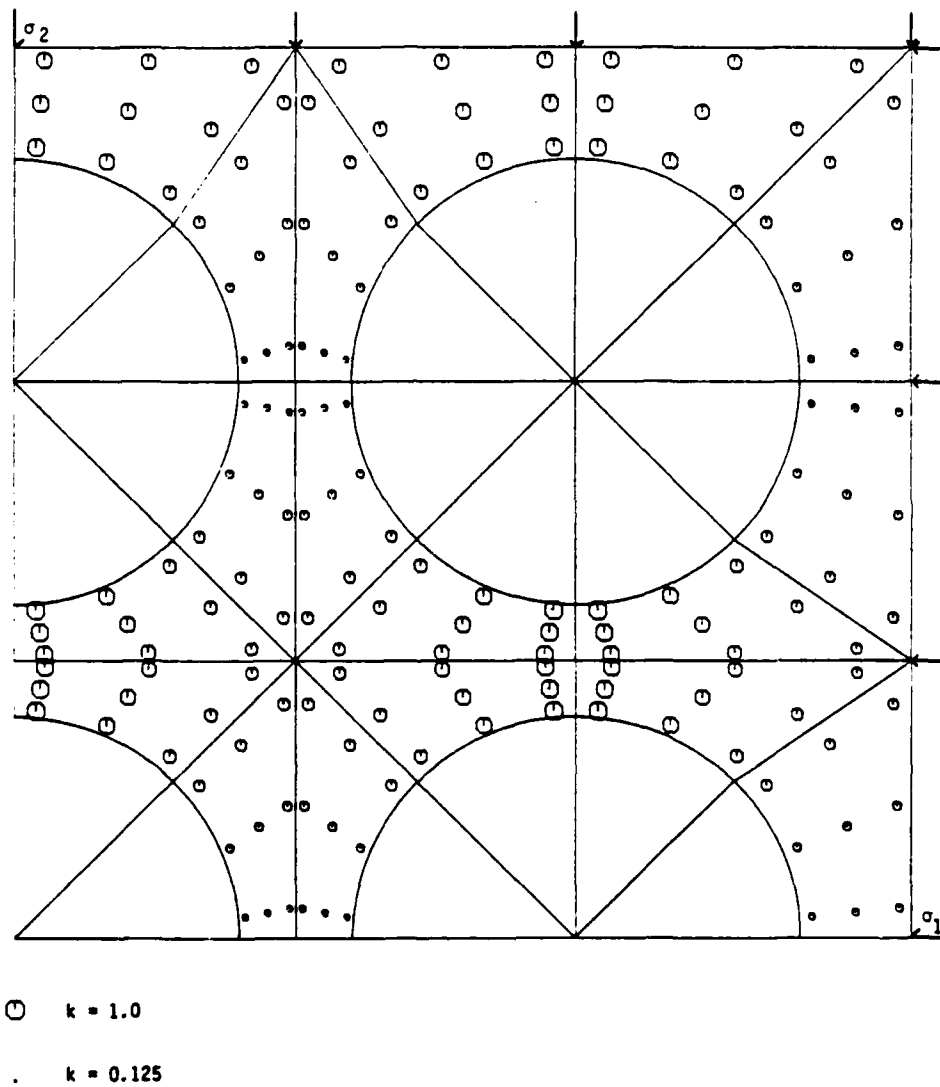
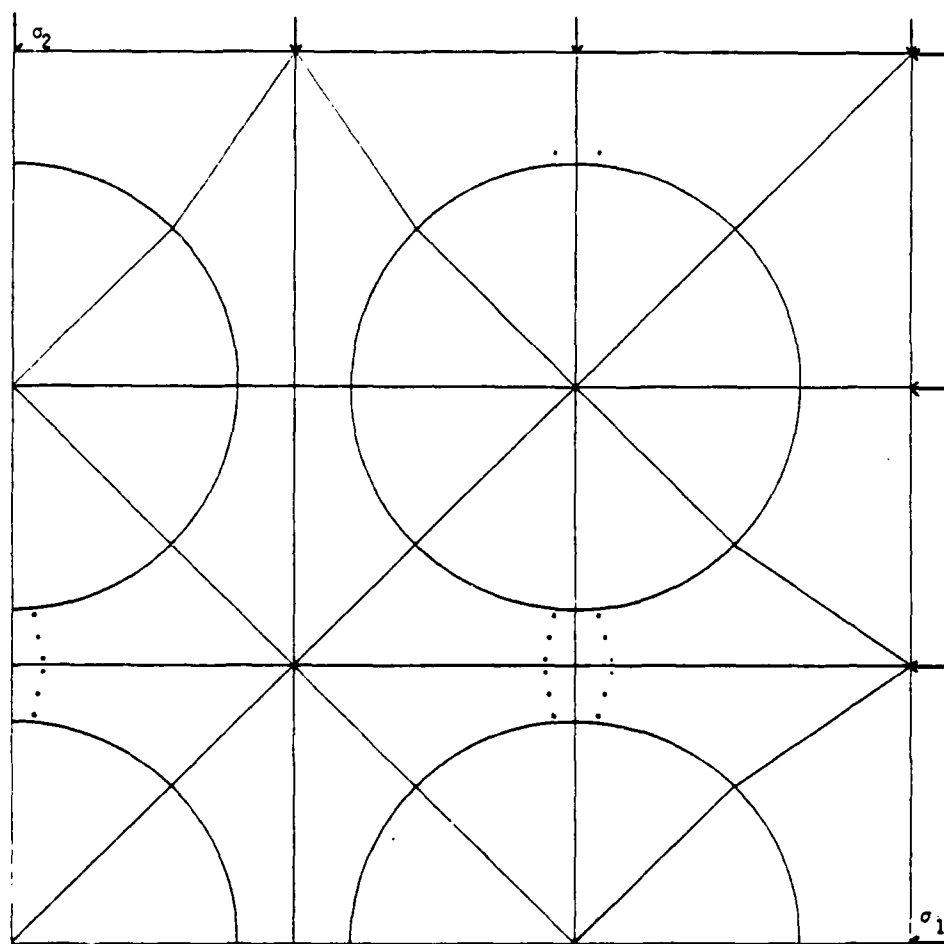


Fig. 6.16 Degree of damage in the specimen at the analytical ultimate strength ($\sigma_2/\sigma_1 = 0.20$).



⊙ $k = 1.0$

• $k = 0.125$

Fig. 6.17 Degree of damage in the specimen at 48 percent of the analytical ultimate strength ($\sigma_2/\sigma_1 = 0.50$).

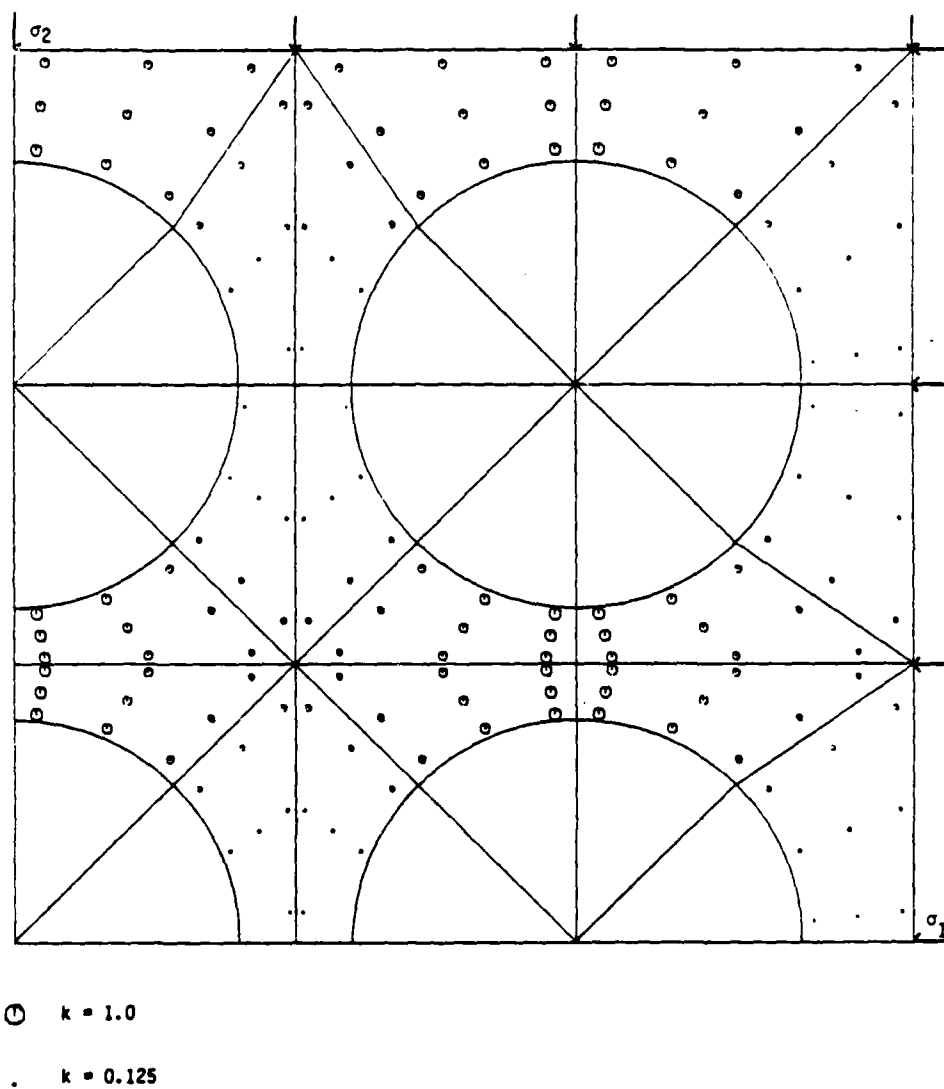


Fig. 6.18 Degree of damage in the specimen at 74 percent of the analytical ultimate strength ($\sigma_2/\sigma_1 = 0.50$).

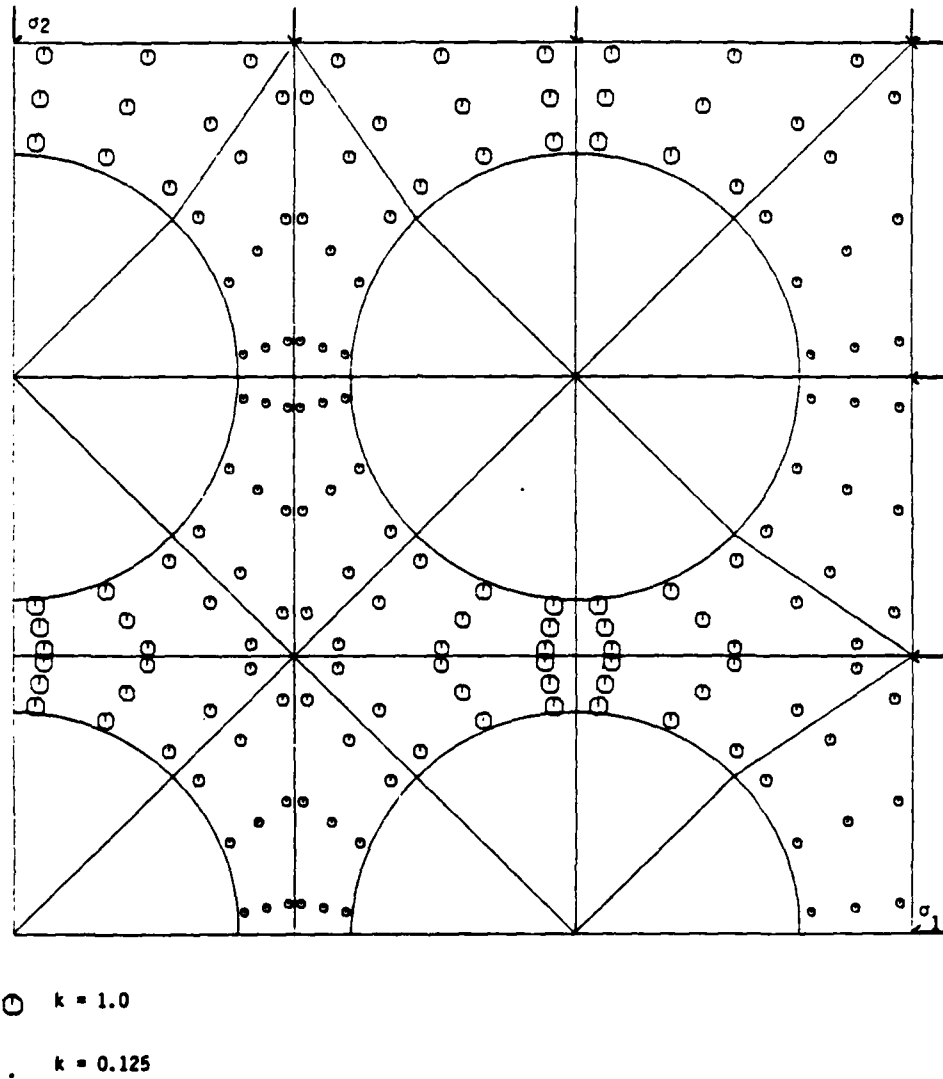


Fig. 6.19 Degree of damage in the specimen at the analytical ultimate strength ($\sigma_2/\sigma_1 = 0.50$).

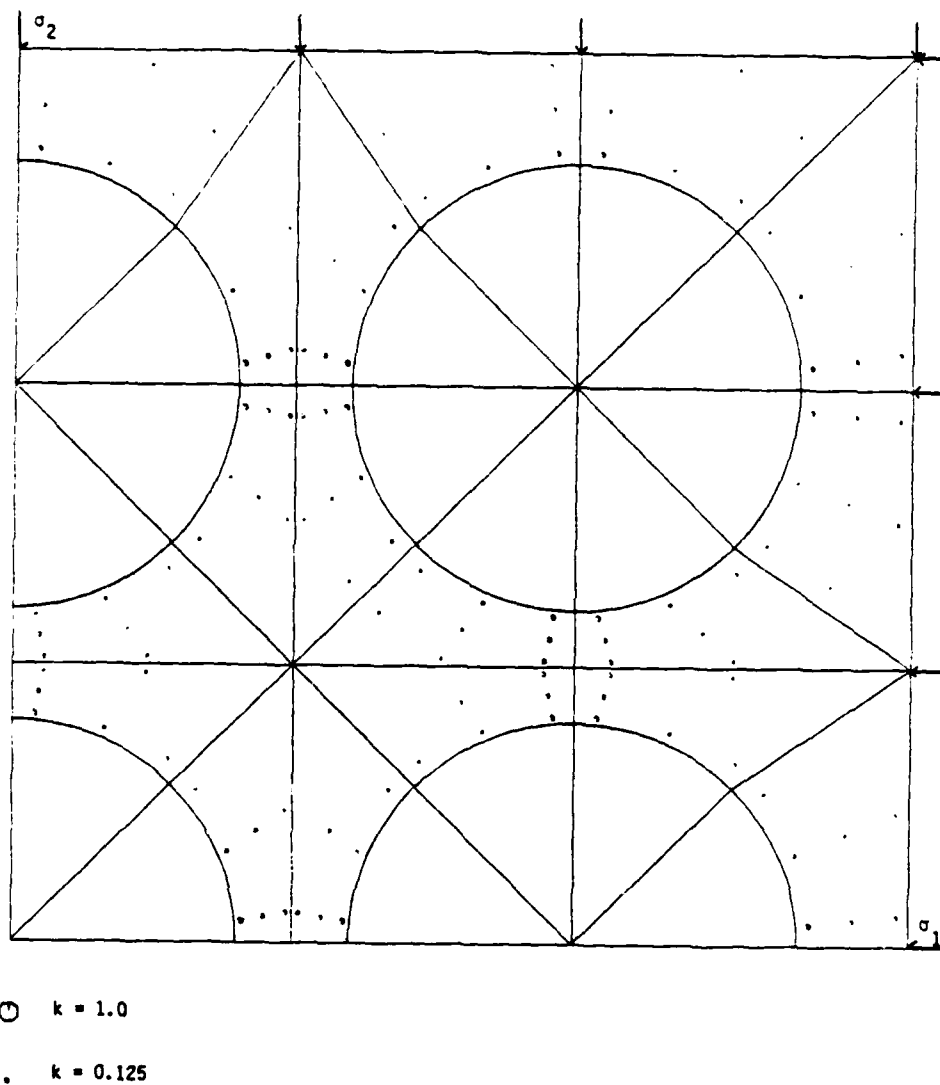
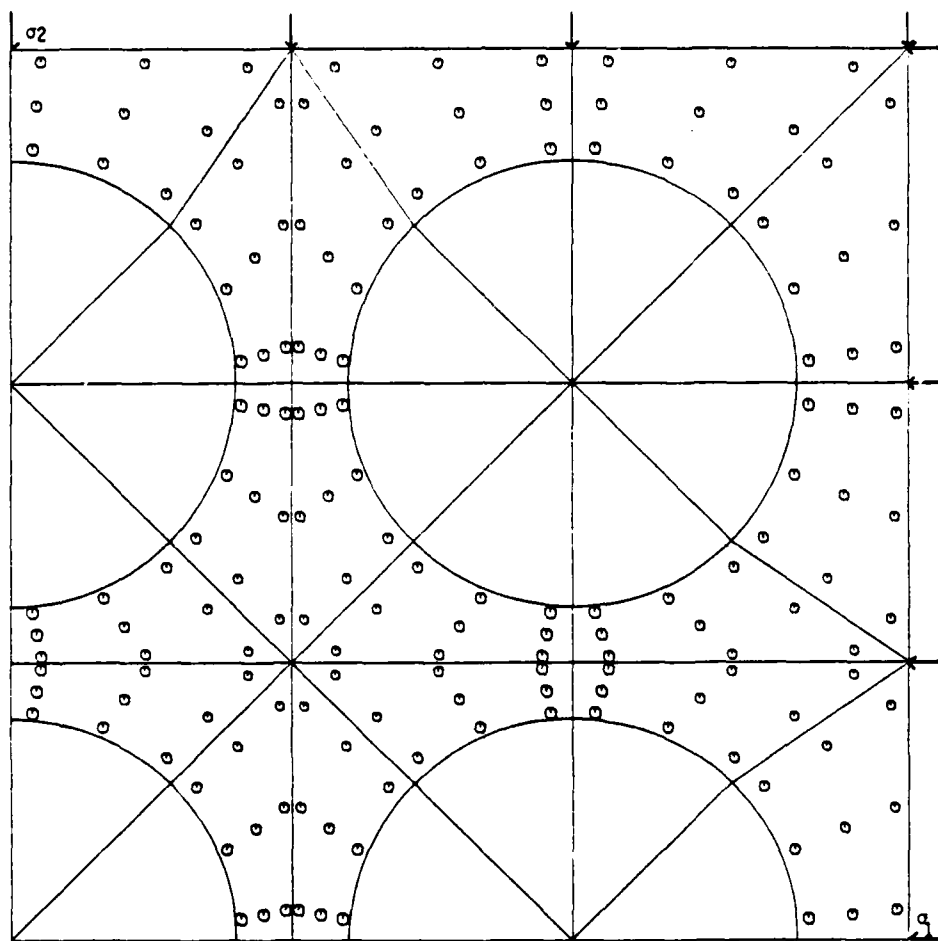


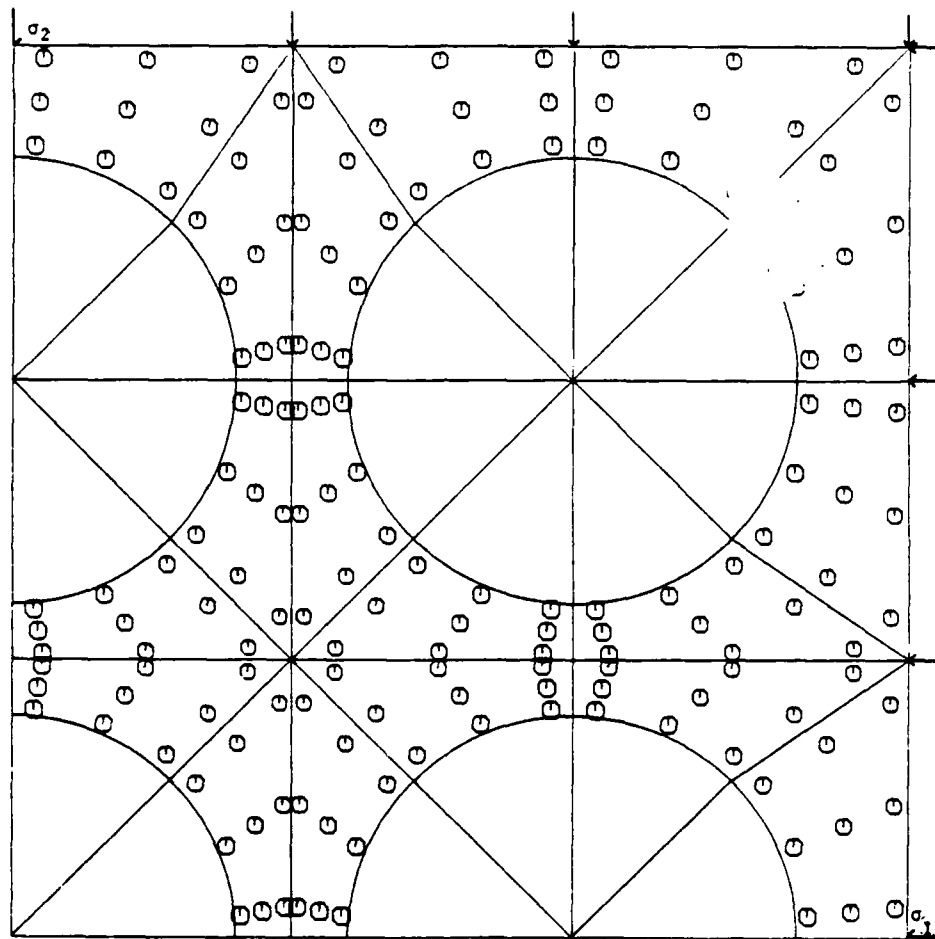
Fig. 6.20 Degree of damage in the specimen at 52 percent of the analytical ultimate strength ($\sigma_2/\sigma_1 = 1.0$).



○ $k = 1.0$

• $k = 0.125$

Fig. 6.21 Degree of damage in the specimen at 84 percent of the analytical ultimate strength ($\sigma_2/\sigma_1 = 1.0$).



○ $k = 1.0$

• $k = 0.125$

Fig. 6.22 Degree of damage in the specimen at the analytical ultimate strength ($\sigma_2/\sigma_1 = 1.0$).

equal biaxial compression shows a more uniform distribution of plasticity throughout the specimen.

6.3.3 Comparison between Analytical and Experimental Results.

Figures 6.23 through 6.26 show the stress-strain curves for the four load cases obtained from experiments and the analysis. The average strains in the directions 1 and 2 were obtained by dividing the displacements of nodes 10 and 77 respectively (Fig. 4.1) by the distance from these nodes to node 1 (1.875 in.). Nodes 10 and 77 correspond to the points at which average strains were obtained in the experiments.

For all the load cases, the analytical results show less stiffness than the experimental ones even at low levels of load for which the specimen is still elastic.

Bond failure for the load cases $\sigma_2/\sigma_1 = 0.0$ and $\sigma_2/\sigma_1 = 0.20$ was observed in the analysis just prior to failure of the specimen. For the load cases $\sigma_2/\sigma_1 = 0.50$ and $\sigma_2/\sigma_1 = 1.0$ the interface remained undamaged up to failure of the specimen and the analytical results showed higher ultimate strength and ultimate strains than the experimental ones. The analytical results in Figs. 6.23 to 6.26 were obtained using the plastic shear modulus H as a function of the hardening parameter k and the hydrostatic stress σ (see Table 3.3).

Figures 6.27 through 6.30 show the analytical results obtained with the plastic shear modulus H as a function of the hardening parameter k only. With this change in the plastic properties of the mortar, the load case $\sigma_2/\sigma_1 = 0.20$ did not show a bond failure at the

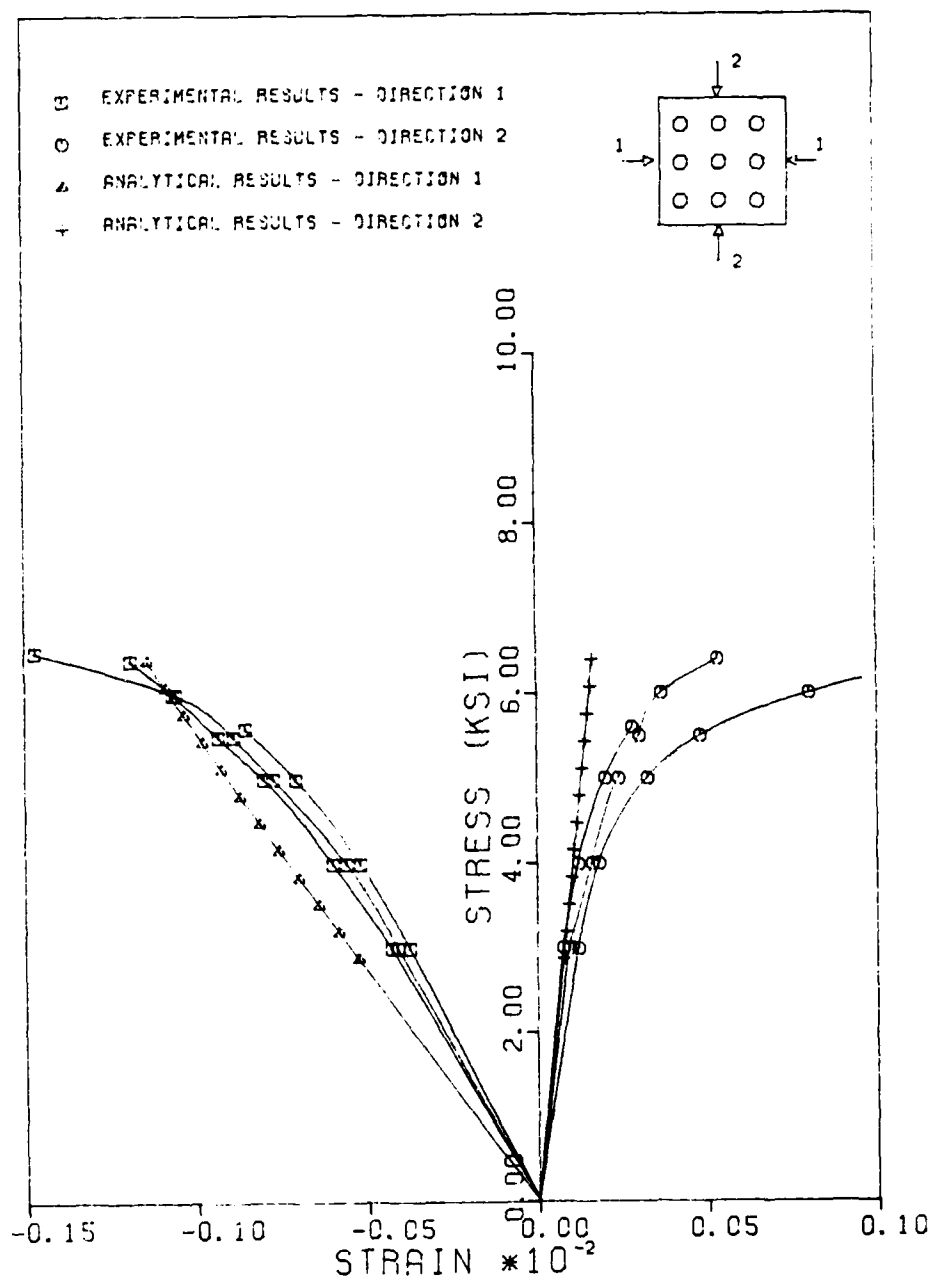


Fig. 6.23 Comparison between analytical and experimental results ($\sigma_1/\sigma_2 = 0.0$; $H = f(\sigma, k)$).

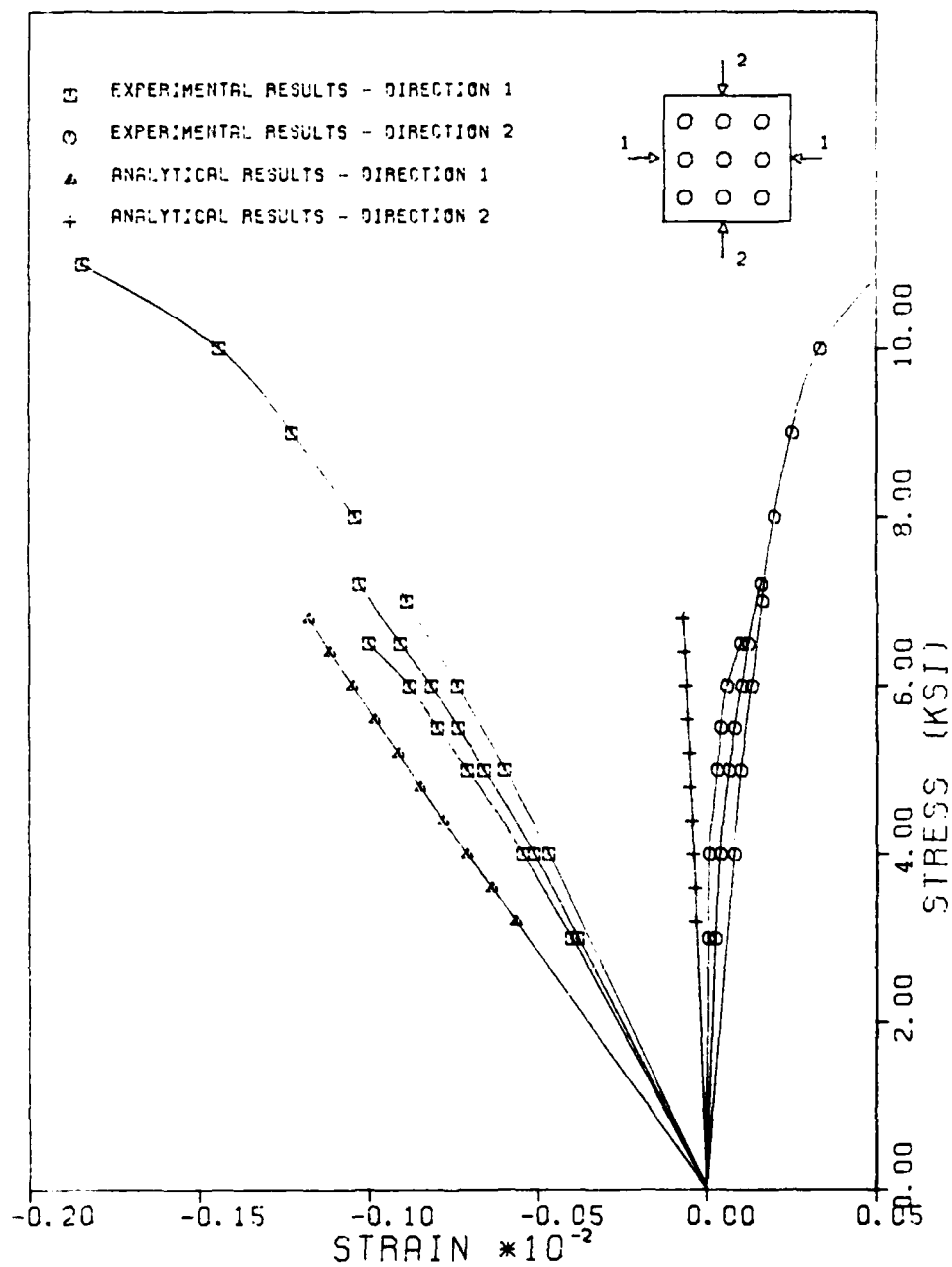


Fig. 6.24 Comparison between analytical and experimental results ($\sigma_1/\sigma_2 = 0.20$; $H = f(\sigma, k)$).

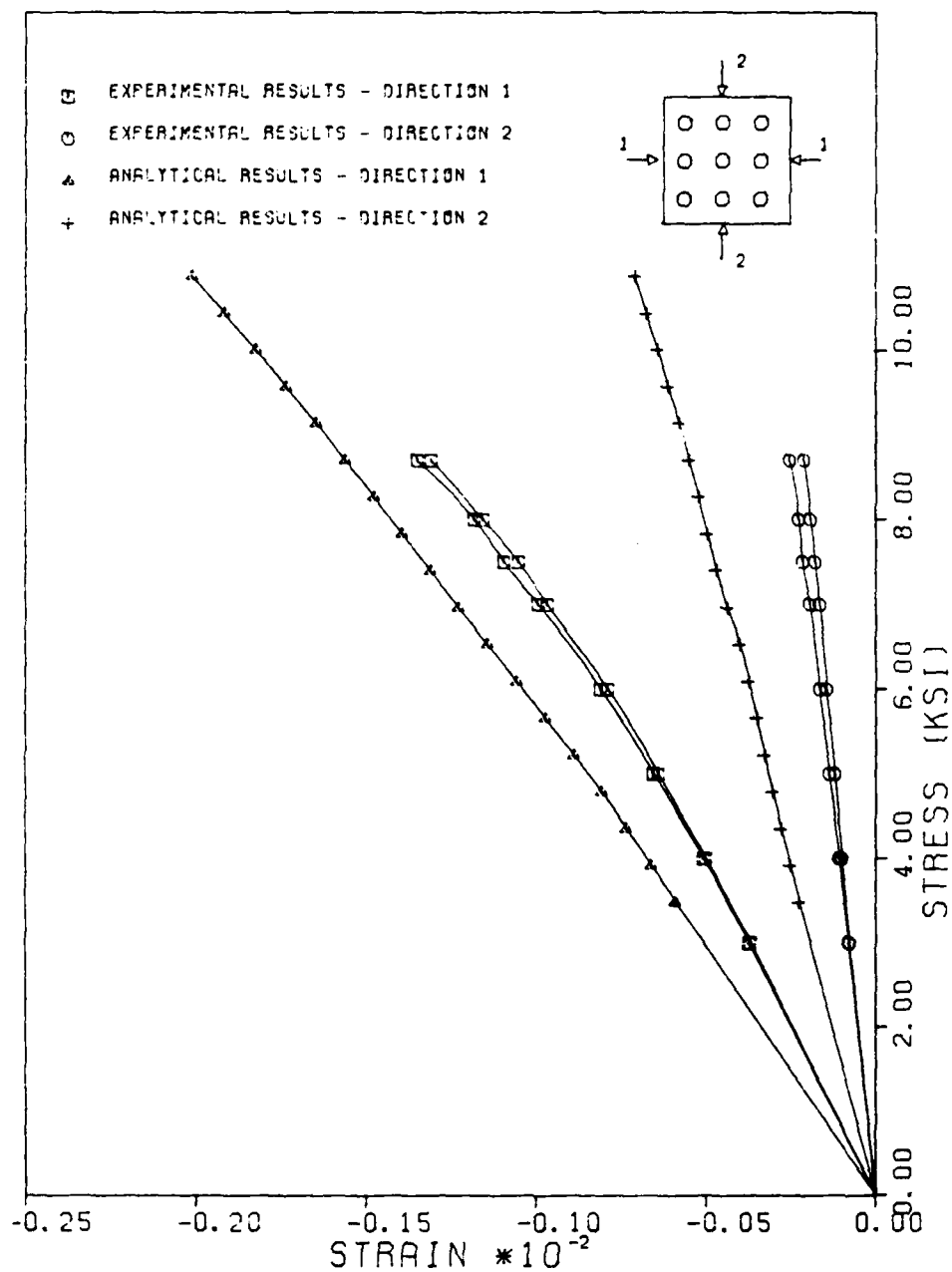


Fig. 6.25 Comparison between analytical and experimental results ($\sigma_1/\sigma_2 = 0.50$; $H = f(\sigma, k)$).

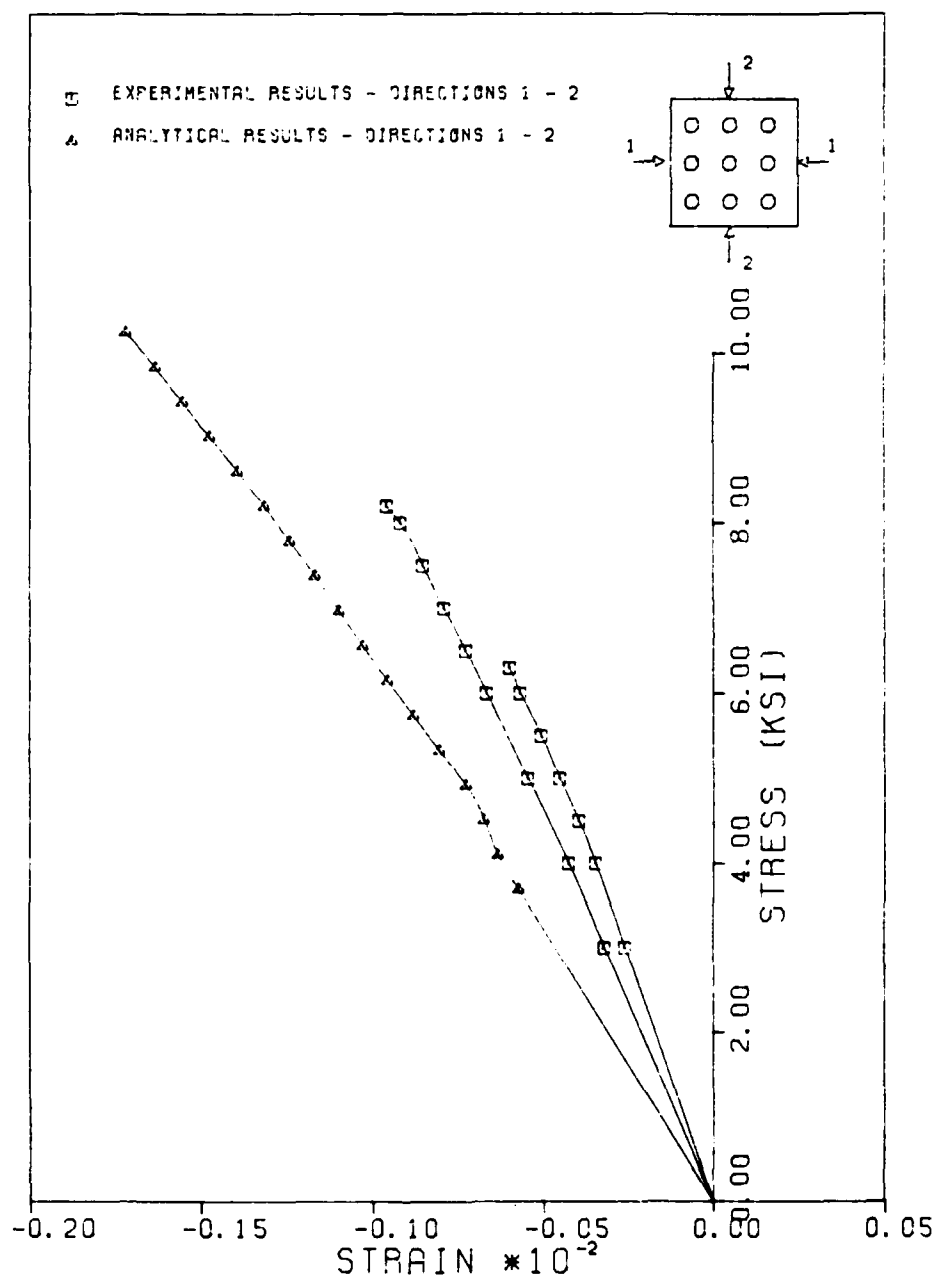


Fig. 6.26 Comparison between analytical and experimental results ($\sigma_1/\sigma_2 = 1.0$; $H = f(\sigma, k)$).

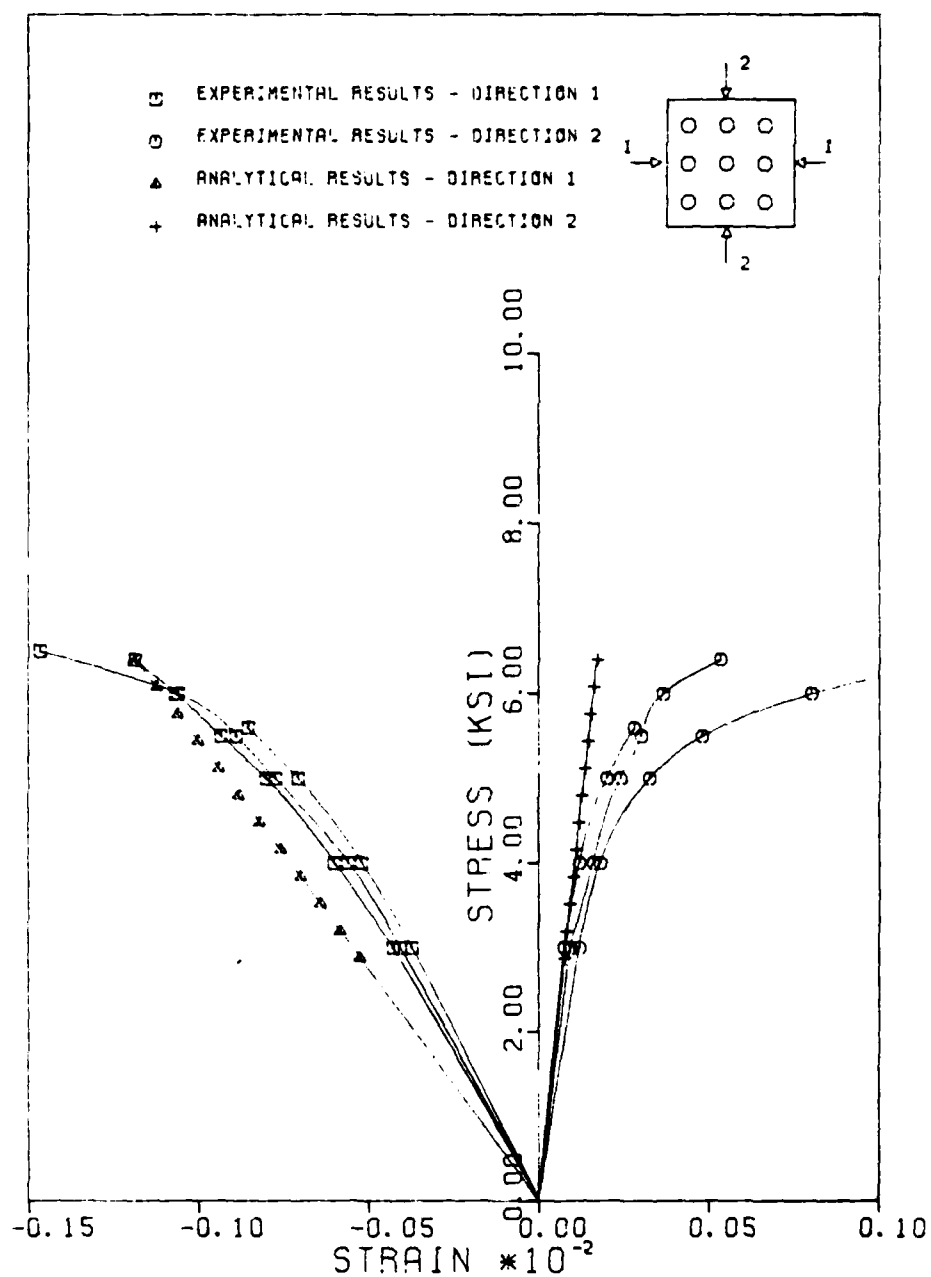


Fig. 6.27 Comparison between analytical and experimental results ($\sigma_2/\sigma_1 = 0.0$; $H = f(k)$).

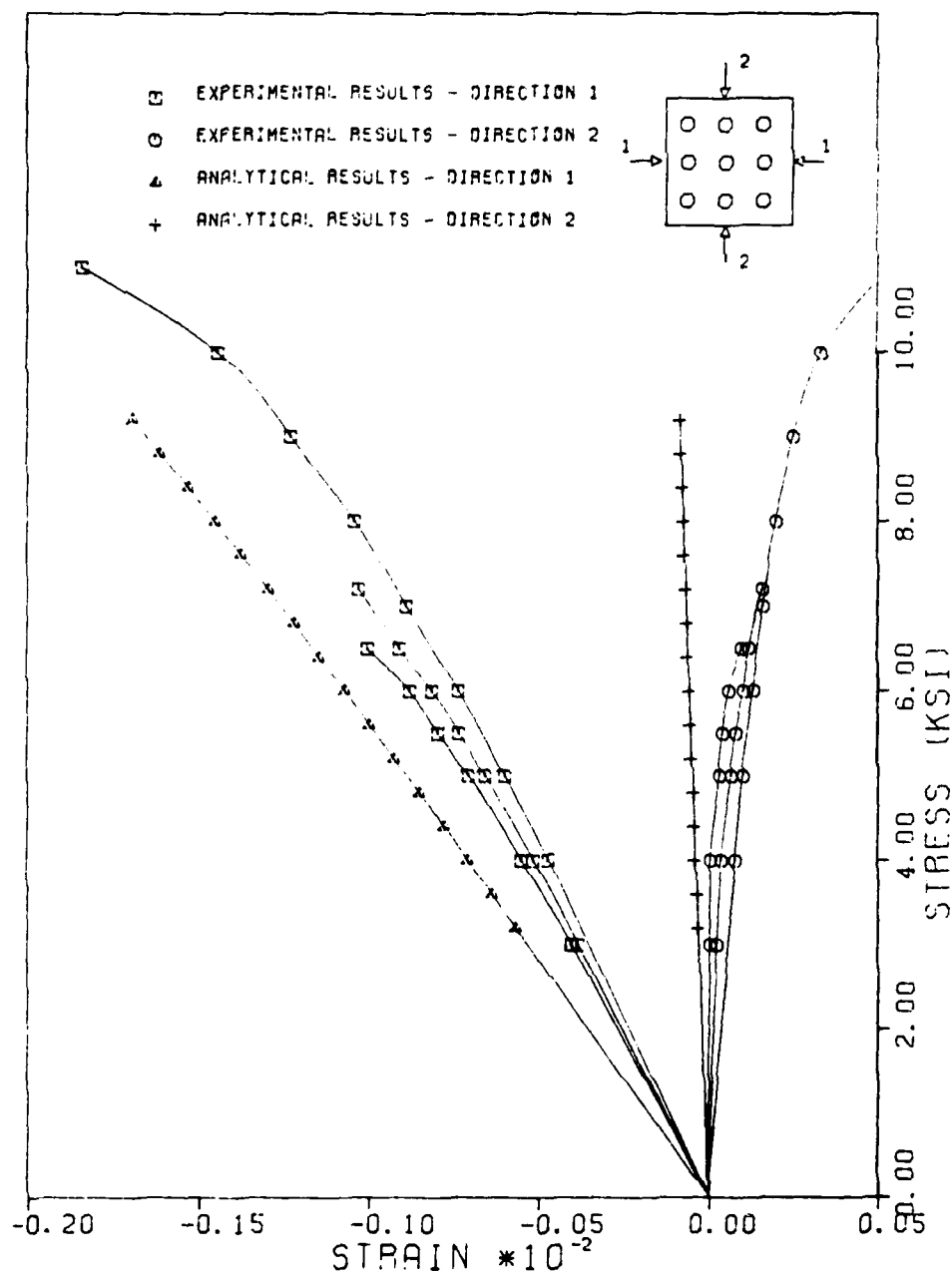


Fig. 6.28 Comparison between analytical and experimental results ($\sigma_2/\sigma_1 = 0.20$; $H = f(k)$).

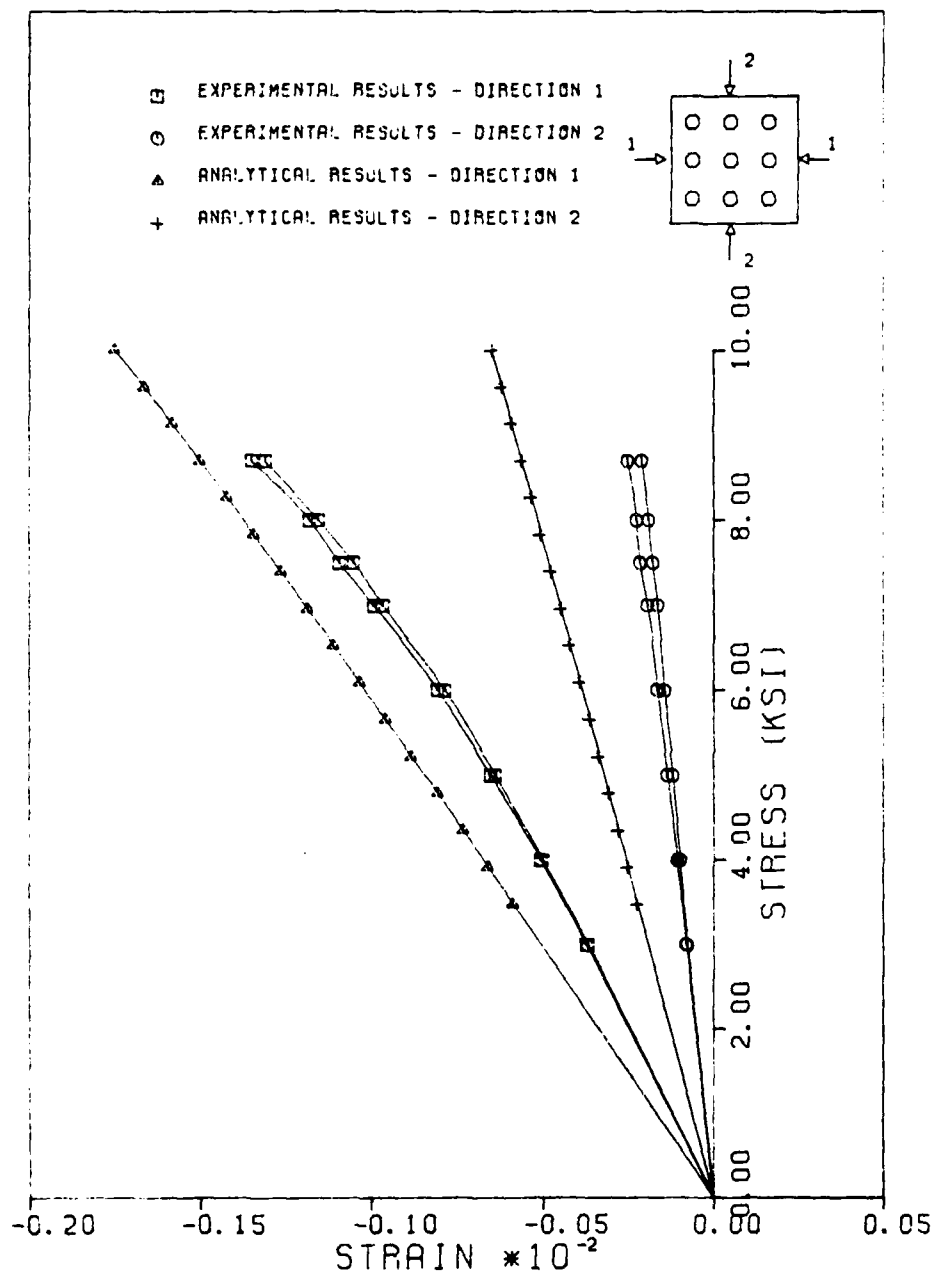


Fig. 6.29 Comparison between analytical and experimental results ($\sigma_2/\sigma_1 = 0.50$; $H = f(k)$).

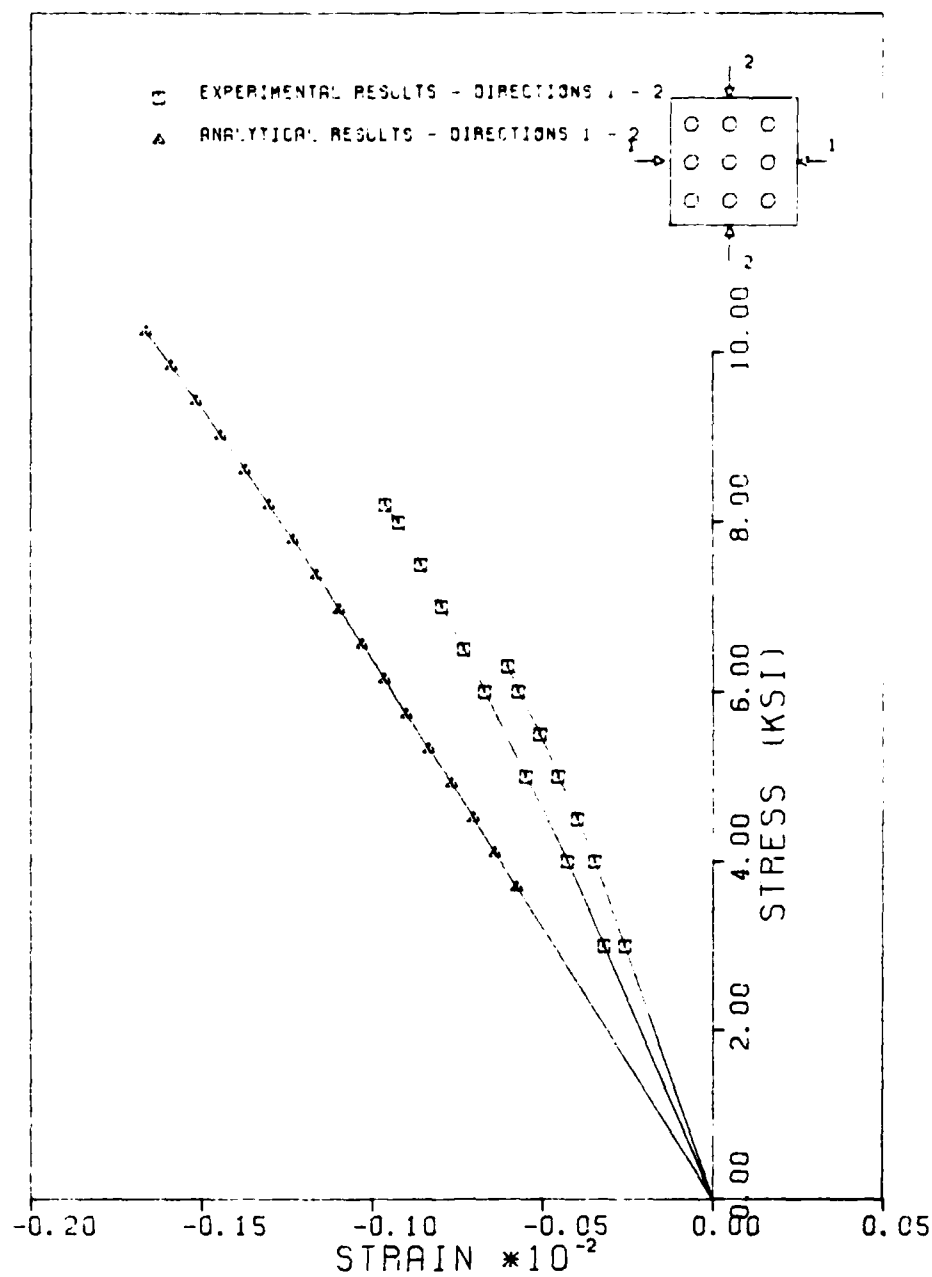


Fig. 6.30 Comparison between analytical and experimental results ($\sigma_2/\sigma_1 = 1.0$; $H = f(k)$).

interface and its analytical ultimate strength was increased. The load case $\sigma_2/\sigma_1 = 0.50$ showed a slight decrease in strength and less plastic deformation may be observed in all load cases.

The difference in stiffness between the analytical and the experimental results is attributed to the boundary conditions at the edges of the specimen in the experiments. The next part of this chapter will present analytical results for specimens with edge restraints imposed in the direction perpendicular to the direction of the applied load.

6.4 Analysis of Constrained Specimens

The question as to what the boundary conditions are at the edges of the specimen is not easily answered because no information is available about the degree and distribution of restraint provided by the loading device. If one tries, at what would be considered as extreme boundary conditions, to set equal to zero the edge displacements in the direction perpendicular to the direction of the applied load, a singularity in the displacement field is obtained at the corner. From one side the corner must have the same displacement as the other edge nodes and from the other side this same displacement is set equal to zero. If the displacements of the corner node are not prescribed equal to zero, a concentration of strains and therefore stresses is obtained in the elements in the neighborhood of the corner and premature failure of the specimen is predicted.

Any reasonable distribution of edge restraint is best justified if good agreement with the experimental results is obtained.

The concrete model was analyzed with rectangular elements attached to the boundary mortar elements in an attempt to simulate the loading device (Fig. 6.31). The elastic properties of these elements were set equal to the elastic properties of typical steel ($E = 2.90 \times 10^7$ psi, $\nu = 0.30$) and the dimension of the element in the direction of the applied load was set equal to the dimension of the loading device (0.75 in.). No relative displacement was allowed between the mortar and the steel elements and the load was applied at the edge nodes of the steel elements. The displacements of the edge nodes of the steel elements in the direction perpendicular to the direction of the applied load were set equal to zero.

The stress-strain curves obtained with these boundary conditions and the stress-strain curves obtained with no edge restraint of the concrete model are compared with the experimental results in Figs. 6.32 through 6.35. In uniaxial compression, the edge condition has negligible influence on the analytical results. The two curves are almost identical. In the other three load cases, the experimental results lie in between the two sets of analytical results. Obviously, a certain degree of relative displacement has occurred between the specimen and the loading device in the experiment.

Another way to impose edge restraint on the specimen was examined using the three-node bar element shown in Fig. 6.36. Such elements were attached to the boundary mortar elements in order to decrease the edge displacements in the direction perpendicular to the direction of the applied load. The stiffness matrix of this

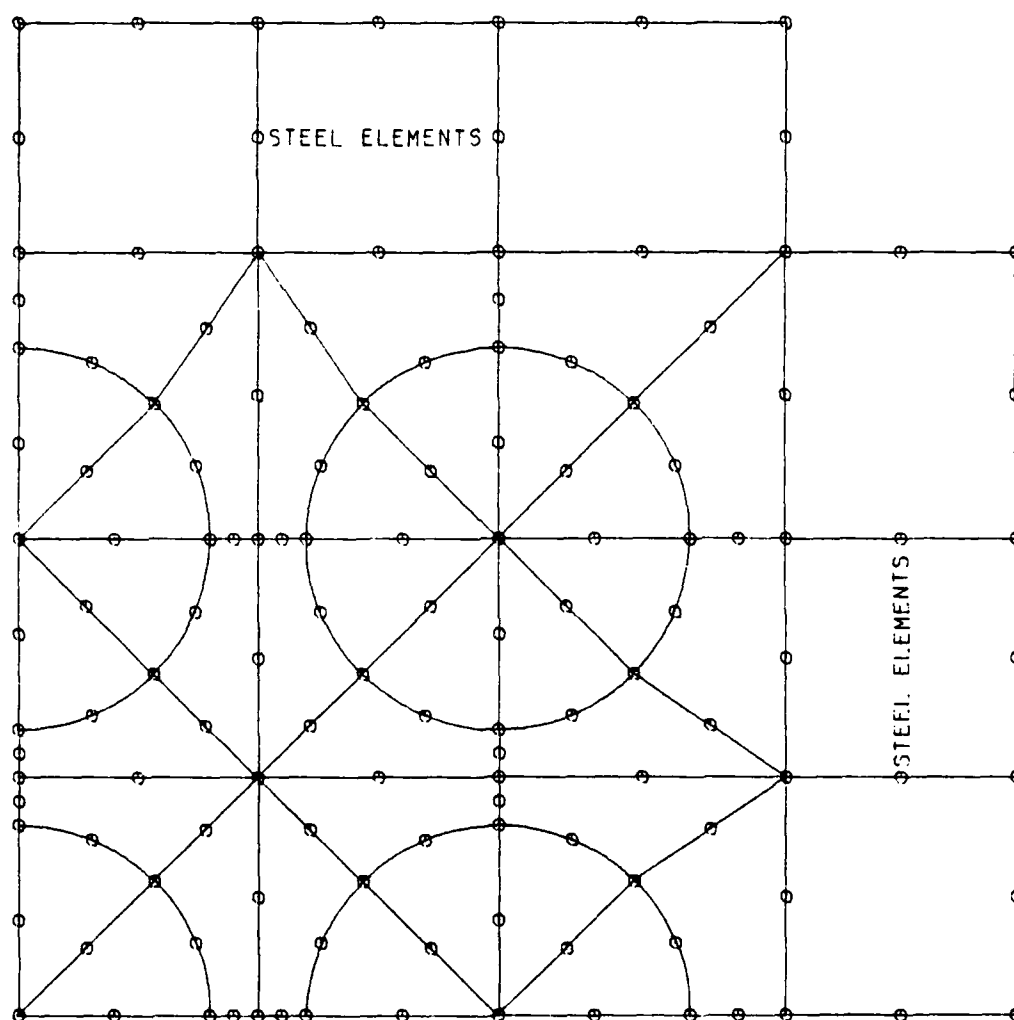


Fig. 6.31 Finite element mesh with steel elements attached.

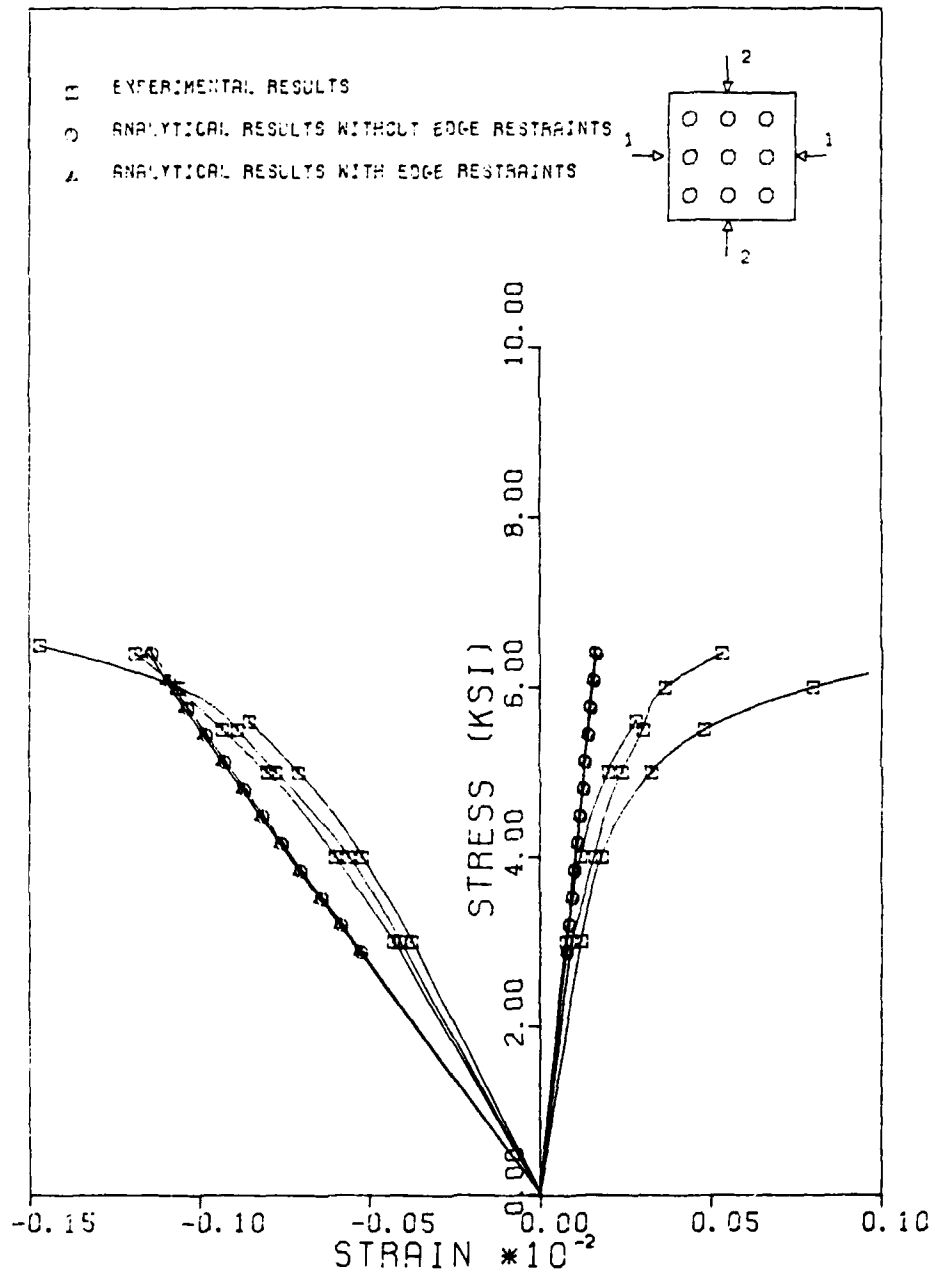


Fig. 6.32 Comparison between analytical results with and without edge restraints and the experimental results ($\sigma_2/\sigma_1 = 0.0$).

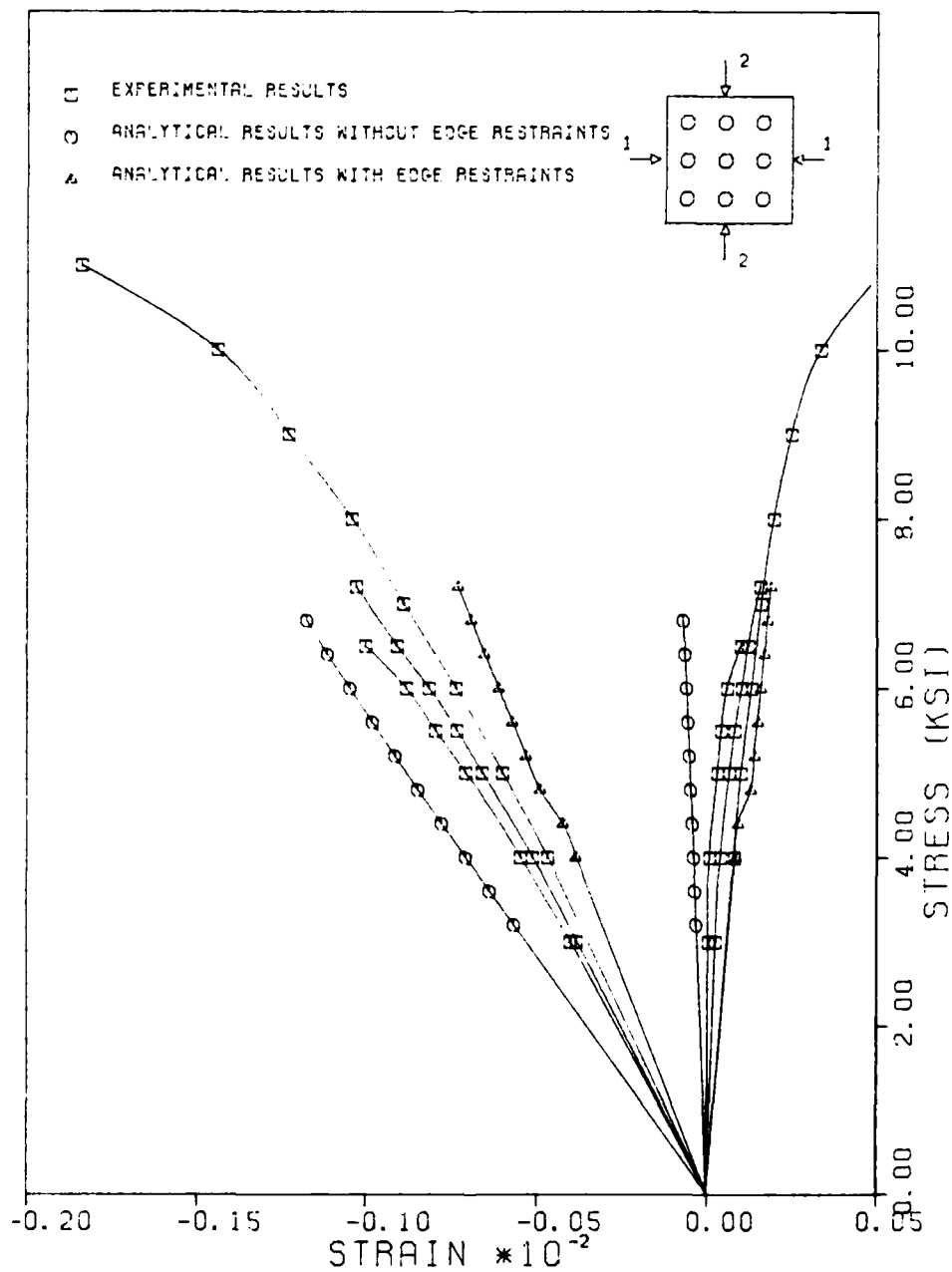


Fig. 6.33 Comparison between analytical results with and without edge restraints and the experimental results ($\sigma_2/\sigma_1=0.20$).

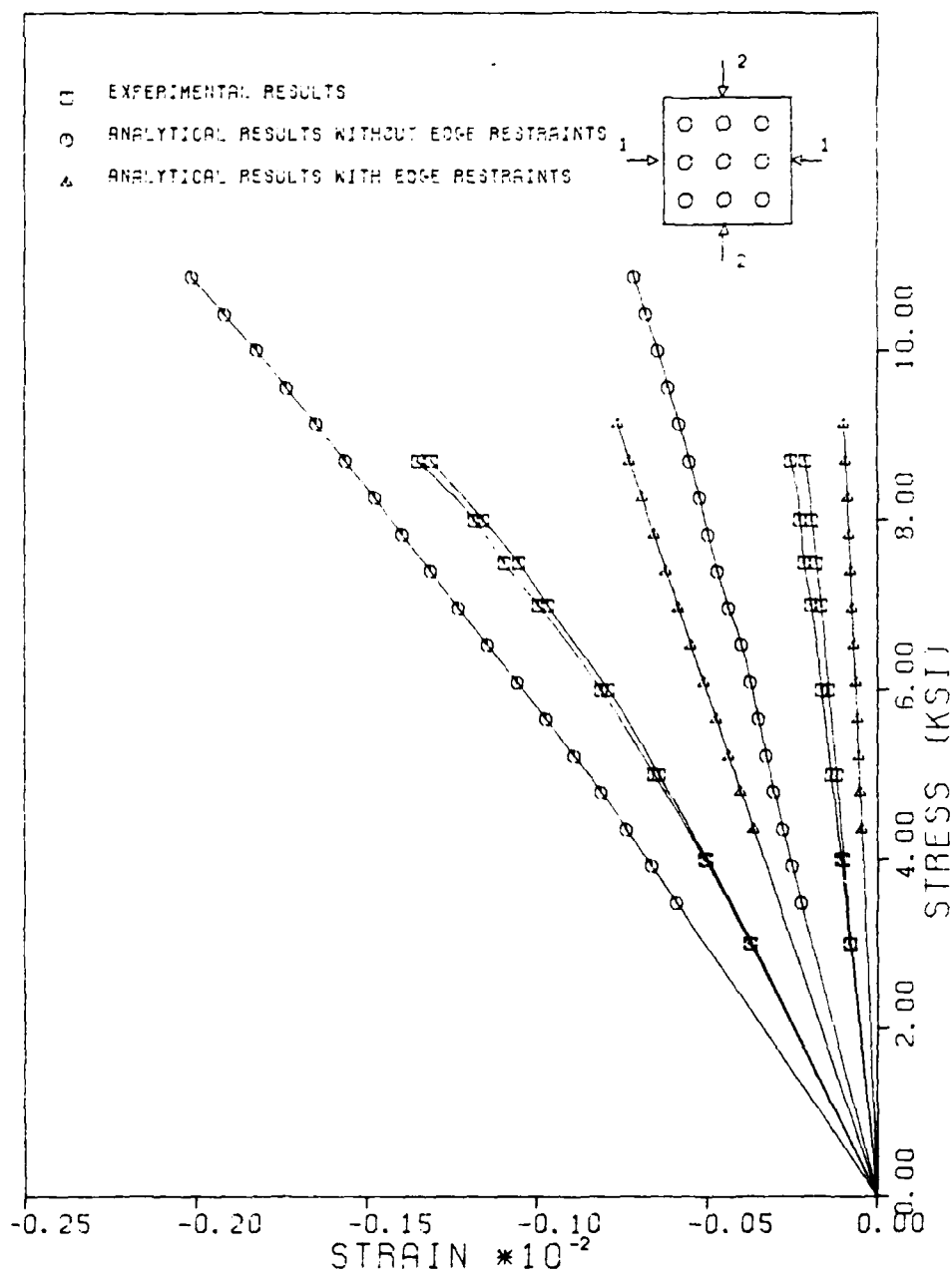


Fig. 6.34 Comparison between analytical results with and without edge restraints and the experimental results ($\sigma_2/\sigma_1=0.50$).

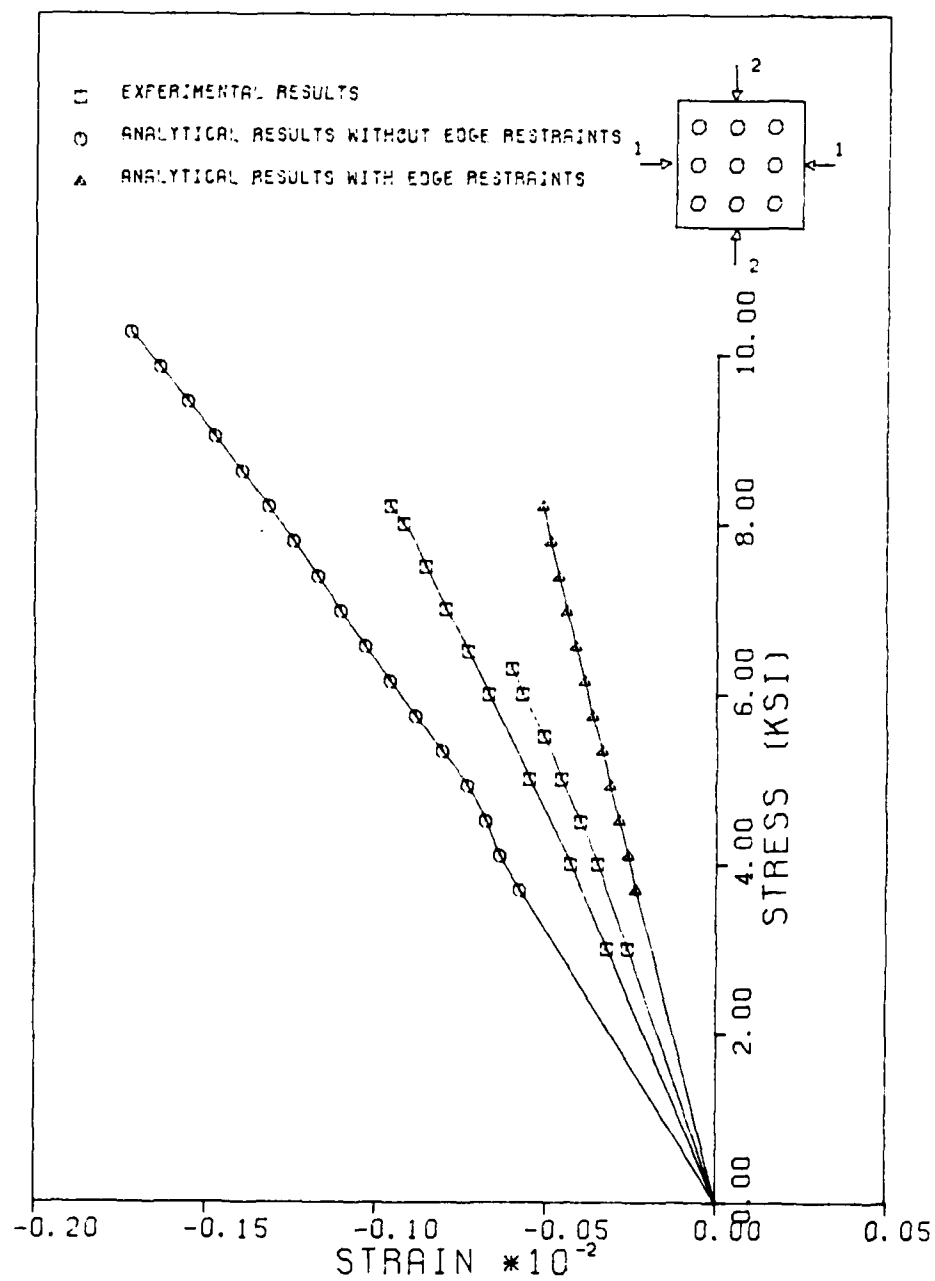


Fig. 6.35 Comparison between analytical results with and without edge restraints and the experimental results ($\sigma_2/\sigma_1=1.0$).

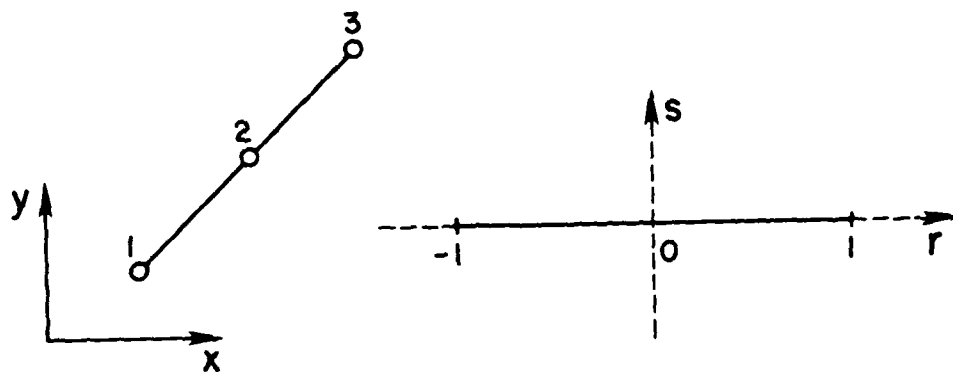


Fig. 6.36 Three-node bar element used in the constrained analysis of the specimen.

element was obtained numerically using three Gaussian integration points. The element axial stiffness was assumed to vary linearly along the element length. Thus, during the integration of the element stiffness matrix, each integration point had a different value of the stiffness assigned. In order to avoid the high concentration of strains and stresses in the corner elements, this axial stiffness was distributed linearly from zero at the corner node (node 100 in Fig. 4.1) to a maximum value at the middle of a side of the specimen (nodes 13 and 94 in Fig. 4.1). This maximum value of axial stiffness was calibrated with the experimental results in equal biaxial compression in order to have the same initial elastic stiffness in the stress-strain curve. A value equal to $4.2 \times 10^7 \text{ lb/in}$ was obtained, then used for all the load cases. The analytical results obtained under these assumptions regarding the boundary conditions are compared

to the experimental results in Figs. 6.37 through 6.40. A better agreement in stiffness and ultimate strength may be observed.

A representation of the magnitude of the hardening parameter k at different levels of load for the four load cases is shown in Figs. 6.41 through 6.52 for the above described boundary conditions. With the exception of the uniaxial load case, the inelasticity starts and develops with more intensity at the corner of the specimen. The failure of the specimen is seen to be premature because of the edge conditions.

6.5 Analysis Shortcomings

The linear finite element analysis of the concrete model is expected to predict stiffer behavior than the exact solution due to the discretization. The error, however, is not large for the discretization used in this analysis and the results are accurate enough as demonstrated in Section 4.2.5. This observation establishes beyond any doubt that the specimens were constrained by the heads of the loading device in the experiments.

The accuracy of the nonlinear analysis is mainly influenced by the accuracy of the constitutive model used for the mortar. The model has proved to be accurate for normal-strength concrete under biaxial states of stress (Ref. 1) but has not yet been tested for high-strength mortar under multiaxial states of stress since no experimental data are available.

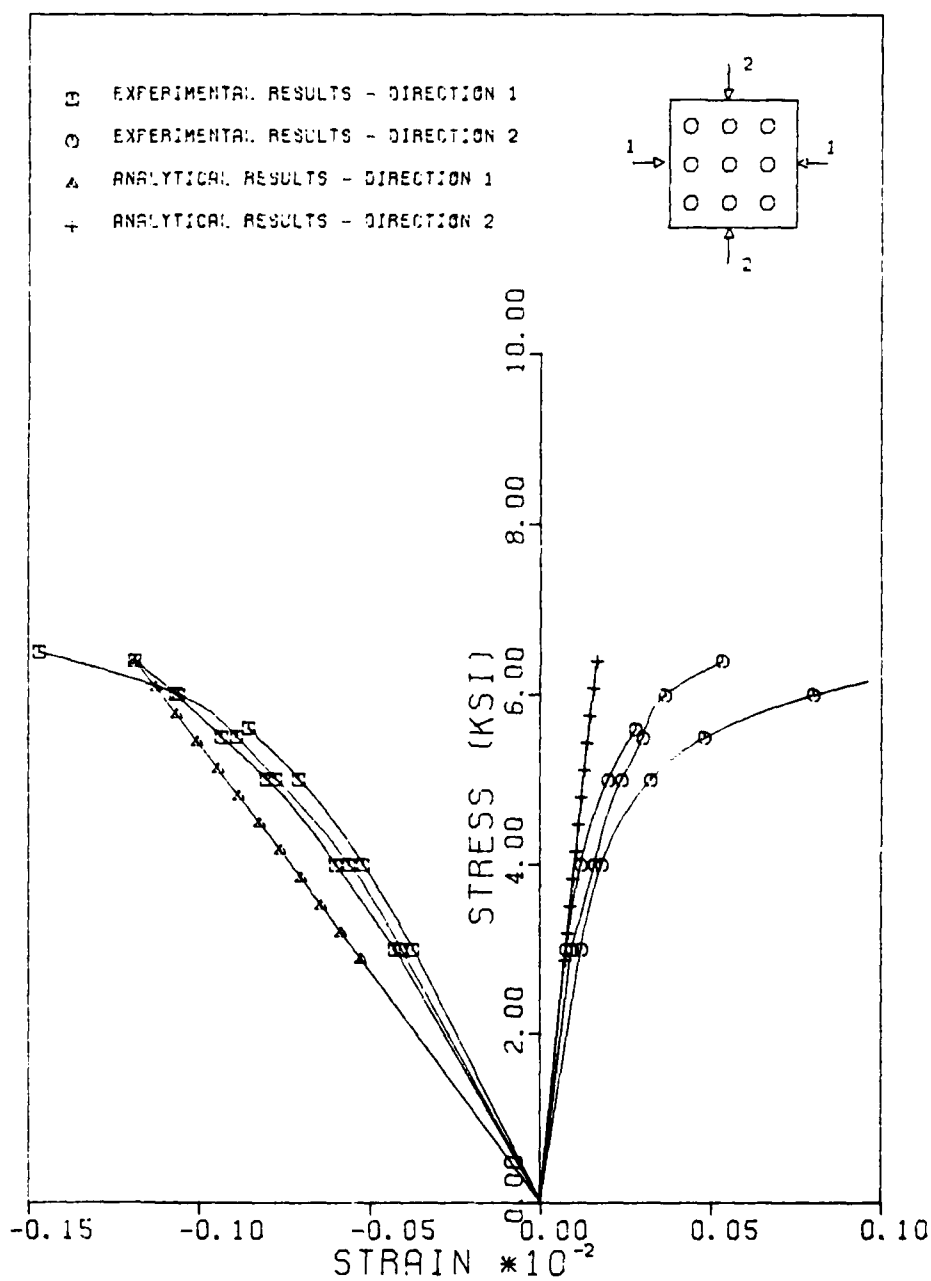


Fig. 6.37 Comparison between analytical results with edge stiffening elements attached and the experimental results ($\sigma_2/\sigma_1=0.0$).

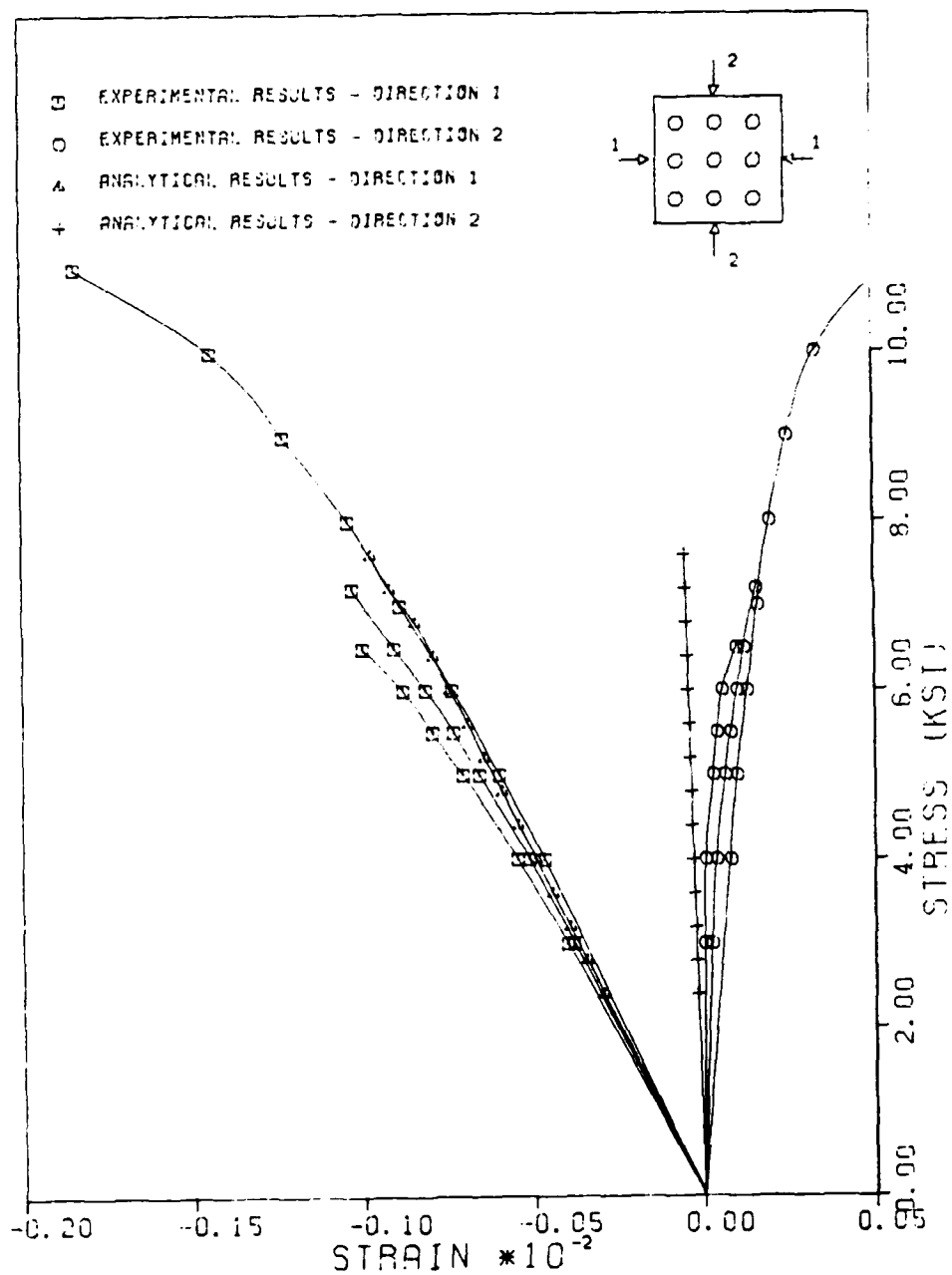


Fig. 6.38 Comparison between analytical results with edge stiffening elements attached and the experimental results ($\sigma_2/\sigma_1=0.20$).

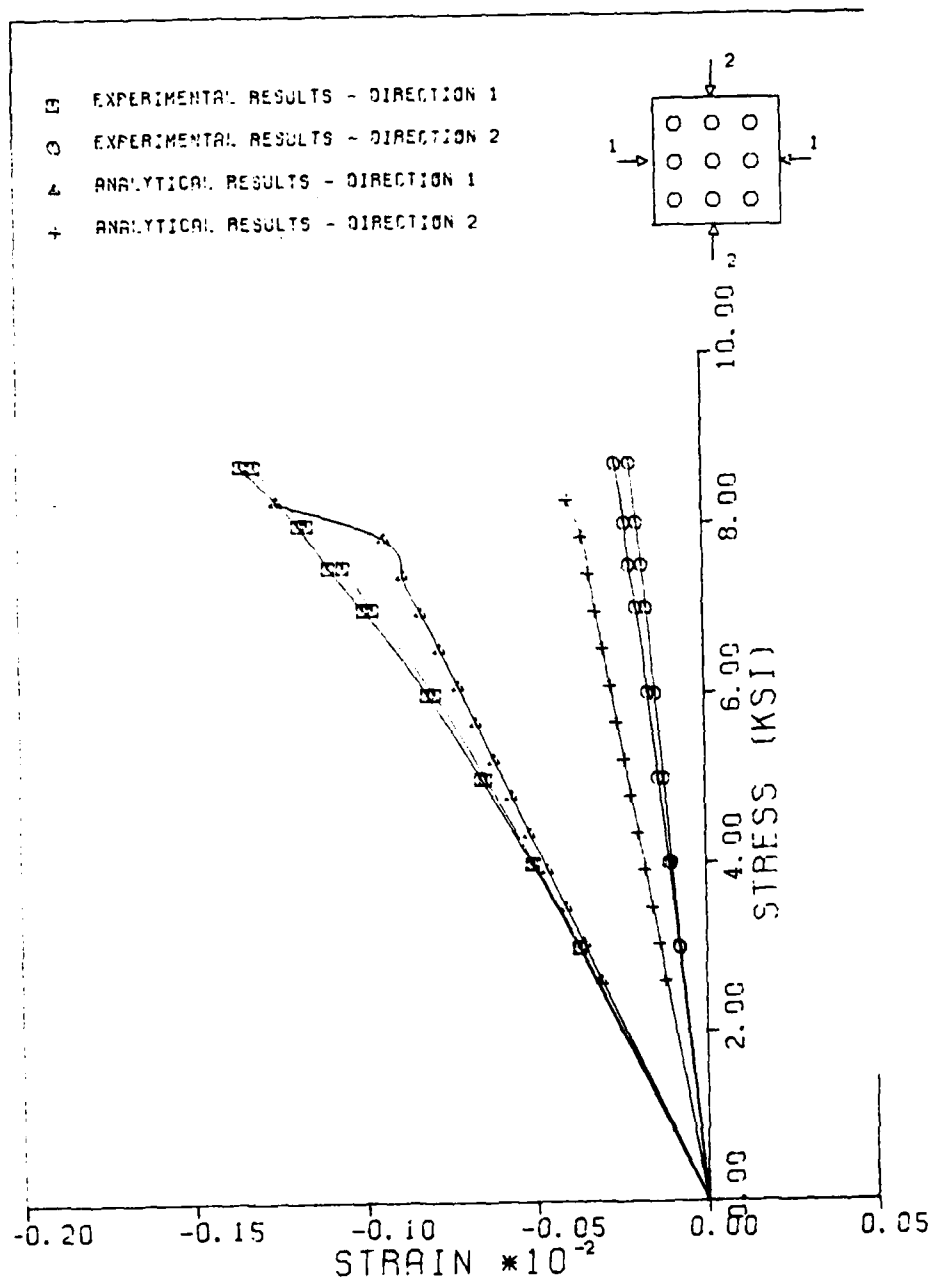


Fig. 6.39 Comparison between analytical results with edge stiffening elements attached and the experimental results ($\sigma_2/\sigma_1=0.50$).

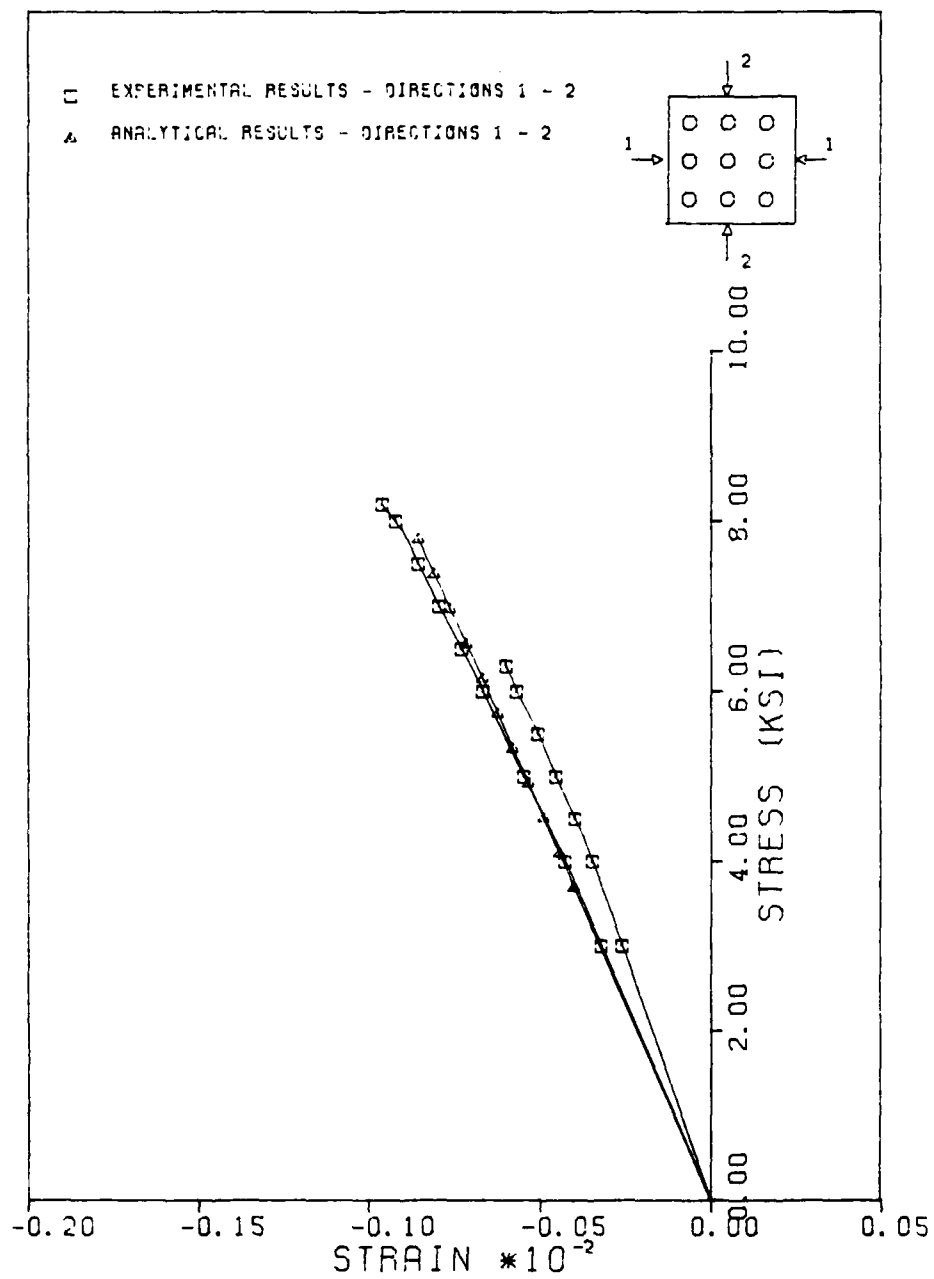


Fig. 6.40 Comparison between analytical results with edge stiffening elements attached and the experimental results ($\sigma_2/\sigma_1=1.0$).

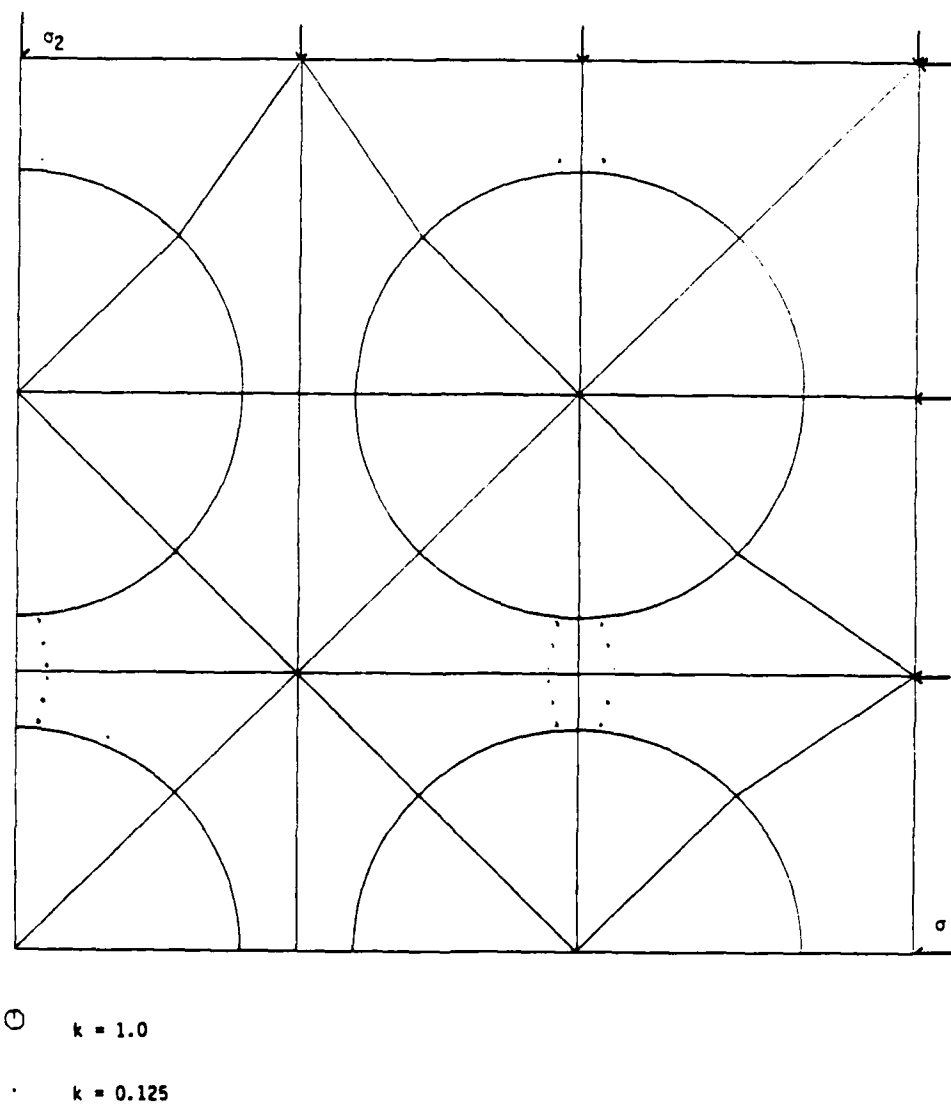
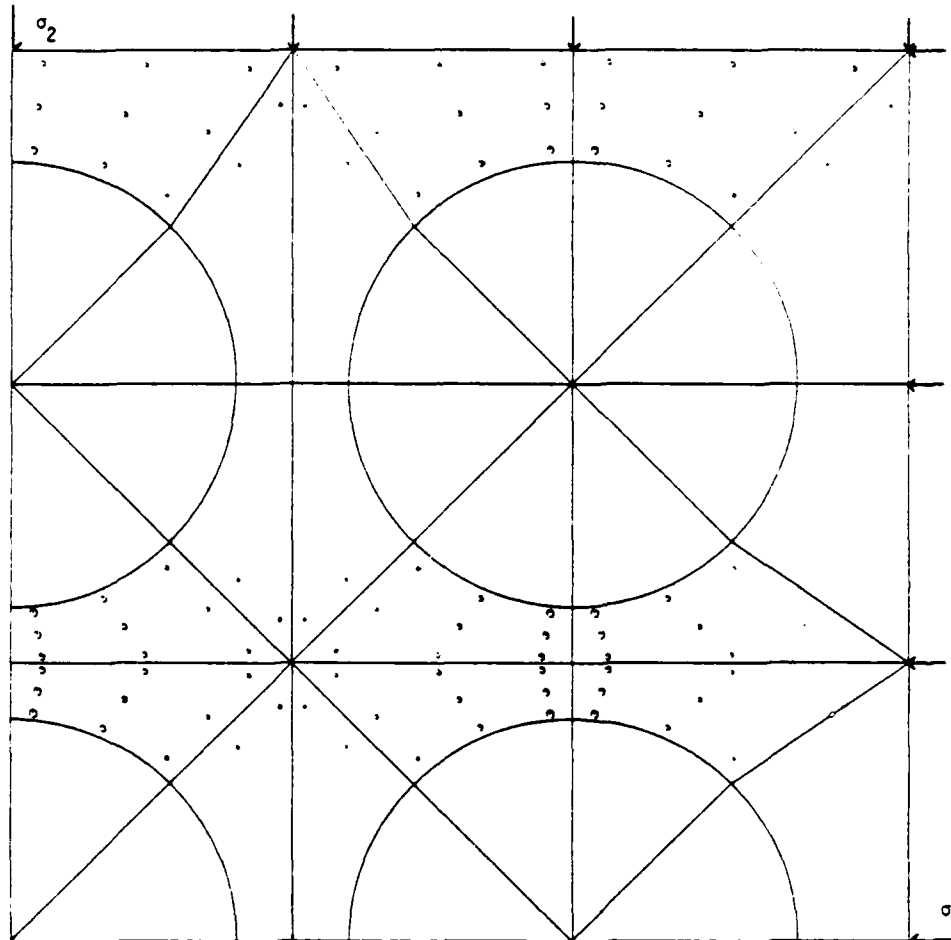


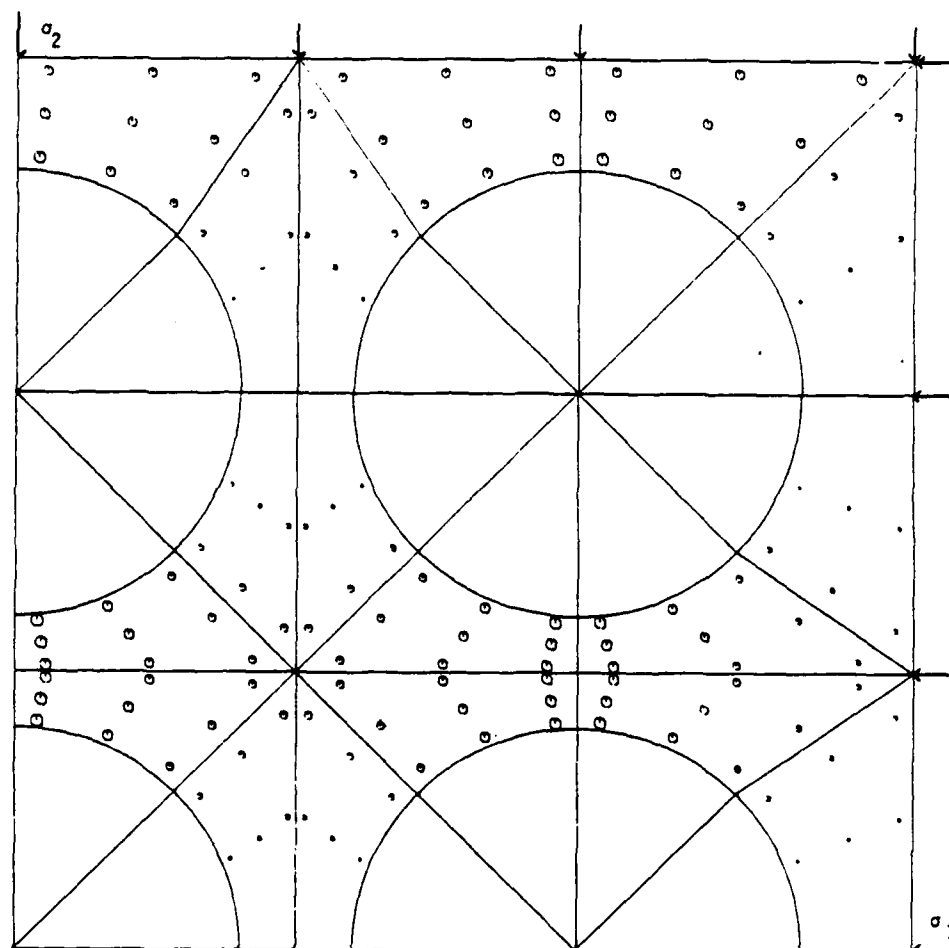
Fig. 6.41 Degree of damage in the specimen at 65 percent of the analytical ultimate strength with the edge stiffening elements attached ($\sigma_2/\sigma_1 = 0.0$).



⊙ $k = 1.0$

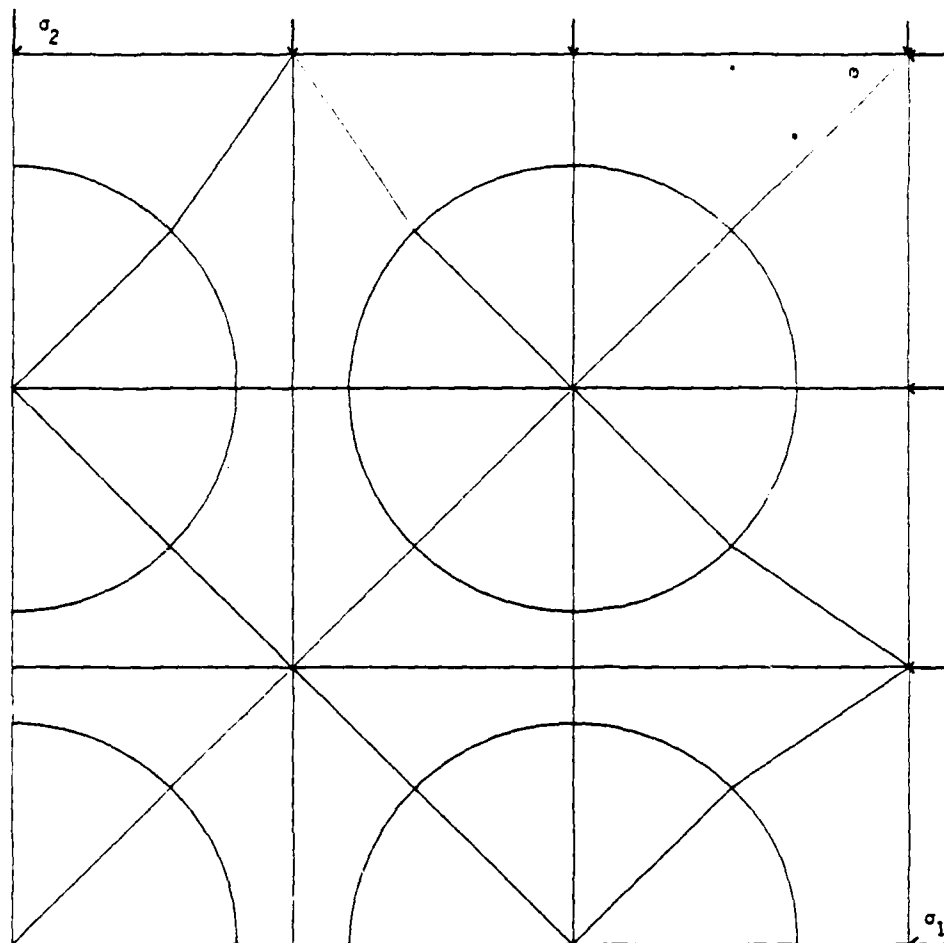
• $k = 0.125$

Fig. 6.42 Degree of damage in the specimen at 80 percent of the analytical ultimate strength with the edge stiffening elements attached ($\sigma_2/\sigma_1 = 0.0$).



○ $k = 1.0$
 . $k = 0.125$

Fig. 6.43 Degree of damage in the specimen at the analytical ultimate strength with the edge stiffening elements attached ($\sigma_2/\sigma_1 = 0.0$).



○ $k = 1.0$

• $k = 0.125$

Fig. 6.44 Degree of damage in the specimen at 58 percent of the analytical ultimate strength with the edge stiffening elements attached ($\sigma_2/\sigma_1 = 0.20$).

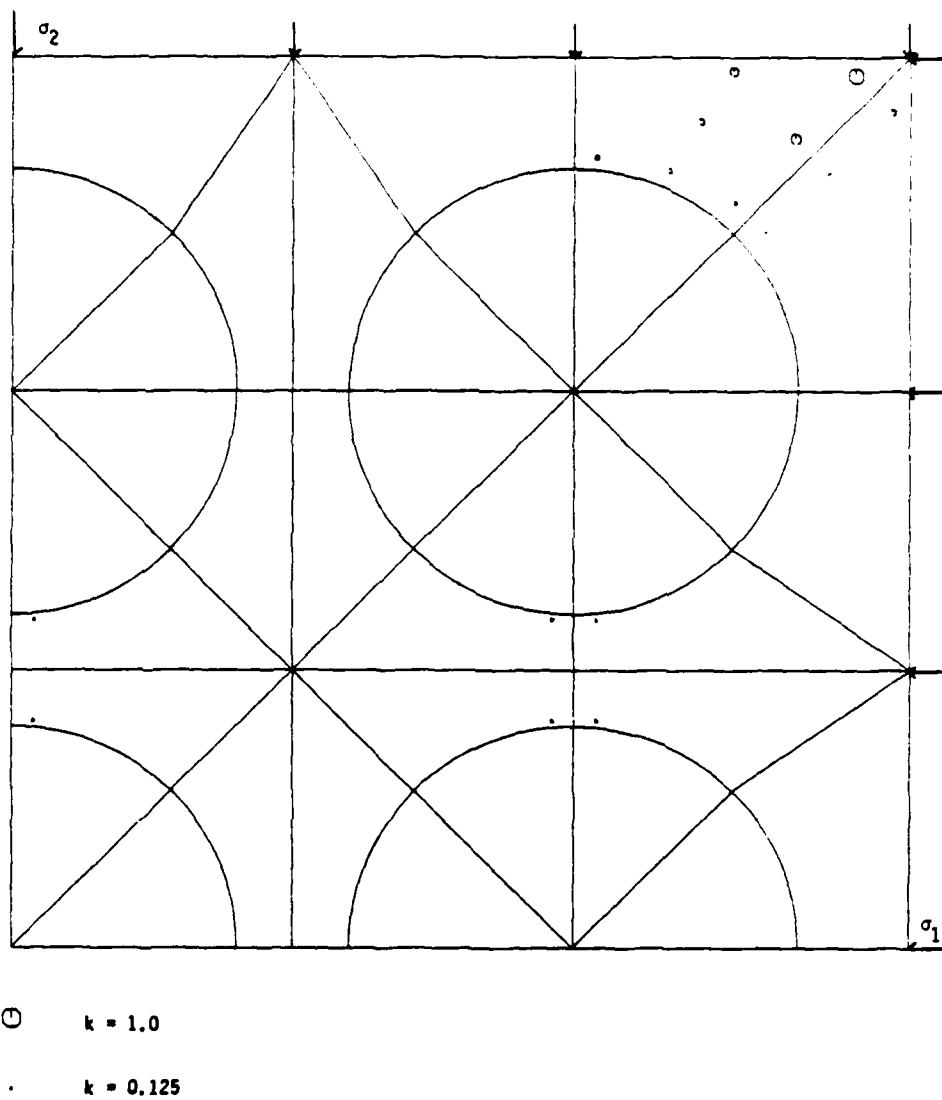


Fig. 6.45 Degree of damage in the specimen at 79 percent of the analytical ultimate strength with the edge stiffening elements attached ($\sigma_2/\sigma_1 = 0.20$).

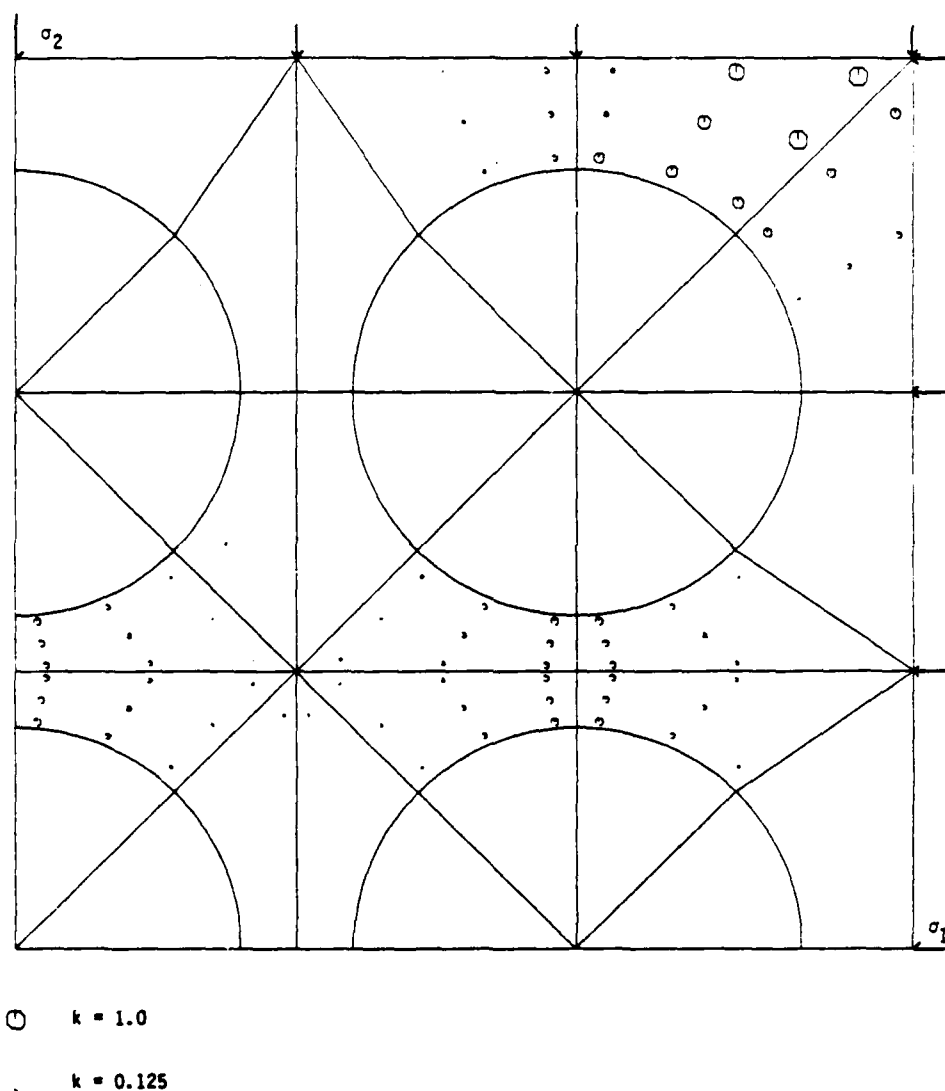
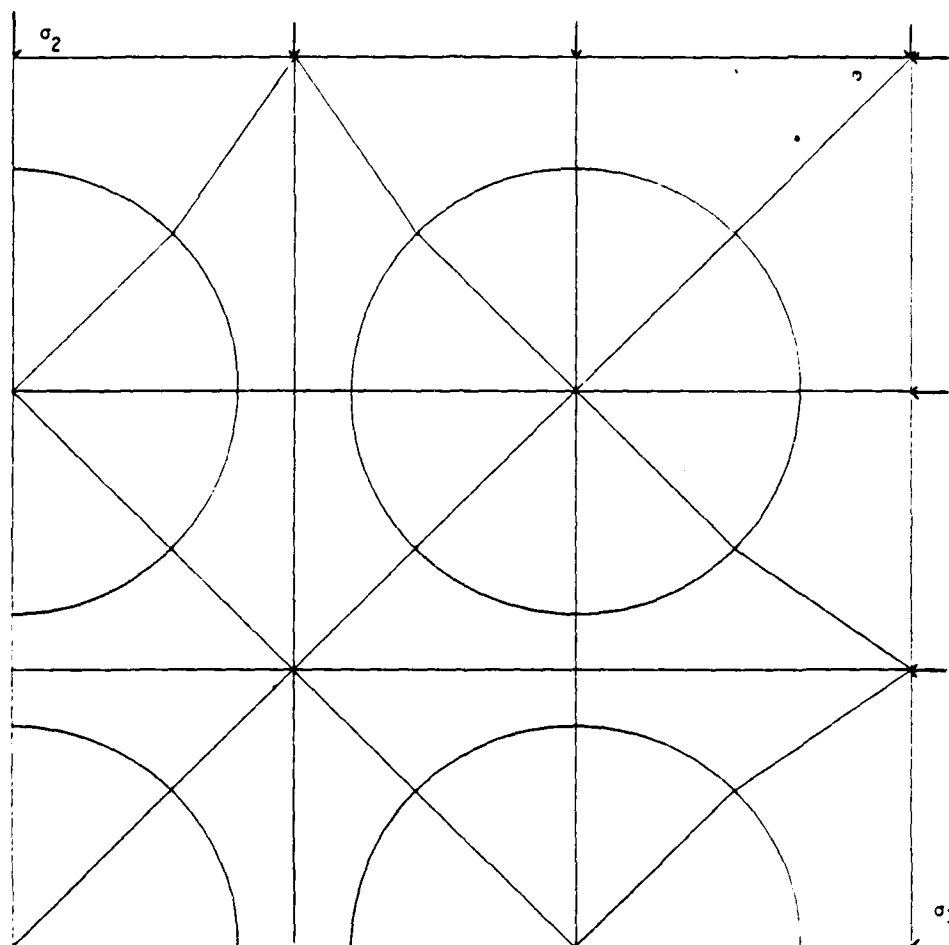


Fig. 6.46 Degree of damage in the specimen at the analytical ultimate strength with the edge stiffening elements attached ($\sigma_2/\sigma_1 = 0.20$).



⊙ $k = 1.0$

• $k = 0.125$

Fig. 6.47 Degree of damage in the specimen at 53 percent of the analytical ultimate strength with the edge stiffening elements attached ($\sigma_2/\sigma_1 = 0.50$).

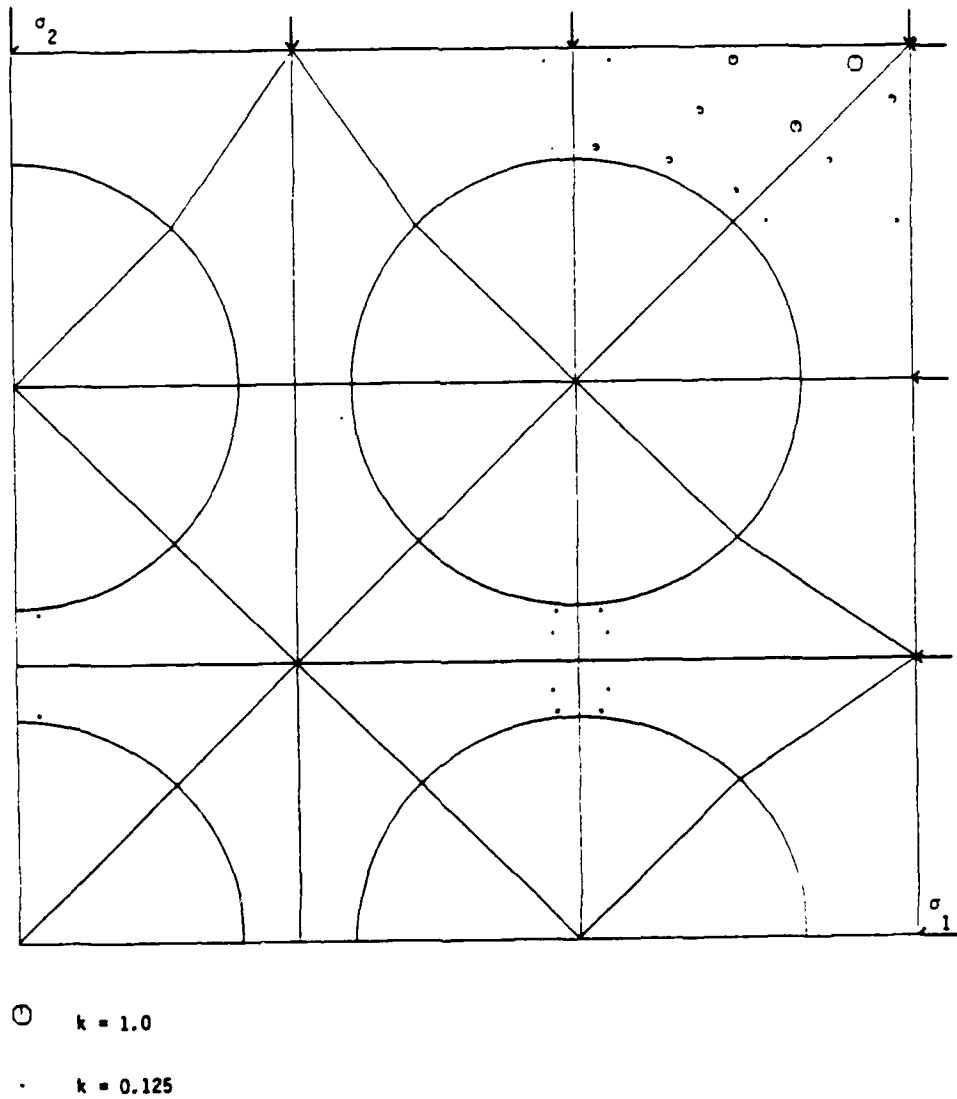


Fig. 6.48 Degree of damage in the specimen at 79 percent of the analytical ultimate strength with the edge stiffening elements attached ($\sigma_2/\sigma_1 = 0.50$).

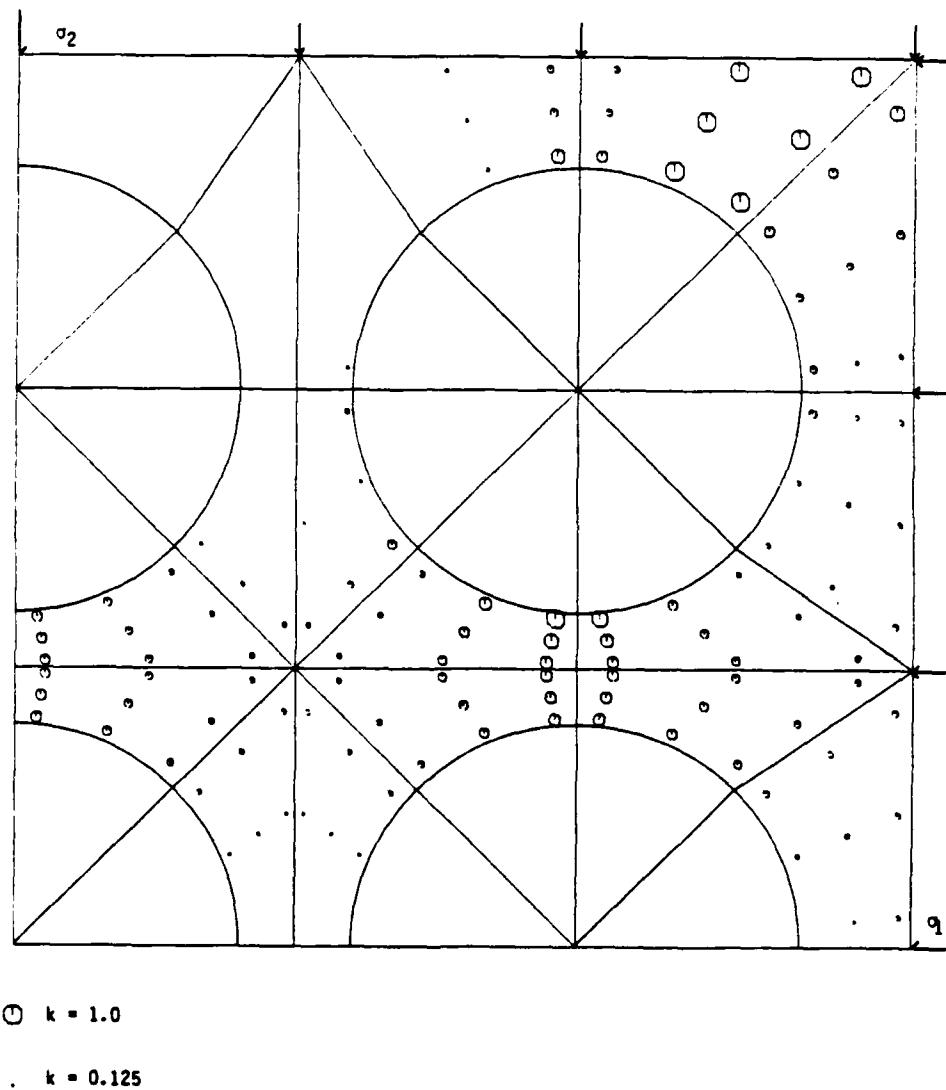
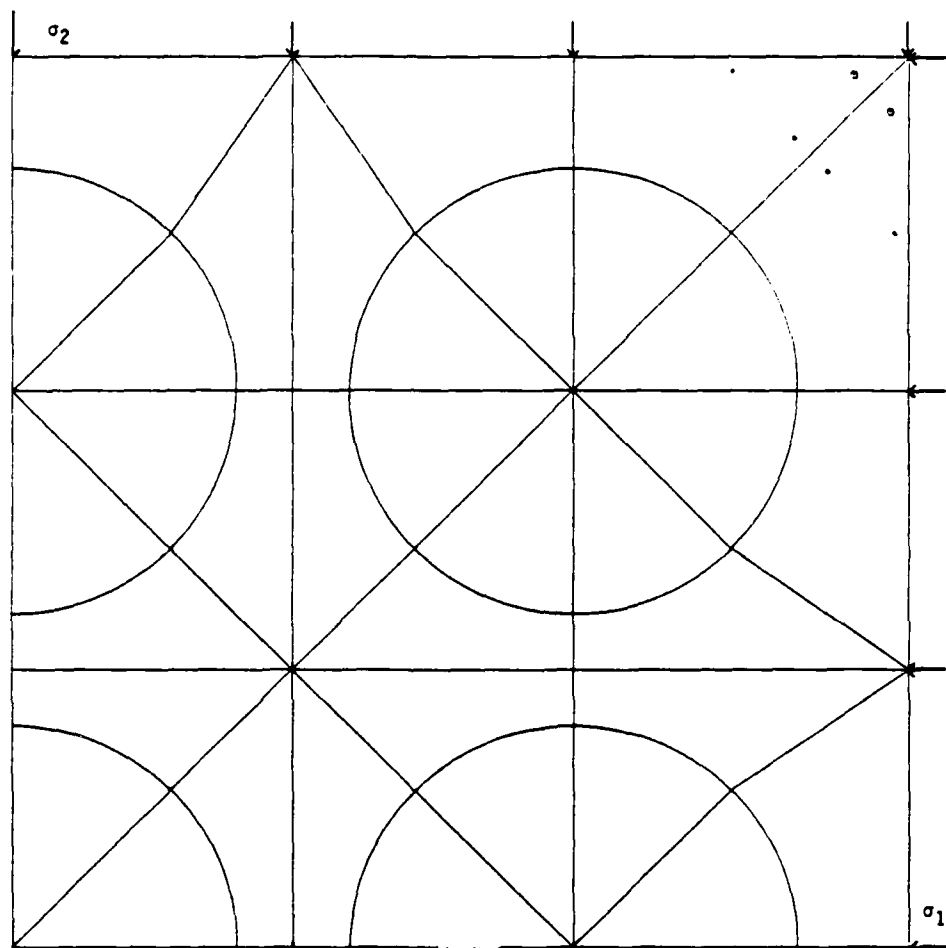


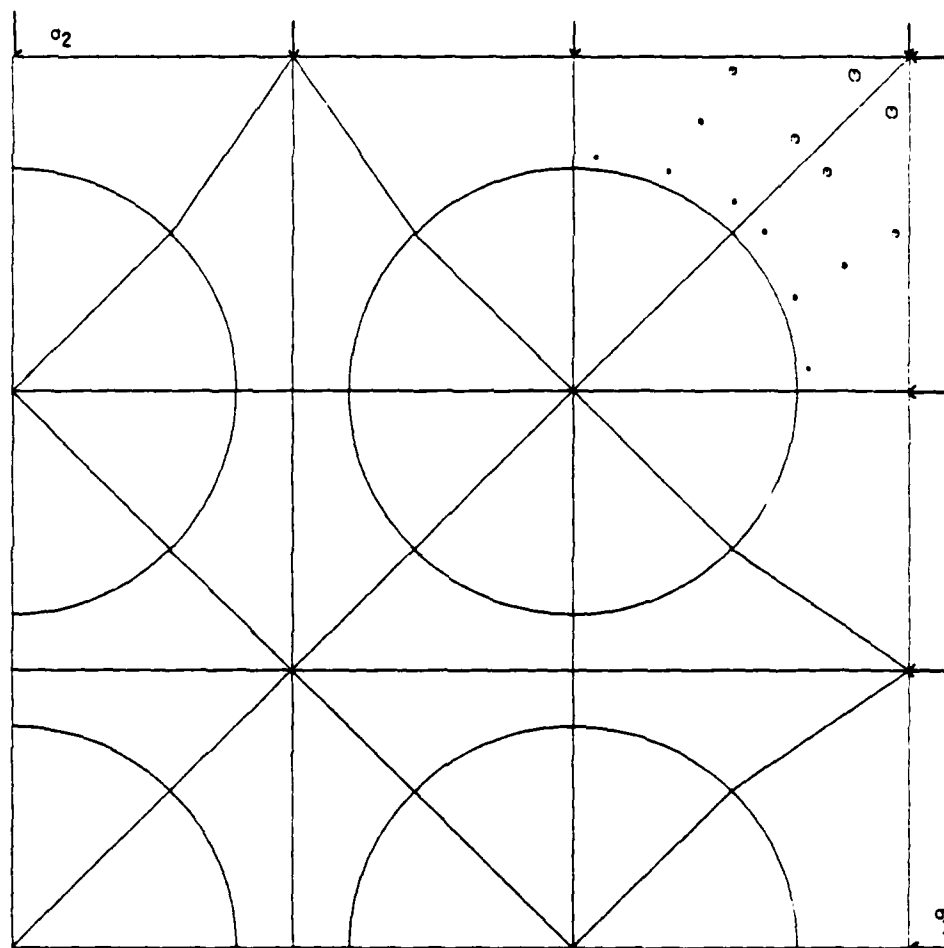
Fig. 6.49 Degree of damage in the specimen at the analytical ultimate strength with the edge stiffening elements attached ($\sigma_2/\sigma_1 = 0.50$).



○ $k = 1.0$

• $k = 0.125$

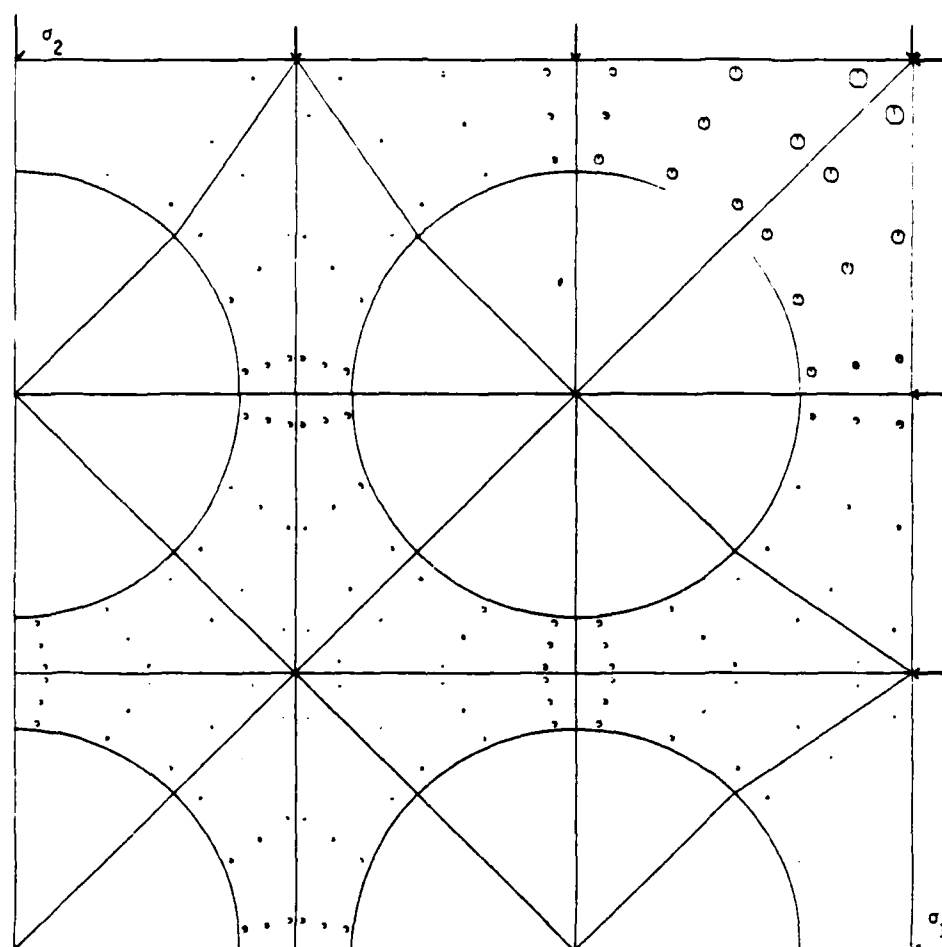
Fig. 6.50 Degree of damage in the specimen at 58 percent of the analytical ultimate strength with the edge stiffening elements attached ($\sigma_2/\sigma_1 = 1.0$).



○ $k = 1.0$

• $k = 0.125$

Fig. 6.51 Degree of damage in the specimen at 74 percent of the analytical ultimate strength with the edge stiffening elements attached ($\sigma_2/\sigma_1 = 1.0$).



○ $k = 1.0$

· $k = 0.125$

Fig. 6.52 Degree of damage in the specimen at the analytical ultimate strength with the edge stiffening elements attached ($\sigma_2/\sigma_1 = 1.0$).

The bond properties used for the mortar-aggregate interface modeling may not be accurate and experimental studies of the bond between the coarse aggregate and high-strength mortar are yet to be performed. An increase in the number of interface points used to check for bond failure may also yield more accurate modeling of the interface.

The differences in stiffness between the analytical and the experimental results in uniaxial compression cannot be attributed to the restraints imposed on the edge of the specimen only. Other factors may be responsible for the disagreement such as difference between the elastic properties of the component materials as obtained from tests on cylindrical specimens and their actual values in the concrete model as well as possible eccentricities in the loading device.

CHAPTER 7

SUMMARY AND CONCLUSIONS

7.1 Summary

This present work describes a finite element analysis of a high-strength concrete model under short-term monotonic biaxial compressive loading. The concrete model consists of a square mortar plate with nine coarse aggregate circular inclusions (Fig. 2.1).

The analysis takes into account the nonlinear behavior of the mortar using a constitutive model proposed in Ref. 1. The significance of the bond between the coarse aggregate and the mortar is also studied using an interface element developed in this work. The analytical results are then compared with experimental ones.

7.2 Conclusions

The following conclusions may be drawn from this work:

1. The strength of the bond between the coarse aggregate and the mortar appears to be the most significant factor influencing the strength of the concrete model in uniaxial compression.
2. Except for low values of the stress ratio σ_2/σ_1 (e.g., $\sigma_2/\sigma_1 = 0.20$), the analysis predicts that the bond between the coarse aggregate and the mortar remains intact up to ultimate strength of the concrete and it is failure in the mortar matrix that leads to failure of the model.

3. Mild stress concentrations were observed in all load cases. Although significant stress concentrations certainly appear around aggregates in high-strength concrete, this phenomenon, apparently, is not captured in the concrete model (circular aggregates).

4. The damage in the concrete starts and develops most conspicuously in the regions between two aggregates in the direction perpendicular to the direction of application of the largest stress.

5. The boundary conditions at the edges of the specimen have negligible influence on the strength and stiffness of the concrete model subjected to uniaxial compression.

6. The boundary conditions at the edges of the specimen most significantly affect the strength and stiffness of the concrete model in biaxial compression.

R E F E R E N C E S

1. Tassoulas, J. L., "Inelastic Behavior of Concrete in Compression," thesis submitted to the Department of Civil Engineering, M.I.T., in partial fulfillment of the requirements for the degree of Master of Science, June 1979.
2. Buyukozturk, O., Nilson, A. H., and Slate, F. O., "Stress-Strain Response and Fracture of a Concrete Model in Biaxial Loading," Journal of the American Concrete Institute, August 1971, vol. 68, pp. 590-599.
3. Freedman, S., "High-Strength Concrete," publication No. 1S176, Portland Cement Association, 1971, 19 pp.
4. Carrasquillo, R. L., Slate, F. O., and Nilson, A. H., "Micro-cracking and Behavior of High-Strength Concrete Subjected to Short-Term Loading," Journal of the American Concrete Institute, May/June 1981, vol. 78, no. 15, pp. 179-186.
5. Kupfer, H., Hulsdorf, H. K., and Rusch, H., "Behavior of Concrete Under Biaxial Stresses," Journal of the American Concrete Institute, vol. 66, no. 8, August 1969, pp. 656-666.
6. Zienkiewicz, O. C., The Finite Element Method (New York: McGraw-Hill, 1977).
7. Irons, B., and Ahmad, S., Techniques of Finite Elements (New York: John Wiley and Sons, 1980).
8. Donnell, L. H., "Stress Concentrations due to Elliptical Discontinuities in Plates under Edge Forces," Theodore von Karman Anniversary Volume, pp. 293-309, Pasadena, 1941.
9. Goodier, J. N., "Concentration of Stress Around Spherical and Cylindrical Inclusions and Flaws," Transactions of the ASME, vol. 55, pp. 39-44, 1933.
10. Hsu, T. T. C., and Slate, F. O., "Tensile Bond Strength Between Aggregate and Cement Paste or Mortar," Proceedings of the American Concrete Institute, vol. 60, no. 4, April 1963, pp. 465-485.
11. Kao, C. C., and Slate, F. O., "Tensile-Shear Bond Strength and Failure Between Aggregate and Mortar," Journal of Testing and Evaluation, JTEVA, vol. 4, no. 2, March 1976, pp. 148-150.

12. Taylor, M. A., and Broms, B. B., "Shear Bond Strength Between Coarse Aggregate and Cement Paste or Mortar," Proceedings of the American Concrete Institute, vol. 61, no. 8, August 1964, pp. 939-957.

ATE
LMED
8